

Politecnico di Torino

Politecnico di Torino

Master's Degree in Aerospace Engineering

A.Y. 2025/2026

Graduation Session July 2026

Automatic Calculation and Reporting of Spacecraft Structural Technical Margins

Academic Supervisor
Prof. Manuela BATTIPEDE

TAS Supervisor
Dr. Pietro NALI

Candidate
Leonardo GALEOTTI

Abstract

This thesis presents the development of a Femap custom post-processing tool for the assessment of composite laminate initial failure and sandwich structure Margins of Safety (MOSs) in aerospace applications, developed in collaboration with Thales Alenia Space.

The developed program aims at automating the evaluation of the main structural MOSs, significantly reducing analysis time and minimizing the risk of human error associated with manual post-processing activities. At the same time, the tool promotes the adoption of advanced failure theories for composite laminates in industrial finite element analyses. A graphical user interface was developed in order to provide a practical and user-friendly software for structural analysts.

For sandwich panels, the tool is capable of evaluating the main failure modes considering different finite element modelling approaches. In the case of panels with metallic skins, the software allows the assessment of MOS associated with skin yielding and ultimate failure, core shear failure, and local instability modes such as wrinkling, dimpling, and crimping.

For composite laminates, the work focuses on the implementation and comparison of two first ply failure criteria: the physically-based LaRC05 criterion and the phenomenological Hoffman criterion, which is commonly adopted in engineering practice. Particular attention was devoted to the implementation of the LaRC05 formulation, including the modelling of different failure mechanisms, nonlinear shear behaviour and in-situ strengths formulations accounting for the constraint effects of plies in multidirectional laminates.

The predictive capabilities of the implemented criteria were assessed through several validation case studies based on linear FEM analyses compared to experimental data available in the literature, including longitudinal and transverse loading conditions, shear-dominated laminates, off-axis compression, and open-hole configurations. The comparison highlighted the influence of physically-based criteria and in-situ strengths on the prediction of laminate failure, particularly for multidirectional laminates and complex stress states. The results also showed the potential benefits of advanced failure theories in providing more realistic and less conservative structural assessments for composite structures. Finally, after the validation of the implemented methodologies, the developed tool was applied to the analysis of different sandwich panels belonging to a real satellite, considering both metallic and composite skins together with different finite element modelling approaches.

Contents

List of Figures VI

List of Tables IX

1 Introduction 1
- 1.1 Background . . . 1
- 1.2 Scope of the work . . . 2
- 1.3 Outline . . . 3

2 Design and analysis of sandwich structures 4
- 2.1 Introduction . . . 4
- 2.2 Structural concept . . . 5
- 2.3 Design considerations . . . 7
- 2.4 Margins of Safety for sandwich panels . . . 9
- 2.5 Honeycomb sandwich modelling in FEM programs . . . 13

3 Failure criteria for Composite Laminates 15
- 3.1 Introduction . . . 15
  - 3.1.1 Failure mechanisms and laminate failure definition . . . 15
  - 3.1.2 General form and classification of failure criteria . . . 18
  - 3.1.3 Strength parameters for ply-level failure criteria . . . 19
  - 3.1.4 Adopted failure criteria . . . 20
- 3.2 Hoffman criterion . . . 21
- 3.3 LaRC05 criterion . . . 22
  - 3.3.1 Development and philosophy of the LaRC criteria . . . 22
  - 3.3.2 Main features of LaRC03 and LaRC04 . . . 23
  - 3.3.3 LaRC05 formulation adopted in the present work . . . 24
  - 3.3.4 Fibre tensile failure . . . 24
  - 3.3.5 Matrix failure . . . 25
  - 3.3.6 Fibre kinking failure . . . 28
  - 3.3.7 In-situ strengths . . . 32
- 3.4 Remarks on the considered criteria . . . 36
- 3.5 Margin of Safety for composite laminates . . . 36

3.5.1 Hoffman Criterion . . . 37
3.5.2 LaRC05 Criteria . . . 38
3.5.3 Remarks . . . 40

4 Failure criteria implementation in Femap API 41
4.1 Introduction to Femap and Femap API . . . 41
4.2 API overview . . . 43
4.3 API update . . . 44
4.4 API improvements . . . 46
4.5 Implementation aspects of the LaRC05 formulation . . . 48
4.5.1 Numerical solution of nonlinear equations . . . 48
4.5.2 Implementation of in-situ strengths formulations and shear nonlinearity . . . 49
4.6 User guide . . . 55
4.6.1 Safety factor . . . 57
4.6.2 *Composite Laminates FI/MOS* Mode . . . 57
4.6.3 *Sandwich Panel MOS* Mode . . . 60
4.7 Fracture toughnesses . . . 62
4.7.1 Comparison of interlaminar and intralaminar fracture toughness . 66

5 Validation case studies 68
5.1 Material Properties and In-Situ Strengths . . . 68
5.2 Overview of Validation Test Cases . . . 70
5.3 Summary of Validation Results . . . 72
5.3.1 Longitudinal Tension and In-Plane Shear Tests . . . 74
5.3.2 Longitudinal Compression Tests . . . 78
5.3.3 Transverse Loading Tests . . . 80
5.3.4 Off-Axis Compression Tests . . . 80
5.3.5 Open-Hole Strength Tests . . . 82
5.3.6 Short Beam Strength Tests . . . 84

6 Application to a real satellite use case 87
6.1 Overview of the Case Study . . . 87
6.2 -X Panel Results . . . 91
6.3 -Y Panel Results . . . 93
6.4 -Z Panel Results . . . 95
6.5 Comparison of MOS predictions obtained with Hoffman and LaRC05 . . . 97

7 Conclusions 99

Bibliography 101

A Femap API Upgrade: Implementation Aspects 108
A.1 Implementation Examples 108
A.2 Standardization of the Output Vector IDs 111

List of Figures

2.1 Sandwich composites applied in satellites. Example: Sentinel-1D Earth observation satellite (image source: Thales Alenia Space [66]). 5
2.2 Comparison between a sandwich panel and an I-beam (from [25]) 6
2.3 Load-carrying mechanism of a sandwich panel (from [25]) 6
2.4 Skins instabilities (adapted from [25]) 8
2.5 Characteristic directions of the honeycomb structure 10

3.1 Energy dissipating failure mechanisms of continuous fibre composite materials (from [6]) 17
3.2 Hoffman failure surface for IM7/8552 22
3.3 Definition of the fracture plane orientation and associated local stress components (from [47]) 25
3.4 Experimental evidence of fibre kinking and schematic representation of the kink-band geometry 28
3.5 Physical model for kink-band formation and coordinate systems associated with fibre kinking (from [48], with permission from SAGE Publications, License Number 6278710457725) 30
3.6 Idealized models adopted for the derivation of in-situ strengths for thick embedded, thin embedded and thin outer plies. (from [8] , with permission from Elsevier, License Number 6278711312248) 34
3.7 Idealized Mode I and Mode II intralaminar crack loading conditions associated with σ_{22}, τ_{12} and τ_{23} in LaRC04/05 35

4.1 API as interface between code and Femap database 42
4.2 Obsolete API warning 45
4.3 Example of nonlinear longitudinal shear and transverse compression stress–strain responses of IM7/8551-7 ((from [48], with permission from SAGE Publications, License Number 6278710457725)) 49
4.4 In-situ transverse tensile strength predictions as a function of ply thickness based on linear formulations (from [47]) 50
4.5 In situ longitudinal shear strength: linear and non-linear predictions . . . 52
4.6 Starting interface of the API 56
4.7 *Composite Laminates FI/MOS* interface 58

4.8 *LaRC05 Laminate Modelling Assumptions* interface 59
4.9 *LaRC05 Material Input* interface 60
4.10 *Sandwich Panel MOS* Interface 61
4.11 *Metallic Materials Properties* Interface 62
4.12 *Sandwich Panel Properties* Interface 62
4.13 *Honeycomb Materials Properties* Interface 63
4.14 Slit crack geometry (from [47]) 63
4.15 Overview of ply-level failure modes (from [35], with permission from Elsevier, License Number 6278730749245) 64
4.16 Transverse and longitudinal intralaminar crack growth (from [46], with permission from Elsevier, License Number 6278730972880) 64

5.1 Effect of β and η_L on in-situ strengths 69
5.2 FEM model adopted for the longitudinal tension tests, including boundary conditions and loading application 73
5.3 Stress and MOS distributions predicted for the LT-UD test 74
5.4 MOS distributions predicted for the LT-MD-02 test 75
5.5 Dominant LaRC05 failure modes predicted for plies with different fibre orientations in the LT-MD-02 test (red = fibre tensile failure; green = matrix failure; blue = fibre kinking failure) 76
5.6 MOS distributions predicted for the LC-MD-01 test 78
5.7 LaRC05 MOS distributions for the 0° plies in test LC-MD-01 79
5.8 Fracture angle α corresponding to the minimum MOS for matrix failure . 80
5.9 OAC-30 test specimen and results 81
5.10 FEM model adopted for open hole tests, including boundary conditions and loading application 82
5.11 OHT-MD-02 test results 83
5.12 FEM model adopted for the short beam strength tests, including boundary conditions and loading application 84
5.13 Stress and MOS distributions predicted for the SBS-UD test 85

6.1 Analysed satellite panels 88
6.2 -X Panel - honeycomb MOS distribution - Load Case 8 91
6.3 -X panel - Hoffman minimum MOS distribution - Load Case 8 91
6.4 -X panel - LaRC05 minimum MOS distribution - Load Case 8 91
6.5 -X panel - LaRC05 failure mode distribution - Load Case 8 (red = fibre tensile failure; green = matrix failure; blue = fibre kinking failure) 92
6.6 -Y panel - dimpling MOS distribution - Load case 6 93
6.7 -Y Panel - yielding MOS distribution - Load Case 8 93
6.8 -Y Panel - honeycomb MOS distribution - Load Case 3 93
6.9 -Z panel - bottom skin - Hoffman minimum MOS distribution - Load Case 8 95
6.10 -Z panel - bottom skin - LaRC05 minimum MOS distribution - Load Case 8 95
6.11 -Z panel - LaRC05 failure mode distribution - Load Case 8 (red = fibre tensile failure; green = matrix failure; blue = fibre kinking failure) 96

6.12 -Z panel - honeycomb MOS distribution - Load Case 8 96

List of Tables

3.1 Formulae for in-situ strengths in LaRC05 (from [48]) 33

4.1 In-situ strength formulas implemented in the API 54

5.1 Material properties for IM7/8552 used in the present study. 68
5.2 In-situ strengths (MPa) of IM7/8552 under linear and nonlinear shear behaviour 69
5.3 Validation test matrix adopted for the assessment of the implemented failure criteria 71
5.4 Comparison between experimental results and numerical predictions obtained with Hoffman and LaRC05 criteria. 72

6.1 Group identification 88
6.2 Definition of the analysed load cases 89
6.3 -X Panel - Minimum MOS results 92
6.4 -Y Panel - Minimum MOS results 94
6.5 -Z Panel - Minimum MOS results 97
6.6 Relative variation of the minimum MOS predicted by the LaRC05 criterion with respect to the Hoffman criterion 98

A.1 Structure of the output vector ID 111
A.2 Prefix definition (NN) 111
A.3 Definition of result identifier (R) and ply index (PP) for each analysis mode (M) 113

Chapter 1

Introduction

1.1 Background

In the design of aerospace structures, the evaluation of safety margins across multiple failure modes is a fundamental and often time-consuming task. Structural analysts are required to assess the integrity of components under a wide range of loading conditions, considering both material behaviour and complex geometries. Automating this process can significantly reduce the workload and improve the efficiency and consistency of the analyses.

Composite laminates and sandwich panels are widely used in modern aerospace applications due to their high strength-to-weight ratio and design flexibility. However, most finite element codes do not directly provide margins of safety for sandwich failure modes. Therefore, the development of a reliable tool for their assessment is essential [57].

Moreover, in the satellite industrial context considered in this work, composite laminates are primarily employed as face sheets (skins) of sandwich structures. Experimental evidence shows that composite laminates often exhibit higher strength than that predicted by numerical models and classical failure theories implemented in Finite Element Method (FEM) analyses. This discrepancy may lead to overly conservative designs and unnecessary over-dimensioning of laminate structures.

Failure theories are typically employed in the preliminary design phase to size structural components, defining parameters such as thickness, stacking sequence and geometry. Beyond this stage, experimental testing on coupons or structural elements is performed to determine design allowables. These allowables are generally set at levels significantly lower than the ultimate load-carrying capability in order to account for uncertainties related to fatigue, environmental conditions, impact damage, and other unmodelled effects.

As a result, the aerospace industry has historically relied on a "make and test" approach, supported by extensive experimental databases developed at considerable cost.

This methodology, combined with conservative safety factors, has reduced the immediate need for highly accurate failure theories in practical design applications [28]. Consequently, advanced failure models have often been regarded more as an academic exercise than as a practical engineering tool.

However, this perspective is gradually changing. The increasing demand to reduce development time and production costs, together with the need to fully exploit the performance of fibre-reinforced polymers (FRPs) in complex applications, is driving a shift towards more predictive and analysis-based design approaches. The traditional "make and test" philosophy is becoming unsustainable, and improved analytical criteria are now required to support faster and more efficient design processes [28].

While simplified failure theories may be sufficient for preliminary sizing, more advanced models capable of capturing the underlying physical mechanisms of damage and failure are highly desirable. These models provide designers with deeper insight into failure processes and enable more informed design choices, potentially leading to improved structural performance [56].

In addition to strength requirements, designers must also consider constraints such as weight minimization, material cost, and manufacturability. Therefore, the development of reliable and efficient analytical tools that integrate advanced failure theories represents a key step towards more optimized and cost-effective composite structures [56].

Furthermore, the choice of an analysis method is influenced not only by its predictive accuracy, but also by its simplicity, computational efficiency, and ease of implementation within the design process. In this context, advanced failure theories can only be effectively adopted if embedded in reliable and user-friendly computational tools. Ultimately, even the most advanced theory is of little practical value if it is not made available in an accurate and accessible form [56].

1.2 Scope of the work

The aim of this work is to upgrade and enhance a Femap API for the evaluation of structural Margins of Safety (MOS) for sandwich panels, with particular focus on the composite laminate skins.

This thesis has been carried out in collaboration with Thales Alenia Space (TAS), within which the developed tool originates. The initial concept and requirements for the API were defined by the company, based on practical needs arising from their engineering activities.

The developed tool implements both classical and advanced failure criteria for composite laminates, namely the Hoffman criterion and the LaRC05 criterion. By combining a traditional phenomenological approach with a more physically-based failure model, the objective is to evaluate whether the adoption of advanced criteria can lead to higher and more realistic safety margins already at the FEM design stage.

The developed API is intended to serve as a practical engineering tool, capable of automating repetitive tasks and supporting structural analysts in their daily workflow, while also promoting the adoption of more advanced and reliable analysis methodologies.

1.3 Outline

This thesis is structured as follows.

Chapter 2 presents the behaviour, failure modes, and margins of safety of sandwich panels, providing the basis for their implementation in the developed tool.

Chapter 3 introduces the theoretical background required to understand failure criteria for composite laminates. The two failure theories considered in this work are presented and discussed.

Chapter 4 presents the development, update, and enhancement of the Femap API. After introducing the Femap environment and the API architecture, the implemented functionalities are described, together with the procedure adopted for the computation of margins of safety for composite laminates, including in-situ strengths.

Chapter 5 provides application examples to validate and demonstrate the capabilities of the developed tool. Different test cases are considered to highlight the influence of the selected failure criteria on the predicted margins of safety.

Finally, in Chapter 6, the API is applied to the analysis of sandwich panels belonging to an actual satellite, considering different modelling approaches and both metallic and composite skins.

Chapter 2

Design and analysis of sandwich structures

2.1 Introduction

One of the main challenges for design engineers in the space industry is weight reduction, as each kilogram significantly impacts mission costs. In this context, sandwich composites have become one of the most efficient structural solutions, offering high bending stiffness and excellent strength-to-weight ratios [41, 25]. Although each constituent material is relatively weak and flexible when considered individually, their combined action results in an extremely stiff, strong, and lightweight structure [5].

A typical sandwich structure consists of two thin, stiff, and high-strength facing skins separated by a thick and lightweight core. The skins are bonded to the core using structural adhesives capable of efficiently transferring loads between the faces [41, 1] (see Figure 2.2).

In satellites, facing skins are typically made of fibre-reinforced polymer (FRP) laminates or aluminium alloys. For composite laminates, epoxy resins are preferred to unsaturated polyester resins and vinyl esters due to their low weight, high strength, dimensional stability, and superior resistance to heat distortion and shrinkage. Carbon fibres are the most widely used reinforcement due to their low density, high stiffness, and excellent tensile properties. Aramid fibres are even used where impact resistance and toughness are critical, despite their limitations in compressive strength and adhesion [41].

The core is typically based on honeycomb architectures, most commonly with hexagonal or square cell configurations. They consist of a network of cells resembling a beehive and are typically 90–99% void space in their expanded form. Honeycomb offers the best strength-to-weight ratio of the core materials. Aluminium is the most commonly used material for honeycomb cores [41]. Structural adhesives, such as epoxy, acrylic, and urethane resins, are used to bond the skins to the core and ensure effective load transfer [41].

Sandwich panels are extensively used in satellite structures, as shown in Figure 2.1.



Figure 2.1: Sandwich composites applied in satellites. Example: Sentinel-1D Earth observation satellite (image source: Thales Alenia Space [66]).

The main applications highlighted in the figure include: (1) solar panels, (2) antenna structures and reflectors, and (3) satellite structures. Solar panels typically consist of carbon/epoxy prepreg skins combined with aluminium honeycomb cores and film adhesives. Antenna structures often employ aramid-epoxy or carbon-cyanate prepregs in combination with aramid or aluminium honeycomb cores [41].

In primary structures, which carry the main flight loads and define the global stiffness, carbon fibre reinforced polymer (CFRP) skins with aluminium honeycomb cores are typically used. Secondary structures, which have a negligible contribution to the overall stiffness, are more commonly manufactured with aluminium skins and cores. This choice is driven not only by cost considerations but also by the high thermal conductivity of aluminium, which makes these components well suited for thermal control functions.

In addition, sandwich panels are also employed in tertiary structures, where mechanical requirements are less demanding.

2.2 Structural concept

The structural behaviour of a sandwich panel can be effectively understood by analogy with an I-beam (see Figure 2.2). The facing skins act similarly to the flanges of the beam, as they carry nearly all the in-plane and bending (primary) stresses to which the panel is subjected, and provide most of the bending rigidity of the structure.

Similarly, the honeycomb core corresponds to the web of the I-beam. The core resists transverse shear and compressive loads, increases the stiffness of the structure by keeping the facing skins separated, and, compared to an I-beam, provides continuous

support to the flanges (or facing skins), resulting in a uniformly stiffened panel. It also provides most of the shear rigidity of the sandwich structure. The core-to-skin adhesive rigidly joins the sandwich components and allows them to act as a single unit with high torsional and bending rigidity [25, 41, 1]. Figure 2.3 shows the load-carrying mechanism of a sandwich panel, for example in a cantilever configuration.

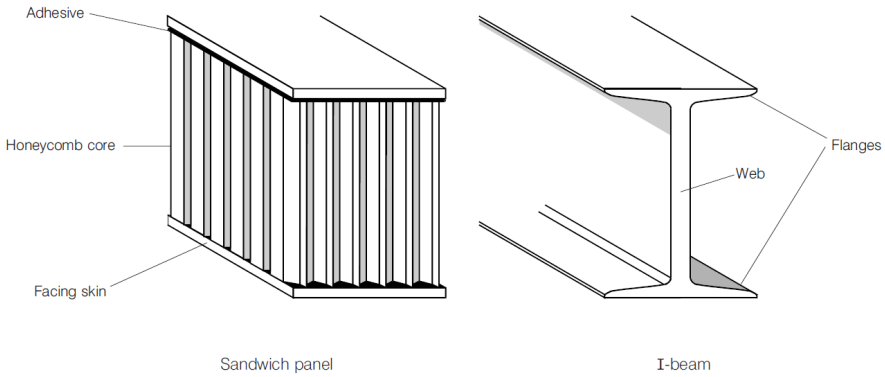


Figure 2.2: Comparison between a sandwich panel and an I-beam (from [25])

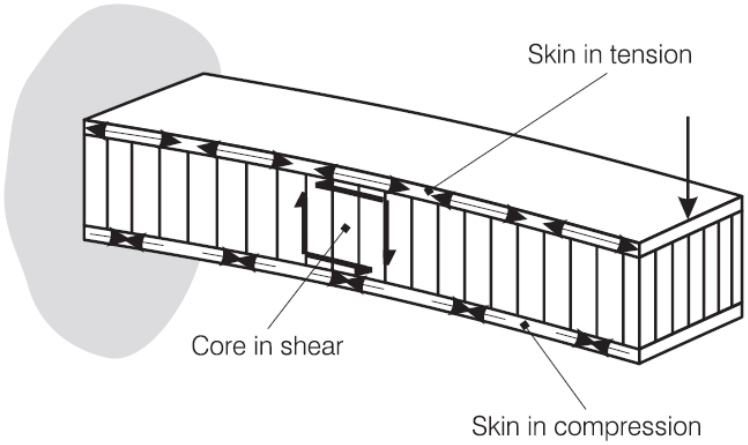


Figure 2.3: Load-carrying mechanism of a sandwich panel (from [25])

It is an efficient structural shape because as much material as possible is placed in the skins, which are located farthest from the neutral axis. Only enough material is left in the core to ensure interaction between the skins and to resist shear and buckling. The main difference with respect to an I-beam is that the core of a sandwich structure is made of a different material than the face sheets and is distributed as a continuous support. This stabilizes the face sheets against local buckling phenomena such as wrinkling [1].

2.3 Design considerations

The design of sandwich structures generally follows the same principles as composite laminate design; however, several failure modes and design aspects specific to sandwich construction must be considered. In particular, for sandwich panels with a honeycomb core, the most critical aspects are shear deformations, dimpling, and wrinkling [5, 1].

Shear deformations arise from the relatively low shear modulus of the honeycomb core (for aluminium honeycomb typically not exceeding 0.5 GPa [25]), especially when compared to solid aluminium alloys (approximately 25 GPa) [5].

Dimpling and wrinkling are local buckling instabilities affecting the face sheets. These phenomena are critical in sandwich structures, as they can lead to premature failure even when global stresses are within allowable limits.

The design process typically begins with the definition of loading and boundary conditions. This is followed by the identification of design requirements, including deflection limits, thickness constraints, weight targets, and safety factors. Based on these requirements, a preliminary material selection can be performed, also guided by prior company experience and market availability of materials.

For simple loading conditions (e.g. uniform load distribution or a single concentrated force) and simple boundary conditions (e.g. simply supported edges, cantilever), preliminary estimations of stiffness, deflection, and stresses in the skins and core can be carried out using beam or plate theory, depending on the panel width-to-length ratio.

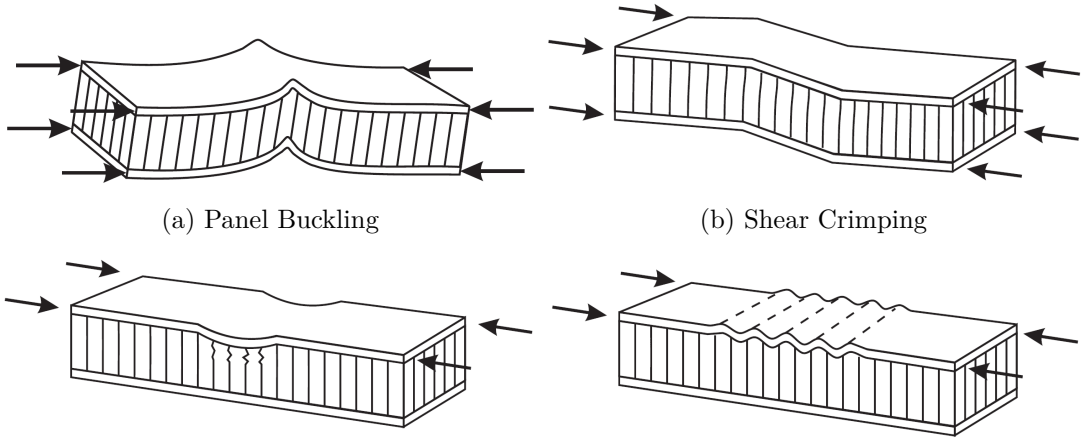
For more complex geometries or loading conditions, the use of computer-aided engineering tools may be required even at the preliminary design stage [41]. In all cases, subsequent design iterations typically involve more detailed analyses of the structural behaviour, often performed using finite element analysis (FEA).

Designers must ensure that all relevant failure modes, discussed below, are properly evaluated [41]:

- **Stiffness requirement:** Designers must ensure that the maximum allowable deflections, including shear deformation, are not exceeded under the most severe service loading conditions. In satellite applications, sandwich panels are often integrated into highly constrained structural assemblies and connected through inserts or bolted interfaces. These constraints tend to limit global displacements and promote load transfer primarily through bending. As a result, shear deformation may have a secondary influence on the global response, although it should not be neglected in the design phase.

- **Skin and core strength:** The face sheets and core materials must withstand the tensile, compressive, and shear stresses induced by the applied loads. The skin-to-core adhesive must be capable of effectively transferring shear stresses between the skins and the core [25, 41]. In the case of composite face sheets, appropriate failure criteria must be used to verify the operating conditions (see Chapter 3).

- **Global panel buckling:** (Figure 2.4a) This mode corresponds to the overall instability of the panel under compressive loads. The core thickness and shear



(a) Panel Buckling (b) Shear Crimping

(c) Skin Wrinkling (d) Skin Dimpling (Intra cell Buckling)

Figure 2.4: Skins instabilities (adapted from [25])

stiffness must be sufficient to prevent buckling. In practice, this is typically assessed through eigenvalue buckling analyses (e.g. Nastran SOL 105), ensuring that the applied load remains below the critical buckling load.

- **Shear crimping (core shear buckling):** (Figure 2.4b) This instability occurs when the wavelength of the buckling mode is comparable to the honeycomb cell size. It is characterized by local core shear failure combined with lateral displacement of the face sheets. Although it appears as a local phenomenon, it is associated with a form of global instability and is more likely to occur in cores with low shear modulus. Sometimes occurs after, and as a consequence of, global buckling.

- **Face sheet wrinkling:** (Figure 2.4c) This is a local instability involving short-wavelength buckling of the compressed face sheet, often accompanied by core crushing, tearing, or face sheet-to-core debonding. It is more critical in configurations with thin face sheets and low-density cores. The wrinkling wavelength is typically very small, making this mode relatively insensitive to boundary conditions [36]. The critical wrinkling stress can be increased by using cores with higher compressive stiffness [5]. One or both face sheets may wrinkle, depending on the loading, materials, and thickness of core and face sheets.

- **Face sheet dimpling (intracell buckling):** (Figure 2.4d) This local instability, specific to sandwich panels with cellular cores such as honeycomb, occurs when the face sheet buckles within a single cell. It is more likely in panels with thin face sheets and large cell sizes. This failure mode can be mitigated by reducing the cell size or increasing the face sheet stiffness [5, 36].

2.4 Margins of Safety for sandwich panels

In structural design, the *Margin of Safety* (MOS) is commonly used to compare the stresses acting on a structure with the corresponding allowable values. Including a global safety factor (SF), the MOS is defined as:

$$MOS = \frac{\text{Allowable Stress}}{SF \cdot \text{Calculated Stress}} - 1$$

In satellite structural applications, the safety factors shall be selected according to the ESA standard ECSS-E-ST-32-10C [17], depending on the specific verification case considered (further details are provided in Section 4.6).

Considering the failure modes discussed in the previous section, the evaluation of margins of safety for strength requirements differs depending on whether the sandwich skins are isotropic or made of composite laminates. For isotropic skins, allowable stresses can be directly compared with the calculated stress state. In contrast, composite laminates require the adoption of appropriate laminate failure criteria, which are discussed in detail in Chapter 3.

Although sandwich panels with composite laminate skins are widely used in aerospace structures, both this section and the API implementation described in Chapter 4 evaluate the MOS associated with face-sheet instabilities assuming isotropic skins. This assumption is motivated by the following considerations:

- The formulas available in the literature for evaluating critical instability stresses are often based on the assumption of isotropic face sheets [36, 25]. Although formulations for orthotropic laminates are available [24, 36], their application is generally more complex and less consolidated. In particular, in ECSS-E-HB-32-20 Part 3A [57] is highlighted that classical dimpling models may not accurately predict intra-cell buckling in sandwich structures with thin and strongly orthotropic facings.

- Composite face sheets are generally thicker and stiffer than aluminium skins (typically 0.4–0.6 mm for aluminium and above 1 mm for CFRP laminates). Since the critical stresses associated with instability phenomena increase with skin stiffness and thickness, wrinkling and dimpling are generally less critical for composite skins in preliminary design assessments.

- Composite laminates do not exhibit a single allowable stress value that can be directly compared with the computed stress state. A possible engineering approximation could consist in representing the laminate through an equivalent orthotropic shell derived from Classical Lamination Theory (CLT), allowing the evaluation of equivalent stress quantities and principal stresses for preliminary instability assessments.

In finite element models, the sandwich metallic skins are typically represented using two-dimensional shell elements. In order to evaluate the margins of safety associated

with the face sheets, it is first necessary to distinguish between elements subjected to compression and those subjected to tension. Since shell elements are generally analysed under a plane stress assumption, this identification can be performed by evaluating the minimum principal stress $\sigma_{\min}$ in each element. If the minimum principal stress is negative, the element is considered to be under compression in at least one direction. The MOS associated with crimping, wrinkling and dimpling are calculated only for skins elements subjected to compressive stresses.

The formulas adopted for the MOS calculations are presented below under the assumption of isotropic skins.

Skin yielding and ultimate strength MOS In this case, the allowable stress corresponds to the yield or ultimate strength of the material, while the calculated stress is represented by the Von Mises equivalent stress σ_{eq}. For elements subjected to compressive stress states:

$$\text{if } \sigma_{\min} < 0 \quad \Rightarrow \quad MOS_c = \frac{\sigma_c^{ult}}{SF \cdot \sigma_{eq}} - 1 \quad \text{and} \quad MOS_y = \frac{\sigma_y}{SF \cdot \sigma_{eq}} - 1$$

For elements subjected to tensile stress states:

$$\text{if } \sigma_{\min} \geq 0 \quad \Rightarrow \quad MOS_t = \frac{\sigma_t^{ult}}{SF \cdot \sigma_{eq}} - 1 \quad \text{and} \quad MOS_y = \frac{\sigma_y}{SF \cdot \sigma_{eq}} - 1$$

where σ_c^{ult}, σ_t^{ult}, and σ_y are the ultimate compressive strength, ultimate tensile strength, and yield strength of the skin under consideration, respectively.

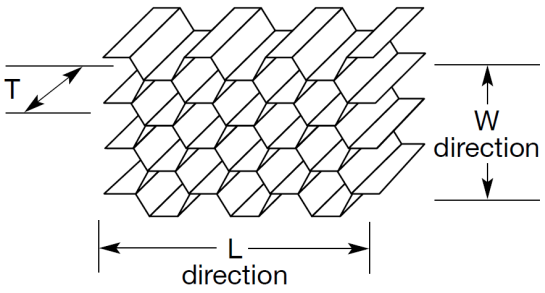


Figure 2.5: Characteristic directions of the honeycomb structure

Core strength MOS Generally, the mechanical properties of honeycomb cores, with reference to the directions shown in Figure 2.5, are expressed in terms of compressive strength and elastic modulus in the through-the-thickness (T) direction, together with shear strengths and shear moduli in the LT and WT planes, namely G_{LT}, τ_{LT}^{ult}, G_{WT}, and τ_{WT}^{ult}. The LT and WT planes are commonly referred to as the L and W directions,

respectively. The core strength MOS associated with shear loading in the LT and WT planes are evaluated as:

$$MOS_{LT} = \frac{\tau_{LT}^{ult}}{SF \cdot |\tau_{XZ}|} - 1 \quad \text{and} \quad MOS_{WT} = \frac{\tau_{WT}^{ult}}{SF \cdot |\tau_{YZ}|} - 1$$

where τ_{XZ} and τ_{YZ} are the shear stresses evaluated in the material reference system associated with the honeycomb core.

The previous expressions evaluate the MOS independently for the LT and WT shear directions. However, since the honeycomb core may be subjected to combined shear stresses in both planes, an interaction criterion must be also considered in order to account for the simultaneous contribution of τ_{XZ} and τ_{YZ}. The combined shear failure index is evaluated according to the following quadratic interaction criterion:

$$FI_{LT-WT}^{comb} = \sqrt{\left(\frac{SF \cdot \tau_{XZ}}{\tau_{LT}^{ult}}\right)^2 + \left(\frac{SF \cdot \tau_{YZ}}{\tau_{WT}^{ult}}\right)^2}$$

and the corresponding MOS is computed as:

$$MOS_{LT-WT}^{comb} = \frac{1}{FI_{LT-WT}^{comb}} - 1$$

The above expressions assume that the material reference system is aligned with the characteristic directions of the honeycomb structure, with the x-axis corresponding to the L direction, the y-axis to the W direction, and the z-axis to the through-the-thickness (T) direction.

This convention shall also be respected when the honeycomb core is represented using equivalent orthotropic two-dimensional properties, where the reference 0° material direction must coincide with the L direction of the honeycomb.

Crimping MOS Shear crimping can be interpreted as a limiting case of global sandwich-panel buckling occurring in configurations with thin face sheets and low core shear stiffness [1]. For consistency with the wrinkling and dimpling assessment approach (see following paragraphs), the minimum principal stress is adopted as the reference compressive stress. As for the other skin instability modes, the crimping MOS is evaluated only for elements characterized by $\sigma_{\min} < 0$:

$$\sigma_{\text{crimp}} = \frac{h^2}{(t_1 + t_2)\, t_c} G_C \quad \Rightarrow \quad MOS_{\text{crimp}} = \frac{\sigma_{\text{crimp}}}{SF \cdot |\sigma_{\min}|} - 1$$

where t_1 and t_2 are the thicknesses of the two face sheets, t_c is the core thickness, and $h = t_c + \frac{t_1+t_2}{2}$ is the distance between the centroids of the face sheets. G_C is assumed as the minimum shear modulus of the honeycomb core between G_{xz} and G_{yz} [1], leading to a conservative estimate of the critical stress.

It may occur that, for sufficiently thick cores, σ_{crimp} exceeds the yield strength σ_y. In such cases, material yielding is expected to occur before the onset of crimping instability.

Wrinkling MOS Wrinkling occurs when the compressed face sheet buckles either into the core or outward, possibly leading to failure of the face-sheet-to-core adhesive bond. This instability mode can be modelled as the buckling of a compressed plate resting on an elastic foundation [57].

Several analytical formulations available in the literature, including the one adopted in the present work and implemented in the API, are based on the idealized case of a flat sandwich strut subjected to uniaxial compression. For this reason, the wrinkling assessment of sandwich structures subjected to combined loading conditions is commonly performed by comparing the critical wrinkling stress with the minimum principal face-sheet stress $\sigma_{\min}$. For sandwich structures with isotropic skins, both analytical and experimental evidence indicate that this approach provides reasonably accurate estimations [36].

The formulation adopted here was originally proposed by Norris et al. [40] for the prediction of wrinkling in honeycomb sandwich structures with initial manufacturing imperfections [36].

In practice, sandwich face sheets are never perfectly flat and may exhibit initial geometric imperfections introduced during the manufacturing and bonding processes. During the hot-bonding phase, the face sheets conform locally to the honeycomb core geometry, producing small-amplitude waviness with a characteristic wavelength typically related to the honeycomb cell size [40]. The formulation accounts for these imperfections through the parameter δ, representing the amplitude of the initial face-sheet waviness.

$$\sigma_{\text{wrink}} = \frac{0.82}{1 + 0.64\, K_\delta} E_f \sqrt{\frac{E_c\, t_f}{E_f\, t_c}} \quad \text{with} \quad K_\delta = \frac{\delta\, E_c}{t_c\, F_c} \quad \Rightarrow \quad MOS_{\text{wrink}} = \frac{\sigma_{\text{wrink}}}{SF \cdot |\sigma_{\min}|} - 1$$

where E_f and E_c are the Young's moduli of the considered face sheet and the core, respectively, while t_f and t_c are their corresponding thicknesses. The parameter δ represents the amplitude of the initial face-sheet waviness, and F_c is the lower flatwise sandwich strength.

By imposing $\delta = 0$, the ideal case of perfectly flat face sheets is recovered. In practical applications, F_c can reasonably and conservatively be assumed equal to the compressive strength of the honeycomb core.

Dimpling MOS The classical approach used for the prediction of dimpling instability is largely empirical. Several equations are available in the literature for estimating the critical dimpling stress. In particular, one of the most commonly used formulations is based on the assumption that each intra-cell plate, i.e. the portions of the face sheets supported along the honeycomb cell edges, can be approximated as an isotropic rectangular plate, simply supported along all edges and subjected to uniaxial compression [57].

The formula reported below is based on this assumption. The coefficient 2 is introduced as a calibration factor to account for the more restrictive boundary conditions imposed along the cell edges [57].

Generally, the plate side lengths are assumed equal to the diameter s of the circle inscribed within the honeycomb cell. However, during the hot-bonding process between the face sheets and the honeycomb core, local imperfections or air bubbles may produce regions where the bonding is not perfect. For this reason, a conservative approach is adopted by introducing a debonded length s_{dl}. In the present model, this assumption is equivalent to considering a plate with side lengths s_{dl} instead of s.

Consistently with the uniaxial compression assumption of the model, and similarly to the wrinkling assessment approach, the minimum principal face-sheet stress $\sigma_{\min}$ is adopted for the evaluation of the MOS in sandwich structures subjected to combined loading conditions [36].

The debonded length can be estimated through NDI techniques and is typically assumed to be approximately three times the honeycomb cell size. In the present formulation, the value $s_{dl} = 2.2\,s$ is adopted.

$$\sigma_{\text{dimp}} = 2\,\frac{E_f}{1-\nu_f^2}\left(\frac{t_f}{s_{dl}}\right)^2 \quad \text{with} \quad s_{dl} = 2.2\,s \quad \Rightarrow \quad MOS_{\text{dimp}} = \frac{\sigma_{\text{dimp}}}{SF \cdot |\sigma_{\min}|} - 1$$

where E_f, ν_f, and t_f are respectively the Young's modulus, Poisson's ratio, and thickness of the considered face sheet.

2.5 Honeycomb sandwich modelling in FEM programs

Several modelling approaches can be adopted for the finite element analysis of sandwich structures, depending on the required level of accuracy and the computational cost. The most common approaches can be summarized as follows:

- 2D shell elements based on classical plate theory, used to represent the skins only, while the sandwich behaviour is reproduced through equivalent membrane and bending stiffness properties. This approach can be adopted for both metallic and composite laminate skins. For example, FEMAP provides dedicated tools for the automatic generation of equivalent shell properties in the case of metallic sandwich panels, while equivalent isotropic properties for composite laminates can be obtained through the "Compute" function available in the laminate layup editor.
- 2D equivalent laminate elements representing both the face sheets and the core through homogenized properties.
- 3D Solid elements for the honeycomb core combined with 2D shell or laminate elements for the face sheets.
- Fully 3D models using solid elements for both the face sheets and the core.

When sandwich structures are analysed using equivalent two-dimensional shell formulations, numerical effects commonly referred to as *shear locking* may arise. Shear

locking is an artificial and non-physical stiffening effect that affects several shell finite elements formulations [57].

In many practical applications, where the panel span is large compared to its thickness, transverse shear deformations remain relatively small. In such cases, equivalent shell models may still provide reasonably accurate results with limited computational cost [25].

When a more detailed representation of the structural behaviour is required, the honeycomb core is often modelled using three-dimensional solid elements. Conversely, modelling the individual honeycomb cells is generally avoided in standard engineering analyses because of the excessively high computational cost [25].

With reference to the modelling of the honeycomb core, finite element analyses generally require the definition of the orthotropic material properties along the three characteristic directions T, L, and W (see Figure 2.5). However, experimentally available data are usually limited to the compressive modulus and strength in the T direction together with the shear strengths and moduli in the LT and WT planes. The remaining properties are rarely measured because of their extremely low values. In addition, reliable values for the honeycomb Poisson's ratios are generally unavailable.

For practical engineering analyses, the recommendations reported in [5, 25] can therefore be adopted:

- $E_x \simeq E_y \simeq 0$, $E_z = E_c$, where E_c is the compressive modulus in the T direction. The compressive strengths and moduli in the L and W directions can be conservatively assumed equal to approximately 1% of the corresponding T-direction properties.

- $G_{xy} \simeq 0$, $G_{xz} = G_{LT}$, and $G_{yz} = G_{WT}$. The in-plane shear properties in the LW plane can be assumed equal to approximately 1% of the average published LT and WT shear properties.

- ν_{xy}, ν_{xz}, and ν_{yz} can be assumed close to zero. In practice, a small non-zero value (typically 0.01) is often introduced to ensure numerical stability and allow the finite element solver to run correctly.

Chapter 3

Failure criteria for Composite Laminates

3.1 Introduction

Fibre-reinforced polymer (FRP) composites are widely used in high-performance engineering applications due to their high specific stiffness and strength, which enable significant weight reduction and improved structural efficiency.

However, the mechanical response and failure behaviour of composite laminates are considerably more complex than those of isotropic materials. The onset and progression of damage depend on several interacting factors, including constituent material properties, stacking sequence (layup), geometry, loading conditions and load history [43].

For this reason, the reliable structural design of composite components requires analytical and computational tools capable of predicting both the mechanical response and the initiation of failure. In this context, failure criteria are commonly employed to determine, at the ply level, whether the local stress or strain state exceeds the corresponding material strength limits.

A proper understanding of the underlying failure mechanisms is also essential, since different failure modes are governed by distinct physical processes that should be represented, at least approximately, within the adopted modelling framework [47].

Although numerous failure theories have been proposed, no single criterion is currently capable of accurately predicting failure for all laminate configurations, loading conditions and damage mechanisms. This limitation mainly arises from the complexity of the interacting microstructural damage processes and from the difficulty of relating them to the macroscopic structural response [47, 13].

3.1.1 Failure mechanisms and laminate failure definition

Failure in composite laminates can occur either within individual plies (*intralaminar* failure) or through the separation of adjacent plies (*interlaminar* failure). In order to formulate and apply reliable failure criteria for composite laminates, it is therefore

necessary to understand the physical mechanisms governing damage initiation and propagation.

The main failure modes of laminated fibre-reinforced composites are summarized below [47, 30, 43] (see Figure 3.1):

- **Delamination**: delamination consists in the separation of adjacent plies and may originate during manufacturing or be induced by mechanical loading. This mechanism significantly reduces the bending stiffness and compressive strength of the laminate, even in the absence of visible surface damage. It is particularly critical under compressive loading, where it can lead to a premature loss of load-carrying capacity.

- **Matrix compression failure**: this failure mode is primarily governed by shear mechanisms. Indeed, failure typically develops along inclined planes with respect to the loading direction, highlighting its shear-driven nature. Although matrix compression failure does not usually cause immediate structural collapse, it degrades stiffness and may promote the onset of other damage mechanisms, such as delamination.

- **Fibre compression failure**: this mode is strongly influenced by matrix properties and initial imperfections, such as fibre misalignment or voids. It is commonly associated with micro-buckling phenomena, in which initially misaligned fibres undergo localized instability under compressive loading. This instability leads to the formation of kink bands, i.e. localized regions in which fibres rotate collectively within the surrounding matrix. The development of kink bands results in a significant reduction in the compressive stiffness and strength of the laminate.

- **Matrix tensile failure**: this failure occurs when the matrix is subjected to tensile stresses transverse to the fibres. The resulting fracture surface is typically oriented normal to the loading direction and may be accompanied by limited fibre/matrix debonding or fibre splitting.

- **Fibre tensile failure**: this is a brittle and energy-releasing failure mode associated with the rupture of fibres under tensile loading along their direction. It generally leads to catastrophic failure of the laminate, especially in structures with limited load redistribution capability.

In the present work, only intralaminar failure modes are considered; interlaminar failure, i.e. delamination, is not taken into account.

Definition of failure in laminates From a structural point of view, laminate failure may be defined according to different criteria, depending on the level of conservatism required. In particular, a distinction is commonly made between initial failure and ultimate failure, which are conceptually analogous to yield and ultimate strength in metallic materials.

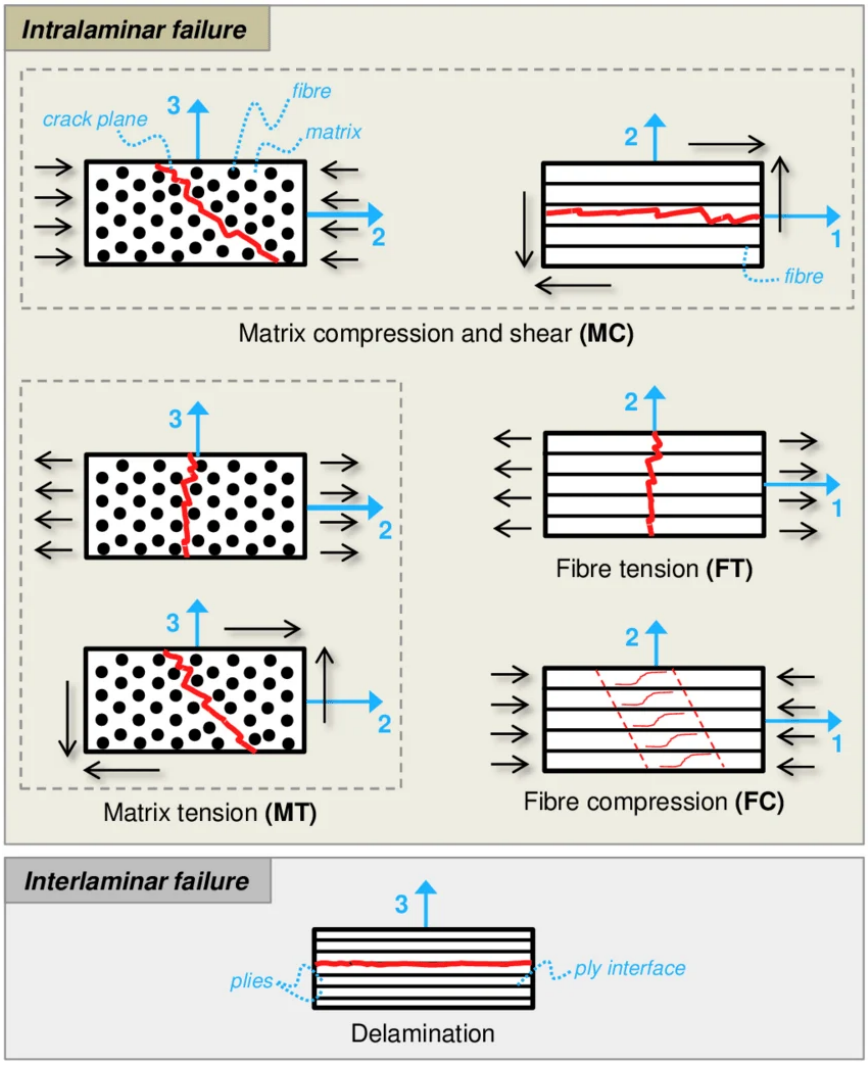


Figure 3.1: Energy dissipating failure mechanisms of continuous fibre composite materials (from [6])

In the first approach, known as *first-ply failure* (FPF), the laminate is considered to have failed when the first ply reaches its failure condition. This is determined by evaluating the stress or strain state in each ply under the applied loading and comparing it with the corresponding strength parameters through a suitable failure criterion [12].

Although the failure of a single ply does not necessarily lead to the collapse of the entire laminate, since the remaining plies may still carry load, the FPF approach is widely adopted in engineering practice as a conservative design criterion. This is mainly due to the significant complexity associated with accurately modelling damage evolution and the interaction between different failure mechanisms after damage initiation [30].

3.1.2 General form and classification of failure criteria

Regardless of their formulation, whether phenomenological or physics-based, most FPF criteria express failure through one or more scalar functions of the stress (or strain) components and strength parameters, generally referred to as *Failure Indices* (FI). Failure is assumed to occur when this function reaches a critical value of 1 as expressed by:

$$f(\sigma_1, \sigma_2, \sigma_3, \tau_{23}, \tau_{13}, \tau_{12}, F_1, F_2, \ldots) = \begin{cases} < 1 & \text{no failure} \\ = 1 & \text{failure limit} \\ > 1 & \text{failure} \end{cases}$$

where $\sigma_1, \ldots, \tau_{12}$ are the stress components in the ply reference system, with index 1 denoting the longitudinal (fibre) direction, index 2 the in-plane transverse direction and index 3 the through-the-thickness direction (see figure 3.1), and $F_1, F_2, \ldots$ represent the relevant strength parameters, which may correspond either to material strengths or to in-situ strengths, depending on the adopted failure criterion. The criterion is evaluated independently for each ply, and laminate failure is assumed to occur when the condition is satisfied in any one of the plies, according to the first-ply failure definition.

Classification The development of failure criteria for composite materials has been extensively investigated over the past decades, resulting in a wide range of theories available in the literature. These criteria can be classified according to different aspects, such as whether they are based on strength or fracture mechanics approaches, whether they provide a general prediction of failure or are specific to particular failure modes, and whether they address intralaminar or interlaminar failure [43].

Comprehensive comparisons and reviews of the most widely used failure criteria are provided by Nali et al. [39] and Orifici et al. [43]. In addition, detailed formulations of many criteria can be found in commercial finite element software documentation, such as the user guides of MSC Nastran [38], Femap [55], and ANSYS [2].

For the purposes of this work, two classifications are particularly useful in order to highlight the differences among the failure criteria considered. The first classification groups lamina failure theories into three main categories [39, 12]:

- **Limit or non-interactive theories**, in which specific failure modes are predicted by comparing individual lamina stress or strain components with the corresponding strength or ultimate strain values. No interaction between different stress components is considered. Typical examples are the maximum stress and maximum strain criteria.

- **Interactive theories**, such as the Tsai–Hill and Tsai–Wu criteria, in which all stress components are combined into a single scalar function that represents a failure surface in stress space. These approaches provide a global prediction of failure without distinguishing between different failure mechanisms.

- **Partially interactive or failure-mode-based theories**, such as the Hashin–Rotem and Puck criteria, where separate expressions are used to distinguish between fibre-dominated and matrix-dominated failure modes.

The second important classification distinguishes between *strength-based criteria* and *physically-based criteria*. The former are based on the macroscopic strength properties of the material used to form the plies (see the next subsection for more details). Such criteria are generally derived from phenomenological considerations and aim at providing mathematical formulations that best fit experimental data in a form that is practical for engineering design [13]. For this reason, they are still the most widely used in industrial applications.

In contrast, physically-based criteria have been developed more recently with the objective of achieving a more accurate representation of the underlying damage mechanisms [47, 48]. These approaches explicitly account, at least in an approximate manner, for the physical processes governing failure, such as fibre kinking or matrix cracking. Although they offer improved physical consistency, they are typically more complex and computationally demanding, and are therefore less commonly adopted in standard engineering practice.

3.1.3 Strength parameters for ply-level failure criteria

Laminated composites are orthotropic materials, characterized by different properties along different directions, as well as by distinct behaviours in tension and compression. Most failure criteria for composite laminates, including those considered in this thesis, are formulated at the ply level. Consequently, appropriate strength values at the lamina level must be defined in order to assess failure.

Two main approaches can be identified for the definition of these strength parameters.

A first approach, adopted for instance in the Hoffman criterion, consists in using the strengths measured on unidirectional (UD) laminates. At the macroscopic level, five main strength parameters are commonly used to characterize ply failure [30] (and are typically specified when defining a 2D orthotropic material, e.g., MAT8 in Nastran):

- tensile strength parallel to the fibres, denoted by X_T
- compressive strength parallel to the fibres, denoted by X_C
- tensile strength perpendicular to the fibres, denoted by Y_T
- compressive strength perpendicular to the fibres, denoted by Y_C
- in-plane shear strength, denoted by S

These strength values do not correspond to single, well-defined damage mechanisms. For instance, tensile failure in the fibre direction may involve a combination of fibre breakage, matrix cracking and fibre–matrix debonding.

Although these quantities are commonly treated as intrinsic material properties, this assumption is only approximate. In fact, the strength values reported for a material system are not obtained from isolated plies, but from standardized laminate configurations specifically designed to activate the desired stress state (e.g., $[0]_n$, $[90]_n$ or $[\pm 45]_n$ laminates). As a consequence, these parameters inherently depend on the test configuration and should be regarded as effective, rather than purely intrinsic, material properties.

From an engineering standpoint, this approximation remains widely accepted. Material properties are typically evaluated at the macroscale level through homogenization approaches, while a detailed representation of the microscale behaviour (including fibres, matrix and their interface) would require significantly more complex and computationally expensive models [39].

A second approach consists in the use of *in-situ strengths*. It has been experimentally observed that the strength of a ply embedded within a multidirectional laminate can differ significantly from that measured on unidirectional test coupons. In particular, transverse tensile and in-plane shear strengths are often higher due to the constraining effect of adjacent plies, which delays damage initiation and growth.

The use of in-situ strengths is therefore adopted in several advanced failure criteria, like LaRC05, in order to account for the influence of the laminate configuration on ply behaviour. In contrast, strength values obtained from standardized unidirectional tests may lead to conservative predictions when applied to general laminate configurations. Further details on in-situ strengths are provided in Sections 3.3 and 4.7.

3.1.4 Adopted failure criteria

Within the scope of this thesis, two failure criteria have been selected in order to represent both strength-based and physically-based approaches. In particular, the LaRC05 criterion is adopted as a physically-based model, since it is commonly regarded as one of the most advanced formulations available in the literature for predicting failure initiation in composite laminates. Although the original formulation also includes damage evolution capabilities, in the present work it is employed exclusively for failure initiation prediction.

For comparison, the Hoffman criterion is considered as a representative strength-based approach. Unlike the LaRC05 model, it provides a global prediction of failure based on macroscopic strength properties, without explicitly accounting for the underlying damage mechanisms. Moreover, the Hoffman criterion has been selected due to its long-standing and widespread use within the company, thus representing current industrial practice.

The adoption of these two criteria therefore enables a direct comparison between a physically-based formulation and a traditional strength-based engineering approach.

In the following subsections, only these two criteria are described in detail, as they are the ones implemented in the API presented in Chapter 4. For a more comprehensive overview of available failure criteria, the reader is referred to the aforementioned literature.

3.2 Hoffman criterion

In 1967, O. Hoffman proposed a phenomenological failure criterion for orthotropic brittle materials under a general three-dimensional stress state [29]. The formulation can be interpreted as an extension of the von Mises isotropic failure criterion to anisotropic materials through Hill's theory, further modified to account for different tensile and compressive strengths.

Unlike Hill's criterion, which assumes identical behaviour in tension and compression, the Hoffman formulation introduces linear stress terms, allowing the representation of strength asymmetry typical of composite materials [38].

The general three-dimensional formulation involves nine material parameters determined from basic strength data (tensile, compressive, and shear strengths). However, for composite laminates, the criterion is commonly expressed under plane stress conditions, since in finite element models laminates are often represented as two-dimensional structures.

The Hoffman criterion combines multiple stress components into a single failure index through a polynomial expression including both quadratic and linear stress terms. For this reason, it is often classified among interactive criteria [43, 39]. The failure index is written as [38, 2]:

$$FI = F_{11}\sigma_1^2 + F_{22}\sigma_2^2 + F_{12}\sigma_1\sigma_2 + F_{66}\tau_{12}^2 + F_1\sigma_1 + F_2\sigma_2 \tag{3.1}$$

This expression defines a failure surface in the stress space $(\sigma_1, \sigma_2, \tau_{12})$, representing the envelope of admissible stress states for the ply. If the stress state lies within this surface, no failure is predicted, whereas failure is assumed to occur when the failure index reaches a value equal to unity ($FI = 1$). The coefficients F_i are defined as:

$$F_{11} = \frac{1}{X_T X_C}, \quad F_{22} = \frac{1}{Y_T Y_C}, \quad F_{12} = -\frac{1}{X_T X_C}$$

$$F_{66} = \frac{1}{S^2}, \quad F_1 = \frac{1}{X_T} - \frac{1}{X_C}, \quad F_2 = \frac{1}{Y_T} - \frac{1}{Y_C}$$

As an example, Figure 3.2 shows the Hoffman failure surface for IM7/8552 (the corresponding strength values are reported in Table 5.1). It can be observed that, unlike Hill's criterion, the surface is not a symmetric ellipsoid centered at the origin. This is due to the presence of linear stress terms, which introduce asymmetry between tensile and compressive behaviour.

It should be noted that the failure index may assume negative values due to the presence of linear stress terms. These values do not indicate failure, but rather stress states far from the failure surface. The critical condition must therefore be evaluated based on the maximum value of the failure index, without considering its absolute value.

As Hoffman himself points out, this criterion does not distinguish between different failure modes (e.g. fibre or matrix failure) and lacks a strict phenomenological basis. It should be regarded as a smooth interpolation between experimentally determined strength values [29]. In this context, Puck and Schürmann [50] note that experimental

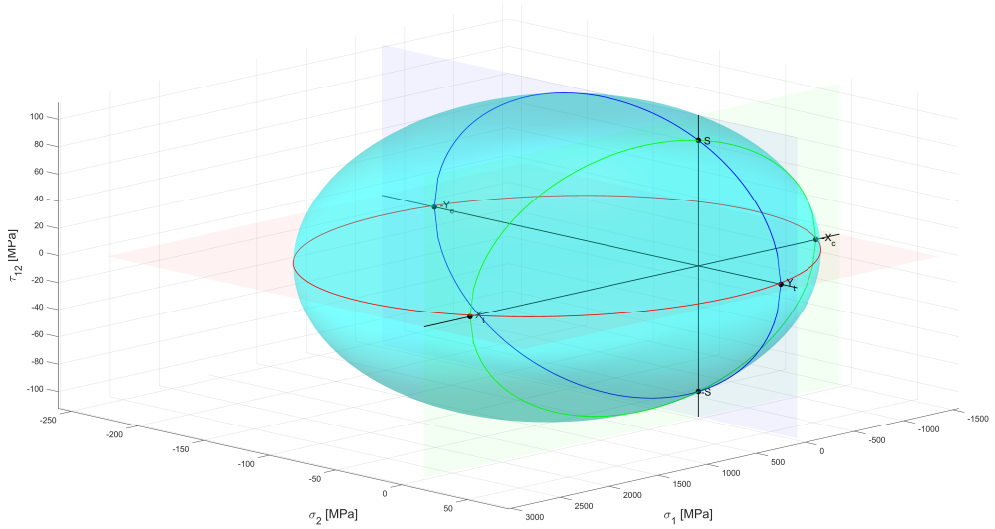


Figure 3.2: Hoffman failure surface for IM7/8552

evidence on composite laminates indicates a predominantly brittle behaviour at failure, particularly in inter-fibre (matrix-dominated) failure modes, and highlight the inconsistency of adopting criteria derived from ductile yield theories, such as those of von Mises and Hill.

Moreover, Hashin [23] pointed out inherent limitations of quadratic interactive criteria when considering biaxial stress states. For instance, consider the stress state $\sigma_1 = \sigma$, $\sigma_2 = \alpha\sigma$, and $\tau_{12} = 0$. Substituting this condition into the failure index expression yields a quadratic equation in σ. Due to the form of the coefficients F_i, the resulting equation depends on both tensile and compressive strength parameters, i.e. $\sigma = f(X_T, X_C, Y_T, Y_C, \alpha)$. As a consequence, failure under a purely tensile biaxial stress state may depend on compressive strengths, which is physically inconsistent.

Nevertheless, Hoffman failure criteria has demonstrated satisfactory predictive capability and is widely implemented in finite element codes. For this reason, it is still commonly adopted in engineering applications where a simple and efficient failure assessment is required, particularly in design scenarios where detailed failure mode differentiation or delamination effects are not critical [43].

3.3 LaRC05 criterion

3.3.1 Development and philosophy of the LaRC criteria

Between 1996 and 2004, the World-Wide Failure Exercise Part I (WWFE-I) was conducted as an international research project aimed at assessing the predictive capabilities of several failure criteria for composite laminates subjected to two-dimensional stress states [28]. The results highlighted significant limitations in the predictive accuracy of

the available models, particularly for multidirectional laminates [56, 13]. Among the evaluated approaches, the Puck criterion [50] demonstrated one of the best predictive capabilities and was recommended by the organizers of the WWFE for predicting final laminate failure [56]. Nevertheless, significant discrepancies with experimental results were still observed.

Following the WWFE, researchers at NASA Langley Research Center revisited existing failure theories with the aim of identifying the most accurate models and introducing physically-based improvements where possible. This effort led to the development of the LaRC03 criterion (acronym of Langley Research Center), formulated for in-plane stress states, and subsequently to the LaRC04 criterion, extended to three-dimensional stress conditions [47, 39]. Finally, within the framework of the World-Wide Failure Exercise Part II (WWFE-II) [32], a further improved formulation, referred to as LaRC05, was proposed in 2012 [48].

The philosophy behind LaRC criteria is that, despite the current incomplete physical understanding of failure in composite materials, adopting a physically-based modelling approach provides a robust foundation. This approach enables not only the prediction of the onset of failure, but also the identification of the governing failure modes and the assessment of the post-failure response in terms of residual material properties [48].

The LaRC formulations can therefore be regarded as evolutions and extensions of the Puck [50] and Hashin [23] criteria within a more physically-consistent framework [30, 21, 47, 48].

3.3.2 Main features of LaRC03 and LaRC04

The main features inherited from the Puck and Hashin theories can be summarized as follows:

- distinction between fibre-dominated and matrix-dominated failure modes, including separate formulations for tensile and compressive conditions;
- use of a matrix compressive failure criterion based on the Mohr–Coulomb criterion, motivated by the brittle behaviour of UD composite plies in the transverse direction, where the load is primarily carried by the polymer matrix and the compressive strength significantly exceeds the tensile strength;
- prediction of fibre tensile failure through a maximum stress criterion.

Significant advancements were nevertheless introduced in the LaRC03 and LaRC04 formulations, particularly for matrix tensile failure and fibre compressive failure.

Matrix cracking and the corresponding in-situ strengths are derived from the fracture mechanics analysis of a slit crack in a ply, originally proposed by Dvorak and Laws [16] for linear orthotropic materials and subsequently extended within the LaRC framework to account for nonlinear shear behaviour [47]. In particular, the energy release rates associated with intralaminar crack propagation are used to formulate mixed-mode matrix failure criteria under combined transverse and shear stresses, and to derive in-situ

strengths accounting for the constraining effect of adjacent plies within multidirectional laminates [13, 47, 30, 39].

In addition, concerning fibre compression failure, a dedicated mechanical model was introduced to represent fibre kinking as a distinct failure mode. This represents a significant improvement with respect to the Puck [50] and Hashin [23] criteria, where fibre compressive failure is predicted using a simple maximum stress criterion.

Overall, the LaRC04 formulation, valid for three-dimensional stress states, consists of six failure criteria associated with distinct physical mechanisms, including matrix cracking, fibre tensile failure, fibre kinking, and matrix-driven failure under combined loading conditions. Different formulations are adopted depending on the stress state and on the interaction between matrix failure and fibre kinking under compressive loading [47].

3.3.3 LaRC05 formulation adopted in the present work

The LaRC05 formulation consists of four failure indices defined at the ply level *for unidirectional composite plies*, distinguishing between matrix cracking, fibre kinking, fibre tensile failure, and polymer-dominated failure under hydrostatic pressure [48]. Compared to LaRC04, the number of failure indices was reduced, leading to a more efficient and practical implementation.

The failure index that accounts for failure under hydrostatic pressure has not been considered in the present work for two main reasons:

- the tool is intended for the structural design of satellite components operating in near-vacuum conditions, where no hydrostatic pressure is applied;
- the formulation is implemented through a Femap API applied to 2D laminate models, for which Nastran does not provide the out-of-plane stress component σ_3.

For this reason, only the remaining three failure indices are implemented and evaluated for each laminate ply. The maximum value is then assumed to be the governing failure index.

$$FI_{\text{ply}} = \max\left(FI_{FT}, FI_{M}, FI_{KINK}\right) \tag{3.2}$$

In contrast to LaRC03 and LaRC04, in the LaRC05 formulation the fracture mechanics analysis of intralaminar crack propagation is used only for the determination of in-situ strengths, rather than for the direct formulation of the failure indices. Further details are therefore provided in subsection 3.3.7, dedicated to the evaluation of in-situ strengths.

3.3.4 Fibre tensile failure

The maximum stress criterion has been shown to correlate well with experimental observations of fibre tensile failure. Accordingly, also within the LaRC05 framework, fibre

failure in a unidirectional ply subjected to a general 3D stress state is assumed to occur when the longitudinal stress in the fibre direction reaches the same critical value observed under uniaxial loading along the fibre direction [50].

Accordingly, the fibre tensile failure index is defined as:

$$FI_{FT} = \frac{\langle \sigma_1 \rangle_+}{X_T} \tag{3.3}$$

3.3.5 Matrix failure

Experimental evidence shows that matrix failure in composite laminates is governed by brittle fracture mechanisms. For this reason, the matrix failure criterion adopted in LaRC05 is based on a modified version of the Mohr-Coulomb criterion for unidirectional composite plies. This criterion, originally developed for brittle materials such as cast iron and widely used in soil mechanics, accounts for the different material response under tensile and compressive loading conditions [47].

Starting from the work of Puck [50], modified versions of the Mohr-Coulomb criterion have proven capable of accurately predicting matrix failure under multiaxial stress states [47]. An additional advantage of these formulations is that the fracture plane orientation is obtained directly from the failure analysis [48].

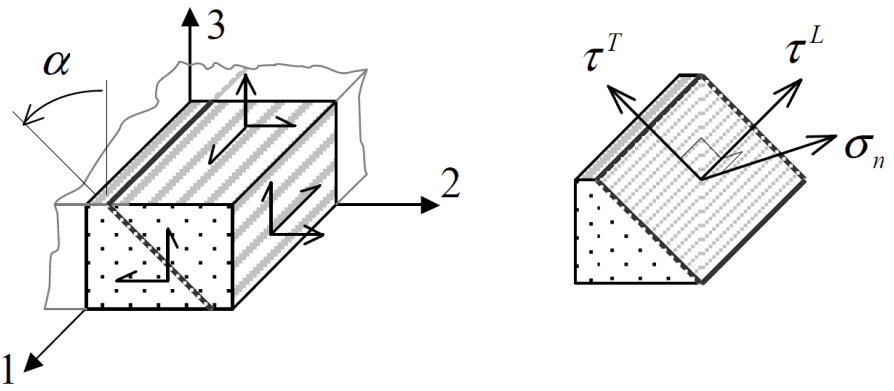


Figure 3.3: Definition of the fracture plane orientation and associated local stress components (from [47])

This criterion is based on the assumption that failure is exclusively governed by the stresses acting on a potential fracture plane forming an angle α with the through-the-thickness direction (see Figure 3.3) [50]. The stress components acting on the fracture plane are obtained through stress transformation:

$$\begin{cases} \sigma_N = \dfrac{\sigma_2 + \sigma_3}{2} + \dfrac{\sigma_2 - \sigma_3}{2}\cos(2\alpha) + \tau_{23}\sin(2\alpha) \\ \tau_T = -\dfrac{\sigma_2 - \sigma_3}{2}\sin(2\alpha) + \tau_{23}\cos(2\alpha) \\ \tau_L = \tau_{12}\cos\alpha + \tau_{31}\sin\alpha \end{cases} \tag{3.4}$$

The failure index expression proposed in LaRC05 is:

$$FI_M = \left(\frac{\tau_T}{S_T^{is} - \eta_T \sigma_N}\right)^2 + \left(\frac{\tau_L}{S_L^{is} - \eta_L \sigma_N}\right)^2 + \left(\frac{\langle \sigma_N \rangle_+}{Y_T^{is}}\right)^2 \tag{3.5}$$

For a given stress state, the fracture plane orientation considered in the analysis is the one corresponding to the value of α that maximizes FI_M within the interval $0° \leq \alpha \leq 180°$ [48, 10].

The parameters appearing in equation 3.5 are defined as follows:

- S_L^{is}, S_T^{is} and Y_T^{is} are respectively the in-situ longitudinal shear strength, in-situ transverse shear strength and in-situ transverse tensile strength. These strengths depend on the laminate configuration (UD or MD) and, in the case of multidirectional laminates, on the considered ply. Further details are provided in subsection 3.3.7.

- η_L and η_T are friction coefficients accounting for the influence of the normal traction on the corresponding shear strengths [48]. In particular, compressive normal tractions increase the effective shear strengths, whereas tensile normal tractions reduce them. These parameters are directly derived from the Mohr-Coulomb criterion and correspond to the slopes of the failure envelope in the $\sigma_N - \tau_L$ and $\sigma_N - \tau_T$ planes at $\sigma_N = 0$:

$$\eta_L = \left.\frac{\partial \tau_L}{\partial \sigma_N}\right|_{\sigma_N=0} \qquad \eta_T = \left.\frac{\partial \tau_T}{\partial \sigma_N}\right|_{\sigma_N=0}$$

The last term in equation 3.5 represents the contribution of positive normal tractions to crack opening. The notation $\langle \sigma_N \rangle_+$ denotes the McCauley brackets, defined as $\langle \sigma_N \rangle_+ = \max(0, \sigma_N)$. Therefore, the criterion is applicable to both tensile and compressive matrix failure conditions.

Evaluation of friction coefficients The friction coefficient η_T can be evaluated starting from the fracture angle under pure transverse compression, denoted as α_0. This angle is considered a material property [48] and can be experimentally determined through a transverse uniaxial compression test performed on a UD laminate.

The relation between η_T and α_0 can be obtained either analytically from equation 3.5 or geometrically from the Mohr–Coulomb criterion. In the present work, only the analytical derivation is reported. Under pure transverse compression, at failure, $\sigma_1 = \sigma_3 = \tau_{12} = \tau_{23} = \tau_{13} = 0$ and $\sigma_2 = -Y_C^{is}$. The stresses acting on the fracture plane become:

$$\begin{cases} \sigma_N = -Y_C^{is} \cos^2 \alpha \\ \tau_T = Y_C^{is} \sin \alpha \cos \alpha \\ \tau_L = 0 \end{cases}$$

Substituting these expressions into equation 3.5 gives:

$$FI_M = \frac{(Y_C^{is})^2 \sin^2\alpha \cos^2\alpha}{\left(S_T^{is} + \eta_T Y_C^{is} \cos^2\alpha\right)^2} \tag{3.6}$$

By definition, α_0 corresponds to the fracture plane orientation that maximizes FI_M under this loading condition. Moreover, failure occurs when $FI_M = 1$. Therefore, the following conditions must be satisfied:

$$\begin{cases} FI_M\big|_{\alpha=\alpha_0} = 1 \\ \left.\dfrac{\partial FI_M}{\partial \alpha}\right|_{\alpha=\alpha_0} = 0 \end{cases}$$

After some algebraic manipulations, not reported here for brevity, the condition of maximum failure index leads to the following relation:

$$\eta_T = -\frac{1}{\tan(2\alpha_0)} \tag{3.7}$$

This relation is also consistent with the geometrical interpretation of the classical Mohr–Coulomb criterion in the Mohr plane.

Regarding η_L, its determination is less straightforward, since it cannot be directly related to a single experimental measurement. Puck and Schürmann [50] proposed the following proportional relation:

$$\frac{\eta_L}{\eta_T} = \frac{S_L^{is}}{S_T^{is}} \tag{3.8}$$

For UD laminates, the in-situ strengths coincide with the experimentally measured ply strengths. Therefore, $S_L^{is} = S_L$ and $Y_C^{is} = Y_C$, where S_L is the in-plane shear strength according to the nomenclature introduced in subsection 3.1.3.

Conversely, S_T is not directly measured experimentally. However, its expression for UD laminates can be obtained from equation 3.6 by imposing the condition $FI_M\big|_{\alpha=\alpha_0} = 1$, leading to:

$$S_T = Y_C \cos(\alpha_0)\left(\sin(\alpha_0) + \frac{\cos(\alpha_0)}{\tan(2\alpha_0)}\right)$$

Substituting this relation together with equation 3.7 into equation 3.8, the following expression is obtained:

$$\eta_L = -\frac{S_L \cos(2\alpha_0)}{Y_C \cos^2(\alpha_0)} \tag{3.9}$$

This approach is commonly adopted in the literature [33]. Therefore, once the fracture angle α_0 and the ply strengths measured on UD laminates are known, equations 3.7 and 3.9 can be used to evaluate the friction coefficients η_T and η_L. For carbon/epoxy composites, typical values of the fracture angle are generally in the range $51° < \alpha_0 < 55°$ [48].

3.3.6 Fibre kinking failure

Introduction In advanced composite materials with high fibre volume fraction, compressive failure is often associated with the formation of a localized failure band, commonly referred to as a *kink band*. Within this band, fibres undergo a significant rotation while the surrounding matrix experiences large shear deformations [47].

Figure 3.4 presents, on the left, a microscopic view of a kink band and, on the right, its idealized representation. A kink band is generally characterized by three independent parameters: the fibre misalignment angle ϕ, the kink-band angle β, and the band width w. The misalignment angle ϕ represents the deviation of the fibres from their nominal longitudinal direction, while β represents the angle of inclination between the kink band boundary and the direction perpendicular to the fibres. The parameter w denotes the width of the localized deformation band.

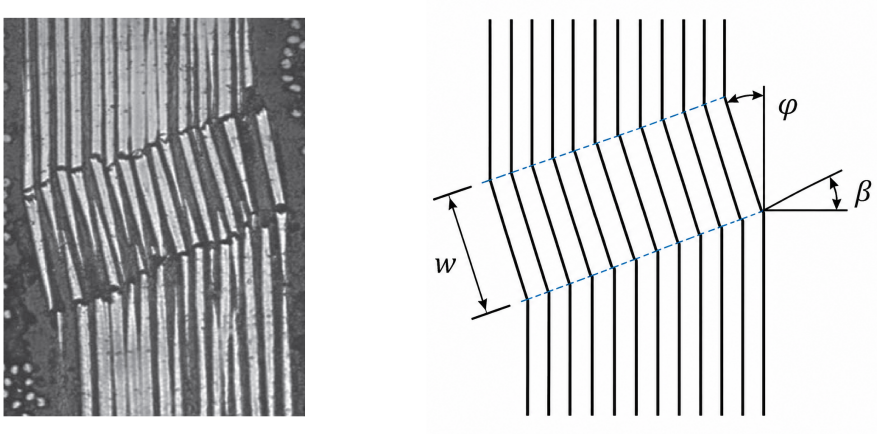


Figure 3.4: Experimental evidence of fibre kinking and schematic representation of the kink-band geometry

Among the various failure mechanisms in composite materials, fibre kinking is arguably one of the least understood. Experimental observations show that kink bands are typically visible after failure; however, experimental evidence capable of clarifying the triggering sequence leading to their formation is still limited. In particular, the mechanisms responsible for their formation in polymer-matrix fibre-reinforced composites are still a matter of debate within the scientific community [48]. Two main interpretations are commonly proposed:

- according to Rosen's hypothesis [52], kink-band formation is the final result of fibre microbuckling;
- according to Argon's hypothesis [3], kink bands are triggered by localized matrix failure in the vicinity of initially misaligned fibres.

According to the researchers involved in the development of LaRC05, experimental evidence suggests that matrix failure precedes kink-band formation and that fibre

microbuckling is not necessarily the primary triggering mechanism. Based on these observations, the LaRC05 criterion adopts an approach consistent with Argon's hypothesis, assuming that fibre kinking originates from shear-dominated matrix failure in a misaligned coordinate frame under significant longitudinal compression [48, 10].

More specifically, according to Argon's interpretation, fibre kinking originates from the presence of an initial fibre misalignment. Under longitudinal compressive loading, this misalignment induces shear stresses in the surrounding matrix. The resulting matrix shear deformation promotes an additional rotation of the fibres, which in turn further increases the shear stresses acting within the matrix. This closed-loop effect progressively amplifies fibre rotation and matrix deformation, eventually leading to matrix failure under shear loading (see Figure 3.5) [47].

Formulation A fully physically-based model capable of reproducing all the mechanisms involved in fibre kinking under a general 3D stress state would be extremely complex and impractical for engineering applications [47]. Consequently, based on the physical interpretation discussed above, the LaRC05 formulation evaluates the onset of fibre kinking by applying the matrix failure criterion (eq. 3.5) in a rotated coordinate system aligned with the kink-band orientation. In this approach, the local stresses acting in the misaligned coordinate system are used to determine the occurrence of shear-dominated matrix failure under longitudinal compression. The proposed expression is:

$$\text{if } \sigma_1 < 0 \quad \Rightarrow \quad FI_{KINK} = \left(\frac{\tau_{23}^m}{S_T^{is} - \eta_T \sigma_2^m} \right)^2 + \left(\frac{\tau_{12}^m}{S_L^{is} - \eta_L \sigma_2^m} \right)^2 + \left(\frac{\langle \sigma_2^m \rangle_+}{Y_T^{is}} \right)^2 \tag{3.10}$$

where σ_2^m, τ_{12}^m and τ_{23}^m are the stress components expressed in the misaligned coordinate system. To obtain these stresses, starting from the material coordinate system (1,2,3), two consecutive rotations are performed (see Figure 3.5).

The first rotation is carried out by an angle ψ, referred to as the kink-band angle, about the 1-axis, obtaining the stresses in the kink-band plane coordinate system. Indeed, the kink-band plane is not necessarily confined to the laminate transverse plane (2,3). The resulting stresses are:

$$\begin{cases} \sigma_2^\psi = \cos^2\psi\,\sigma_2 + \sin^2\psi\,\sigma_3 + 2\sin\psi\cos\psi\,\tau_{23} \\ \tau_{12}^\psi = \tau_{12}\cos\psi + \tau_{31}\sin\psi \\ \tau_{23}^\psi = -\sin\psi\cos\psi\,\sigma_2 + \sin\psi\cos\psi\,\sigma_3 + (\cos^2\psi - \sin^2\psi)\,\tau_{23} \\ \tau_{31}^\psi = \tau_{31}\cos\psi - \tau_{12}\sin\psi \end{cases} \tag{3.11}$$

The second rotation is performed about the 3^ψ axis by an angle equal to the fibre misalignment angle φ, thus obtaining the stresses in the misaligned coordinate system. The resulting stresses are:

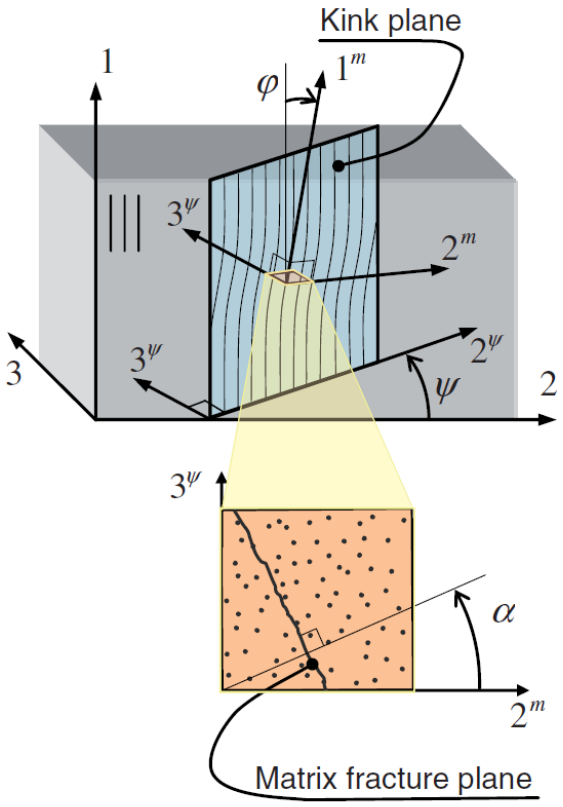


Figure 3.5: Physical model for kink-band formation and coordinate systems associated with fibre kinking (from [48], with permission from SAGE Publications, License Number 6278710457725)

$$\begin{cases} \sigma_2^m = \sin^2\varphi\,\sigma_1 + \cos^2\varphi\,\sigma_2^\psi - 2\sin\varphi\cos\varphi\,\tau_{12}^\psi \\ \tau_{12}^m = -\sin\varphi\cos\varphi\,\sigma_1 + \sin\varphi\cos\varphi\,\sigma_2^\psi + (\cos^2\varphi - \sin^2\varphi)\,\tau_{12}^\psi \\ \tau_{23}^m = \tau_{23}^\psi\cos\varphi - \tau_{31}^\psi\sin\varphi \end{cases} \tag{3.12}$$

The kink-band angle ψ is determined numerically in the range $0 < \psi < 180°$ so as to identify the critical kink-band orientation corresponding to the maximum failure index [48]. The procedure to determine ψ is discussed in the following section.

The same formulation is adopted in LaRC05 for both fibre kinking and fibre splitting. The distinction between the two mechanisms is based on the value of σ_1 compared to the longitudinal compressive strength X_C. However, this distinction mainly affects the subsequent propagation of damage within the material. Since damage propagation is beyond the scope of the present implementation, both mechanisms are here collectively referred to as fibre kinking.

Determination of the angle φ The misalignment angle φ is evaluated as the sum of an initial misalignment angle φ_0, representing manufacturing defects and fibre imperfections, and the shear strain γ_m induced by the applied loading and governed by the constitutive shear law $\tau = f(\gamma_m)$:

$$\varphi = \text{sign}\left(\tau_{12}^{\psi}\right)(\varphi_0 + \gamma_m) \tag{3.13}$$

The initial misalignment angle φ_0 is treated as a material property and can be estimated from the longitudinal compressive strength [48]. The procedure adopted in LaRC05 is based on a uniaxial compressive loading condition applied along the fibre direction. Under this assumption, the critical misalignment angle at failure φ_c can be obtained analytically from the fibre-kinking failure criterion. The corresponding shear strain at failure, denoted as γ_{m_c}, is then evaluated through the constitutive shear law. Finally, the initial fibre misalignment angle is obtained as:

$$\varphi_0 = \varphi_c - \gamma_{m_c} \tag{3.14}$$

Considering a uniaxial compressive loading condition at failure, with $\sigma_1 = -X_C$ and all the remaining stress components equal to zero, substitution into the stress transformation equations reported in Eq. 3.12 leads to the following stress components, independently of the value of ψ:

$$\begin{cases} \sigma_2^m = -\sin^2\varphi_c\, X_C \\ \tau_{12}^m = \sin\varphi_c \cos\varphi_c\, X_C \\ \tau_{23}^m = 0 \end{cases}$$

By imposing $FI_{KINK} = 1$ in Eq. 3.10, the following relation is obtained:

$$S_L^{is} = X_C\left(\sin\varphi_c\cos\varphi_c - \eta_L \sin^2\varphi_c\right) \tag{3.15}$$

Solving the previous equation for φ_c yields:

$$\varphi_c = \arctan\left(\frac{1 - \sqrt{1 - 4\left(\dfrac{S_L^{is}}{X_C} + \eta_L\right)\dfrac{S_L^{is}}{X_C}}}{2\left(\dfrac{S_L^{is}}{X_C} + \eta_L\right)}\right) \tag{3.16}$$

The shear strain at failure is then obtained from the constitutive shear law as:

$$\gamma_{m_c} = f^{-1}\left(\tau_{12}^m\right) = f^{-1}\left(\sin\varphi_c\cos\varphi_c\, X_C\right) = f^{-1}\left(\frac{1}{2}\sin(2\varphi_c)\, X_C\right) \tag{3.17}$$

The resulting expression depends on the particular form of the constitutive shear law and, in the general case, the evaluation of φ_0 requires an iterative solution procedure.

Once the initial misalignment angle has been determined, the remaining unknown in Eq. 3.13 is the shear strain γ_m. For a generic loading condition, γ_m can be obtained by solving:

$$f(\gamma_m) = -\sin\varphi\cos\varphi\,(\sigma_1 - \sigma_2^{\psi}) + (\cos^2\varphi - \sin^2\varphi)\,|\tau_{12}^{\psi}|$$

Under the small-angle approximation, the previous expression becomes:

$$f(\gamma_m) \simeq (\varphi_0 + \gamma_m)(-\sigma_1 + \sigma_2^{\psi}) + |\tau_{12}^{\psi}| \tag{3.18}$$

The use of $|\tau_{12}^{\psi}|$ instead of τ_{12}^{ψ} allows the simultaneous consideration of both positive and negative initial fibre misalignments [47]. The resulting equation depends on the constitutive shear law and, in the general case, must be solved iteratively.

For materials exhibiting linear elastic behaviour in shear, the constitutive law reduces to $\tau_{12}^{m} = G_{12}\gamma_m$ and the previous expressions simplify considerably. In particular, the shear strain at failure (Eq. 3.17) becomes:

$$\gamma_{m_c} = \frac{\sin(2\varphi_c)\,X_C}{2G_{12}} \simeq \frac{\varphi_c X_C}{G_{12}} \tag{3.19}$$

under the small-angle approximation. Moreover, the shear strain for a generic loading condition (Eq. 3.18) can be written explicitly as:

$$\gamma_m = \frac{\varphi_0(-\sigma_1 + \sigma_2^{\psi}) + |\tau_{12}^{\psi}|}{G_{12} + \sigma_1 - \sigma_2^{\psi}} \tag{3.20}$$

3.3.7 In-situ strengths

Experimental evidence has shown that the transverse tensile and shear strengths of a ply embedded within a multidirectional laminate are generally higher than those measured for the same ply in a unidirectional laminate [43]. This effect is commonly referred to as the *in-situ effect* and is mainly attributed to the mechanical constraint imposed by the adjacent plies, which limits the initiation and propagation of transverse micro-cracks within the embedded ply.

In particular, under the same stress state, crack propagation is significantly less favourable in thin embedded plies than in equivalent plies within unidirectional laminates [47, 48]. As a consequence, material strengths obtained from standard experimental characterization tests based on unidirectional laminates may underestimate the actual ply strengths within a multidirectional laminate [43].

The in-situ strengths depend on both the ply thickness and its position within the laminate. In general, thinner plies exhibit higher in-situ strengths than thicker ones. Moreover, embedded plies are generally characterized by higher strengths than outer plies because the free surface of outer plies facilitates crack initiation and propagation [8, 13, 47].

In-situ strengths are used in a number of failure criteria and the methods adopted for their evaluation vary across the literature [43]. Table 3.1 reports the expressions

proposed in LaRC05. Unlike phenomenological criteria such as Hoffman, where the mechanical response of the material does not directly influence the evaluation of the FI, in LaRC05 the constitutive behaviour of the material also affects the failure prediction through the in-situ strengths.

In particular, the in-situ strengths are derived from a fracture mechanics analysis of an idealized slit crack in an unidirectional ply and depend on both the elastic properties and the constitutive response of the material.

Physically, this crack represents a distribution of defects in the composite material: matrix–fibre debonds, matrix voids, or clusters of densely packed fibres, resulting from manufacturing [8, 48].

	Transverse tensile strength		Longitudinal shear strength		Transverse shear strength	
	Linear	Nonlinear	Linear	Nonlinear	Linear	Nonlinear
UD	Y_T		S_L		$S_T = Y_C \cos(\alpha_0)\left(\sin(\alpha_0) + \frac{\cos(\alpha_0)}{\tan(2\alpha_0)}\right)$	
Thick embedded	$1.12\sqrt{2}Y_T$	$\xi_2^{-1}\left(1.12^2\xi_2(Y_T)\right)$	$\sqrt{2}S_L$	$\xi_L^{-1}\left(2\xi_L(S_L)\right)$	$\sqrt{2}S_T$	$\xi_T^{-1}\left(2\xi_T(S_T)\right)$
Thin embedded	$\sqrt{\frac{8G_{Ic}^L}{\pi h \Lambda}}$	$\xi_2^{-1}\left(\frac{2G_{Ic}^L}{\pi h}\right)$	$\sqrt{\frac{8G_{IIc}^L G_{12}}{\pi h}}$	$\xi_L^{-1}\left(\frac{4G_{IIc}^L}{\pi h}\right)$	$\sqrt{\frac{8G_{IIc}^L G_{12}}{\pi h}}$	$\xi_T^{-1}\left(\frac{4G_{IIc}^L}{\pi h'}\right)$
Thin outer	$\sqrt{\frac{4G_{Ic}^T}{\pi h \Lambda}}$	$\xi_2^{-1}\left(\frac{G_{Ic}^T}{\pi h}\right)$	$\sqrt{\frac{4G_{IIc}^T G_{12}}{\pi h}}$	$\xi_L^{-1}\left(\frac{2G_{IIc}^T}{\pi h}\right)$	$\sqrt{\frac{8G_{IIc}^T G_{12}}{\pi h}}$	$\xi_T^{-1}\left(\frac{2G_{IIc}^T}{\pi h'}\right)$

Table 3.1: Formulae for in-situ strengths in LaRC05 (from [48])

The parameters appearing in Table 3.1 are defined as follows:

- h is the thickness of the considered ply, while $h' = h/\cos\alpha_0$
- Λ is a parameter depending on the elastic properties of the ply material:

$$\Lambda = 2\left(\frac{1}{E_2} - \frac{\nu_{12}^2}{E_1}\right)$$

- $\xi_2(\sigma)$, $\xi_L(\tau)$ and $\xi_T(\tau)$ are functions representing the area under the stress–strain curve up to the point (ε, σ) for transverse tension, longitudinal shear and transverse shear, respectively:

$$\xi_2(\sigma) = \int_0^{\varepsilon(\sigma)} \sigma_2 \, d\varepsilon_2 \qquad \xi_L(\tau) = \int_0^{\gamma(\tau)} \tau_L \, d\gamma_L \qquad \xi_T(\tau) = \int_0^{\gamma(\tau)} \tau_T \, d\gamma_T$$

  These functions are obtained from interpolation of the experimental stress–strain curves corresponding respectively to transverse tensile, longitudinal shear and transverse compression tests [48].

- G_{Ic}^L, G_{Ic}^T, G_{IIc}^L and G_{IIc}^T are the longitudinal and transverse intralaminar fracture toughnesses of the material constituting the considered ply [48]. Additional information regarding the selection of fracture toughness values is provided in Section 4.7.

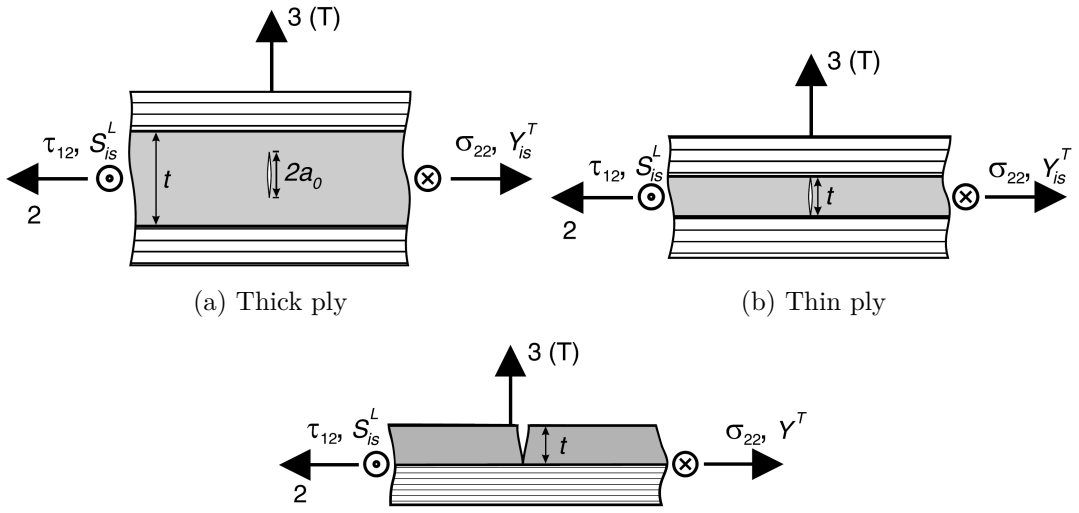
The first row of Table 3.1 corresponds to plies belonging to a unidirectional laminate, for which the in-situ strengths are assumed equal to the standard material strengths. The remaining rows refer to plies embedded within multidirectional laminates and are organized according to the different ply types shown in Fig. 3.6, namely thick embedded plies, thin embedded plies and thin outer plies.

Dvorak and Laws [16] estimated the transition thickness between thin and thick plies to be approximately 0.7 mm, corresponding to about 5–6 plies for typical aerospace laminates.

For each strength, two formulations are reported depending on the constitutive relation considered. The "Linear" columns correspond to the case of linear elastic constitutive behaviour, namely $\sigma_2 = E_2\varepsilon_2$, $\tau_L = G_{12}\gamma_L$ and $\tau_T = G_{12}\gamma_T$.

In this case, the corresponding strain-energy-density functions become:

$$\xi_2(\sigma) = \frac{\sigma_2^2}{2E_2} \qquad \xi_L(\tau) = \frac{\tau_L^2}{2G_{12}} \qquad \xi_T(\tau) = \frac{\tau_T^2}{2G_{12}}$$



(a) Thick ply

(b) Thin ply

(c) Thin outer ply

Figure 3.6: Idealized models adopted for the derivation of in-situ strengths for thick embedded, thin embedded and thin outer plies. (from [8] , with permission from Elsevier, License Number 6278711312248)

Theoretical background The energy release rate G represents the amount of elastic energy released by the structure per unit increase of crack surface area, and therefore

quantifies the energy available for crack propagation. It is defined as [47]:

$$G = -\frac{\partial \Pi}{\partial A}$$

where Π is the potential energy of the system and A is the crack surface area (or crack length in two-dimensional problems).

Crack propagation occurs when the available energy release rate reaches a critical value G_c, experimentally determined for the considered material system. The critical energy release rate therefore represents the minimum energy required to generate a unit area of new fracture surface, and consequently quantifies the resistance of the material to crack propagation.

In fracture mechanics, crack propagation mechanisms are commonly classified according to the relative displacement of the crack faces.

Mode I corresponds to opening loading, in which the crack faces separate under a normal stress acting perpendicular to the crack plane. In laminated composites, this mechanism is typically associated with transverse tensile stresses.

Mode II corresponds to in-plane sliding (shear) loading, in which the crack faces slide relative to each other under shear stresses acting on the crack plane. In the LaRC04/LaRC05 formulation, both the in-plane shear stress τ_{12} and the transverse shear stress τ_{23} are associated with Mode II crack propagation [47].

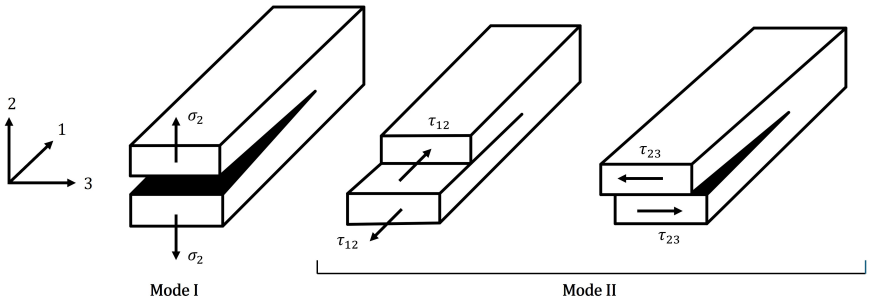


Figure 3.7: Idealized Mode I and Mode II intralaminar crack loading conditions associated with σ_{22}, τ_{12} and τ_{23} in LaRC04/05

The base relations between intralaminar fracture toughnesses and in-situ strengths from which the formulations reported in Table 3.1 are derived are the following [48]:

$$G_{Ic} = Y\,\frac{\pi a_0}{m}\,4\xi_2\left(Y_T^{is}\right); \qquad G_{IIc}^{L} = Y\,\frac{\pi a_0}{m}\,\xi_L\left(S_L^{is}\right); \qquad G_{IIc}^{T} = Y\,\frac{\pi a_0}{m}\,\xi_T\left(S_T^{is}\right)$$

where Y is a geometry-dependent factor, m is equal to either 2, for unstable crack propagation in the transverse direction, or 4, for unstable propagation in the longitudinal direction, and a_0 is the half-length of the transverse slit crack [48].

The distinction between the longitudinal (L) and transverse (T) fracture toughnesses is related to the preferential crack-growth direction within the ply.

In thick embedded plies, the slit crack can propagate both in the transverse and in the longitudinal directions. Fracture-mechanics analysis shows that crack growth in the transverse direction is energetically favoured, leading to unstable transverse propagation until the crack reaches the constraining adjacent plies.

Conversely, in thin plies the crack extends across the ply thickness and propagation in the transverse direction is suppressed by the surrounding plies. As a consequence, crack growth can only occur in the longitudinal direction or trigger delamination at the ply interfaces.

The thin outer ply can be regarded as a particular case of a thin embedded ply in which one constraining interface is replaced by a free surface, resulting in reduced resistance to crack propagation and therefore lower in-situ strengths.

3.4 Remarks on the considered criteria

- LaRC05 criterion is developed for unidirectional plies, whereas the Hoffman criterion can also be applied to fabric-based composite materials.
- The increased predictive capability of the LaRC-based approach comes at the cost of a more demanding material characterization. In particular, the identification of intralaminar fracture toughness values and the nonlinear shear response is required, potentially for each material in the laminate.
- The LaRC formulation shows higher sensitivity to material parameters, especially those related to fracture toughness and shear nonlinearity, which can significantly influence the predicted failure response.
- From a computational standpoint, the Hoffman criterion is straightforward to implement and numerically robust, while the LaRC formulation is more complex and require additional care in numerical implementation.
- Although the two criteria are formulated under different stress assumptions (2D for Hoffman and 3D for LaRC05), their comparison is still meaningful as it highlights two fundamentally different approaches to failure prediction.

3.5 Margin of Safety for composite laminates

When evaluating the structural performance of laminated composite structures, it is important not only to detect failure conditions but also to quantify the available safety margin.

For this purpose, the *Strength Ratio* (SR) represents a more informative failure metric than the Failure Index. While the FI only indicates whether a failure condition has been reached (i.e. $FI \geq 1$), the SR provides a direct measure of how much the applied load can be scaled before failure occurs. In general, the Strength Ratio is defined as:

$$SR = \frac{\text{Allowable Stress}}{\text{Calculated Stress}}$$

The Strength Ratio can be interpreted as the factor by which the current stress state must be scaled to reach failure. For instance, an SR value of 1.2 implies that the applied loads could be increased by 20% before reaching the failure condition. In contrast, a Failure Index of 0.8 only indicates that failure has not yet occurred, without directly quantifying the available margin [38].

For design purposes, it is often more convenient to express structural capacity in terms of Margin of Safety (MOS) rather than Strength Ratio. As discussed in section 2.4, when a global safety factor (SF) is included, the MOS can be written as:

$$MOS = \frac{\text{Allowable Stress}}{SF \cdot \text{Calculated Stress}} - 1 = \frac{SR}{SF} - 1$$

However, in contrast to isotropic materials, laminated composites do not exhibit a single allowable stress value that can be directly compared to the computed stress state. This is due to their anisotropic nature and the presence of multiple failure mechanisms.

Moreover, no universal equivalent stress measure exists that can uniquely represent the multiaxial stress state for all failure modes. As a result, classical MOS formulation based on a single allowable stress is not directly applicable.

The approach adopted here for the computation of the MOS is consistent with the methodology described in [38] for polynomial failure criteria, such as Tsai–Wu and Hoffman. In this framework, the stress state is scaled by an unknown Strength Ratio (SR), while the safety factor (SF) is directly included in the scaled stresses before substitution into the failure criterion. By imposing the failure condition ($FI = 1$), the corresponding value of SR is determined. Since the safety factor is already included in the stress scaling procedure, the MOS is finally computed as:

$$MOS = SR - 1$$

3.5.1 Hoffman Criterion

The Hoffman criterion includes both linear and quadratic terms (see Eq. 3.1). By scaling the stress components as $\sigma_i \rightarrow SR{\cdot}SF{\cdot}\sigma_i$ and substituting them into the failure criterion, the resulting expression becomes quadratic in SR. Imposing the failure condition $FI = 1$ therefore leads to the following second-order equation in SR:

$$\Big(F_{11}\sigma_1^2 + F_{22}\sigma_2^2 + F_{12}\sigma_1\sigma_2 + F_{66}\sigma_{12}^2\Big)SF^2SR^2 + \Big(F_1\sigma_1 + F_2\sigma_2\Big)SF\,SR - 1 = 0$$

The resulting equation has the form $a\,SR^2 + b\,SR + c = 0$, whose solutions are:

$$SR_{1,2} = \frac{-b \pm \sqrt{b^2 - 4ac}}{2a}$$

with:

$$a = \Big(F_{11}\sigma_1^2 + F_{22}\sigma_2^2 + F_{12}\sigma_1\sigma_2 + F_{66}\sigma_{12}^2\Big)SF^2, \quad b = \Big(F_1\sigma_1 + F_2\sigma_2\Big)SF, \quad c = -1$$

In general, it cannot be excluded that both solutions are positive, due to the asymmetric tensile and compressive strengths of composite materials. Therefore, the smallest positive value of SR must be selected in order to ensure a conservative estimate of the MOS.

3.5.2 LaRC05 Criteria

Fibre tensile failure

Considering fibre tensile failure (see Eq. 3.3), at failure the condition $FI = 1$ is satisfied. Therefore:

$$\frac{SR_{FT} \cdot SF \cdot \langle \sigma_1 \rangle_+}{X_T} = 1 \implies SR_{FT} = \frac{X_T}{SF \cdot \langle \sigma_1 \rangle_+} = \frac{1}{SF \cdot FI_{FT}}$$

Consequently:

$$MOS_{FT} = \frac{1}{SF \cdot FI_{FT}} - 1 \tag{3.21}$$

Due to the linear form of this failure index, the minimum MOS corresponds to the maximum value of FI_{FT}.

When $\sigma_1 < 0$, it follows that $FI_{FT} = 0$. In this case, fibre tensile failure is not activated and the corresponding MOS is not mathematically defined, as it involves division by FI_{FT}, and not physically meaningful.

Matrix failure

For matrix failure (see Eq.3.4 and 3.5), the expressions used to compute σ_N, τ_L and τ_T depend linearly on σ_2, σ_3, τ_{23} and τ_{31}. Therefore, applying the SF to the stress components is equivalent to applying it directly to σ_N, τ_L and τ_T.

At failure, including the SF, the following nonlinear equation in terms of the SR is obtained:

$$\begin{aligned} f(SR) = \left(\frac{SF \cdot SR \cdot \tau_T}{S_T^{is} - \eta_T \cdot SF \cdot SR \cdot \sigma_N} \right)^2 + \left(\frac{SF \cdot SR \cdot \tau_L}{S_L^{is} - \eta_L \cdot SF \cdot SR \cdot \sigma_N} \right)^2 \\ + \left(\frac{SF \cdot SR \cdot \langle \sigma_N \rangle_+}{Y_T^{is}} \right)^2 - 1 = 0 \end{aligned} \tag{3.22}$$

If $\langle \sigma_N \rangle_+ > 0$, the function $f(SR)$ leads to a sixth-degree polynomial equation, whereas if $\langle \sigma_N \rangle_+ = 0$, it reduces to a fourth-degree equation. In both cases, no closed-form analytical solution is available and the equation must therefore be solved numerically.

The existence of real positive solutions can be investigated through the asymptotic behaviour of the function $f(SR)$. Evaluating the function at $SR = 0$ yields $f(0) = -1$. Therefore, if the limit of $f(SR)$ for $SR \to +\infty$ is positive, the existence of at least one real root is guaranteed.

From a physical standpoint, a monotonic increase of $f(SR)$ with respect to SR is expected, since increasing SR corresponds to a proportional increase in the applied stress state and therefore to a progressive approach to the failure condition. Under this assumption, the positive root is unique whenever it exists.

The asymptotic behaviour of the function is given by:

$$\lim_{SR\to+\infty} f(SR) = \begin{cases} +\infty & \text{if } \sigma_N >= 0 \\ \frac{\tau_T^2}{\eta_T^2\sigma_N^2} + \frac{\tau_L^2}{\eta_L^2\sigma_N^2} - 1 & \text{if } \sigma_N < 0 \end{cases}$$

Therefore, if $\sigma_N \geq 0$, the limit diverges to $+\infty$ and the existence of at least one real positive solution of $f(SR) = 0$ is guaranteed. Conversely, if $\sigma_N < 0$, the limit assumes a finite value, which may be negative. In this case, the function may not intersect the zero level, and therefore failure may never be reached.

From a physical standpoint, when $\sigma_N \geq 0$, the normal stress contributes to matrix crack opening through the last term of the criterion, which increases with the stress level and drives the function towards failure.

Conversely, when $\sigma_N < 0$, the normal stress is compressive and does not contribute to crack opening, so that the last term vanishes. In addition, the denominators of the shear-related terms increase, reducing the contribution of shear stresses to the failure index. Physically, compressive normal stress promotes crack closure, thereby inhibiting matrix failure and possibly preventing the failure condition from being reached.

Moreover, it is worth noting that the asymptotic value of the function is independent of the SF.

Finally, the function $f(SR)$ exhibits two vertical asymptotes, corresponding to the zeros of the denominators:

$$SR_1 = \frac{S_T^{is}}{\eta_T\, SF\, \sigma_N}, \quad SR_2 = \frac{S_L^{is}}{\eta_L\, SF\, \sigma_N}$$

These asymptotes define regions where the function is not continuous and must be properly accounted for in the numerical solution procedure. It is worth noting that SR_1 and SR_2 have the same sign as σ_N. In particular, if $\sigma_N < 0$, both SR_1 and SR_2 are negative. Since, by definition, $SR \geq 0$, the vertical asymptotes do not affect the solution domain and therefore do not introduce numerical issues.

Fibre kinking failure

The formulation adopted for the computation of the MOS associated with fibre kinking failure is analogous to that derived for matrix failure. By imposing the condition $FI = 1$ on the fibre kinking criterion (see Eq. 3.10) and scaling the stress components by the SR and the SF, the following nonlinear equation is obtained:

$$g(SR) = \left(\frac{SF \cdot SR \cdot \tau_{23}^m}{S_T^{is} - \eta_T \cdot SF \cdot SR \cdot \sigma_2^m}\right)^2 + \left(\frac{SF \cdot SR \cdot \tau_{12}^m}{S_L^{is} - \eta_L \cdot SF \cdot SR \cdot \sigma_2^m}\right)^2 + \left(\frac{SF \cdot SR \cdot \langle \sigma_2^m \rangle_+}{Y_T^{is}}\right)^2 - 1 = 0 \tag{3.23}$$

The function exhibits asymptotic properties analogous to those discussed for matrix failure. In particular:

$$\lim_{SR \to +\infty} g(SR) = \begin{cases} +\infty & \text{if } \sigma_2^m \geq 0 \\ \frac{(\tau_{23}^m)^2}{\eta_T^2 (\sigma_2^m)^2} + \frac{(\tau_{12}^m)^2}{\eta_L^2 (\sigma_2^m)^2} - 1 & \text{if } \sigma_2^m < 0 \end{cases}$$

Similarly to the matrix failure case, the function also exhibits vertical asymptotes corresponding to the zeros of the denominators.

3.5.3 Remarks

- The present approach is valid under the assumption of linear elastic behaviour, as it relies on the proportional scaling of the stress state. Therefore, it is recommended to use results obtained from linear static analyses (e.g. SOL 101 in MSC Nastran).

- FI values obtained from different failure criteria should not be directly compared, as they do not represent a physical quantity and are defined through criterion-dependent formulations. This limitation is particularly relevant when fundamentally different failure theories are considered (e.g. LaRC05 and Hoffman).

  In fact, the Failure Index only provides information on whether a failure condition has been reached (i.e. $FI \geq 1$), and therefore allows for a qualitative comparison limited to identifying whether failure is predicted or not. However, comparing FI values to assess which criterion predicts a state closer to failure is not meaningful.

  In contrast, the Strength Ratio (and the derived MOS) represents the scaling factor required to reach the failure condition, thus providing a quantitative and physically meaningful measure of the distance from failure. For this reason, MOS values provide a consistent basis for comparison across different failure criteria.

- For the failure criteria considered, no direct relationship exists between the FI and the MOS. The only exception is fibre tensile failure in LaRC05, for which a direct relationship was established. In general, the angles that maximize the FI do not coincide with those that minimize the MOS. This applies, for instance, to the angle α in matrix failure and to the angle ψ in fibre kinking failure.

Chapter 4

Failure criteria implementation in Femap API

4.1 Introduction to Femap and Femap API

Femap Femap is a finite element modelling and post-processing environment developed by Siemens, designed to perform engineering analyses in an efficient and reliable way. It allows users to create or import geometries, generate meshes, and define loads and boundary conditions within a single platform.

Additionally, Femap supports interaction with various finite element solvers by enabling the export of input files and the import of analysis results. It also provides essential tools for the visualization and interpretation of simulation outcomes [55].

Femap API In addition to its graphical interface, Femap provides an Application Programming Interface (API) based on OLE/COM technology. In general, an API is an interface that allows software applications to communicate in a structured and controlled way. In the specific case of Femap, the API consists of a set of objects, properties, and methods that enable programmatic interaction with the software through external programming languages.Through this interface, Femap can be controlled via scripts, both internally and from external applications (see Figure 4.1).

Advantages Developing a Femap API script means automating operations that would otherwise be performed manually through the graphical user interface. These tasks can instead be executed programmatically in a faster, more repeatable, and less error-prone manner.

The use of the API is particularly advantageous in scenarios characterized by repetitive operations, manual input of large amounts of data, the management of a high number of entities, or the need for functionalities not available in the standard Femap interface. In many cases, therefore, developing an API-based tool allows one to:

- reduce execution time;

- minimize the risk of human errors;
- create reusable tools for similar tasks on different models;
- share tools with other users, improving overall workflow efficiency;
- automate complex procedures;
- ensure processes that are traceable, repeatable, and independent of the operator.

What Femap API is not It is important to clarify what the Femap API is not. First, it should not be confused with Femap itself: the API is only an interface used to control the software, while scripts developed through it are independent programs that interact with Femap.

Secondly, the API is not a programming language. Languages such as Visual Basic, VBA, Python, or C++ are used to write code that interacts with Femap via the API, but they do not constitute the API itself. In practice, user-written code sends instructions to the API, which reads from and writes data to the Femap database (see Figure 4.1). From this perspective, Femap can be interpreted as a system for storing, managing, and visualizing analysis data.

In this thesis, the term "API" is used, in line with common usage, as a shorthand for both the programmable interface of Femap and the scripts developed through it, although this usage is not strictly accurate.

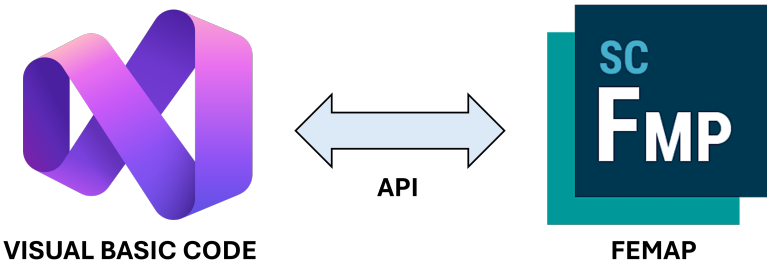


Figure 4.1: API as interface between code and Femap database

Object-oriented programming This paragraph provides the minimal background required to understand the structure of the Femap API. For further details, the reader is referred to the official documentation [54].

The Femap API is based on an object-oriented architecture. All the main entities within Femap, such as nodes, elements, properties, and other model or interface components, are represented as objects. Each object is characterized by properties, which describe its state, and methods, which define the operations that can be performed on it, such as creation, modification, and general interaction.

Femap organizes API objects into three main categories:

- **Application object**: it is unique within each script and represents the active Femap session. It serves as the main entry point to the API and provides access to all other objects. In addition, it allows interaction with the graphical user interface (GUI), including menus and dialog windows, as well as application-level operations such as displaying messages or executing commands. One of its main uses is the creation of tool objects and entity objects.
- **Tool objects**: specialized objects that provide operational functionalities. They do not represent entities stored in the Femap model database, but rather offer utilities to perform specific tasks, such as selecting entities, managing views, or handling data processing operations (e.g., set objects, data table objects, file reading objects).
- **Entity objects**: these represent all the entities stored in the Femap model database. For each type of entity in the model (e.g., nodes, elements, loads, analysis sets), there exists a corresponding API object. These objects are used to create, read, modify, and update model data.

Visual Studio In this work, the Femap API has not been developed using the internal Femap editor, but through Microsoft Visual Studio (as shown in the figure 4.1). Visual Studio is an integrated development environment (IDE) that provides advanced tools for writing, debugging, and managing code.

The choice of Visual Studio is motivated by several advantages. First, it enables the development of stand-alone applications, which can be executed independently from the Femap internal scripting environment. This allows for greater flexibility in structuring the code and managing more complex workflows.

Furthermore, Visual Studio offers a more robust development environment, including features such as code organization, debugging tools, error handling, and user interface design. These capabilities significantly improve code readability, maintainability, and scalability compared to the internal editor.

The code has been developed in VB.NET, which integrates naturally with the OLE/-COM architecture of Femap and facilitates the implementation of object-oriented programming concepts.

4.2 API overview

The first versions of the API addressed in this thesis were developed by Amedeo Grasso in 2018 [20]. One of the main objectives of this thesis is to further develop the existing tool by updating it to ensure compatibility with the most recent versions of Femap, verifying its correct functionality, and enhancing its capabilities.

The updated version of the API allows the evaluation of:

- Failure Indices (FI) and Margins of Safety (MOS) for composite laminates, based on the two theories described in Chapter 3 (applicable to both sandwich panel skins and stand-alone composite laminate structures);

- MOS for metallic skins of sandwich panels, including local instabilities, described in section 2.4;
- MOS for honeycomb cores, described in section 2.4;

User-defined safety factors can be specified and included in the MOS calculations (see subsection 4.6.1). For all operating modes, the API can analyse either the entire Femap model (provided that it satisfies the required conditions, see section 4.6) or selected groups of elements.

Multiple load cases can be processed simultaneously. At the end of the analysis, the minimum MOS for each group is reported for every individual load case as well as across all considered load cases. Complementary information, such as the critical load case ID, the critical element ID, the stress components at the critical location, and other relevant data, is also provided. For composite laminates, the minimum MOS associated with each material present in the analysed layup is reported as well. The results can be exported to an Excel file for further post-processing and documentation. An example of the automatic reporting capabilities of the developed API is presented in Chapter 6.

In addition, depending on the selected operative mode, custom output vectors are generated and made available within the Femap post-processing environment. These vectors enable visualization of the spatial distribution of the computed parameters over the analysed elements, facilitating a more detailed interpretation of the results.

One of the key strengths of the API is its user-friendly graphical interfaces, which allows users to easily select the type of analysis to perform and input the required parameters.

Before describing the functionality in detail (see section 4.6), the updates and improvements introduced in the latest versions are presented. For further details on previous versions (up to version 7.5.4.1), reference is made to Grasso's thesis [20].

4.3 API update

The Femap API developed by Grasso [20] needed to be updated to the latest version of Femap API. Indeed, the API was developed in 2018, and starting from Femap v2020.1 changes have been made. In particular, updates affected the methods for accessing results, the creation and storage of new output vectors, as well as the IDs associated with Nastran solution output vectors. Citing the Femap API guide [54], the main changes are:

- the entire *Output Object* has been deprecated. The *Results Browsing Object* has been enhanced to match the functionality of the *Output Object* and is a more capable and efficient way of retrieving and creating output data.
- The Output Vector ID ranges used in previous versions of Femap are no longer sufficient to accommodate the increasing number of output quantities and element types in modern analyses. Consequently, several output vectors have been reassigned to new ID ranges. For instance, the ID associated with *Plate Bottom von*

Mises Stress was changed from 7033 to 9033 due to a modification in the offset used for plate results.

- All API methods requiring an output vector ID as input in Femap 2019.1 and earlier versions have been deprecated. Updated methods, identified by the suffix *V2*, have been introduced to support the new ID convention.

Because of these changes, the deprecated properties, methods and objects should no longer be used [54]. However, these features are still supported for backward compatibility, although they require the use of pre-2020.1 output vector IDs. Internally, Femap automatically converts legacy vector IDs to the corresponding new IDs and executes the API calls accordingly.

When deprecated properties and/or methods are used, an *obsolete API warning message* is displayed (Figure 4.2), encouraging users to update their scripts to the new *...V2* methods in order to avoid inconsistencies with the output vector IDs shown in the user interface.

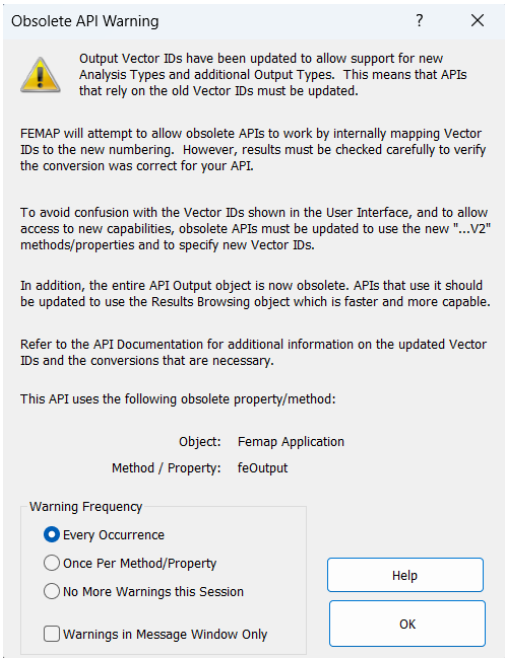


Figure 4.2: Obsolete API warning

Although still functional, reliance on deprecated features is discouraged, as future versions of the API may progressively reduce or remove support for legacy implementations.

To help mitigate the ID changes, a new *ResultsIDQuery Object* has been created to help the user determine the new vector ID of a specific output quantity. This provides the means to acquire vector IDs using a more descriptive keyword approach. In general, a recommended practice is to avoid hardcoding of the vector ID [54].

Before addressing the API updates, a preliminary reverse engineering phase was required. The original codebase, consisting of approximately 5000 lines, contained limited inline comments and only partial external description. Consequently, a significant initial effort was devoted to understanding the logic and structure of the existing implementation.

This phase involved reconstructing the workflow of the previous API version, introducing appropriate comments to improve code readability and maintainability, and progressively replacing deprecated objects and methods with the updated equivalents. Although time-consuming, this activity proved essential not only for ensuring a correct migration to the new API, but also for identifying implementation issues and opportunities for improvement, which are discussed in the following sections.

Further details on the API update process, including examples of upgraded scripts, are provided in Appendix A.

4.4 API improvements

After updating the code and ensuring compatibility with the latest version of Femap, the focus shifted to improving the tool. The original implementation developed by Grasso in [20] provided a solid foundation; however, several enhancements were introduced to improve performance, robustness, user experience, and adherence to the theoretical formulations. The major improvements can be summarized as follow:

- **Graphical user interface**: the graphical user interface has been completely redesigned. Its operation is now based on the opening and management of dedicated forms according to the selected analysis, rather than concentrating all functionalities within a single window. This modular structure improves usability, simplifies the interaction workflow, and makes the interface easier to maintain and extend.

- **All operating modes**: the same analysis can be executed simultaneously on multiple groups. After verifying the compatibility of each group with the selected analysis, the API collects all the required materials and parameters and retrieves them only once. As a result, when two or more groups share the same material or layup, the corresponding information is requested a single time, reducing redundant operations and improving computational efficiency.

- **All operating modes**: in previous versions of the API, the same load case could be processed multiple times when multiple analysis studies were present, often without explicit user awareness, leading to redundant computations and increased execution time. This behavior has been corrected: load cases are now analyzed only once.

- **All operating modes**: the IDs of custom output vectors generated by the API have been standardized (see Appendix A.2) to improve user comprehension and facilitate maintainability.

- **Hoffman/LaRC05**: a constraint has been introduced for both methods requiring that all the elements in a selected group share the same layup. This assumption was already implicitly adopted in previous versions, but no explicit verification was performed.

  By explicitly enforcing this assumption, the data reading process has been significantly optimized: since all elements share the same layup, ply properties can now be stored only once instead of being duplicated for each element. This improvement is particularly relevant for models with a large number of elements.

- **Hoffman**: according to the discussion in section 3.2, the output vector of the maximum FI in absolute value has been removed, as it does not provide meaningful information. Moreover, the evaluation of the maximum FI is now based on its distance from 1 rather than its absolute value.

- **LaRC05**: the implementation of the FI evaluation has been revised to comply with the formulation of the LaRC05 theory, which requires iterative loops over both α, for matrix failure, and ψ, for fibre kinking failure.

  In the previous implementation, the FI for matrix failure was evaluated at discrete values of $\alpha \in [0°, 180°]$. However, instead of identifying the maximum value, separate output vectors were generated for each value of α.

  Furthermore, for the kink failure, no iterative procedure over ψ was performed; a fixed value derived from the earlier LaRC03 [13] formulation was used instead.

- **LaRC05**: the evaluation of the MOS has been introduced (see Section 3.5), including the computation of the minimum MOS for the entire laminate, for each material, and across all load cases. In addition, the possibility to export results to an Excel file has been extended to this theory, consistently with the Hoffman implementation.

- **LaRC05**: in-situ strengths have been incorporated into the evaluation of both the FI and the MOS (see section 4.7). In the previous implementation, the strengths used were those of the material system, implicitly assuming (see Table 3.1) a unidirectional laminate. These values were applied uniformly to all ply types (embedded, outer, thin, and thick), even when the theory was used for multidirectional composites.

- **Sandwich panel analyses**: Support has been added for the analysis of sandwich panels with composite laminate skins and honeycomb cores when modelled using 2D laminate elements.

- **Sandwich panel analyses**: The calculation of the dimpling MOS for metallic skins has been added. Furthermore, the formulations used for the calculation of the instability MOS have been revised to ensure consistency with those reported in section 2.4.

4.5 Implementation aspects of the LaRC05 formulation

4.5.1 Numerical solution of nonlinear equations

With reference to 3.5.2, the following subsection describes the numerical method adopted to solve the nonlinear equations $f(SR)$ (Eq. 3.22) and $g(SR)$ (Eq. 3.23) for the computation of the corresponding MOS values in the LaRC05 formulation.

In both cases, the bisection method has been adopted due to its robustness with respect to the nonlinear characteristics of the functions. This method requires the specification of four parameters: a tolerance on the absolute value of $f(SR)$ or $g(SR)$ for convergence, the maximum number of iterations, and two initial points defining the bracketing interval for the root-finding procedure.

In this implementation, the iterative procedure is terminated when either a tolerance of 10^{-6} on $|f(SR)|$ or $|g(SR)|$ is achieved or a maximum number of 100 iterations is reached. These parameters are fixed by design and cannot be modified by the user. In practice, convergence is typically achieved in fewer than 30 iterations.

For the bisection method to be applicable, the selected interval must satisfy the condition $f(a)\,f(b) < 0$ (or equivalently $g(a)\,g(b) < 0$). The definition of this interval depends on the asymptotic behaviour of the functions. Considering $f(SR)$ as an example, the sign of σ_N is first evaluated:

- If $\sigma_N \geq 0$, the existence of a solution is guaranteed. However, particular attention must be paid to the presence of vertical asymptotes. To avoid them, the upper bound of the interval is defined as the minimum between 10^5, chosen as a sufficiently large upper limit for SR, and 99% of the smallest positive asymptotic limit. Therefore, the initial bracketing interval becomes:

$$\left[0,\ \min\left(0.99 \cdot \min\left(\frac{S_T^{is}}{\eta_T\, SF\, \sigma_N}, \frac{S_L^{is}}{\eta_L\, SF\, \sigma_N}\right), 10^5\right)\right]$$

- If $\sigma_N < 0$, the existence of a solution is not guaranteed. In fact, in this case the asymptotic value of function is finite:

$$FI_{lim} = \lim_{SR \to +\infty} f(SR) = \frac{\tau_T^2}{\eta_T^2 \sigma_N^2} + \frac{\tau_L^2}{\eta_L^2 \sigma_N^2} - 1$$

  If this limit is positive, the existence of a real positive root is guaranteed and the interval:

$$[0,\ 10^5]$$

  is adopted for the bisection procedure. Conversely, if the asymptotic value is negative, the function never reaches the failure condition and no real positive solution exists.

It is possible that no root is found within the specified interval. In such cases, the SR is not determined by the bisection procedure and is considered effectively unbounded.

Accordingly, a conventional large value ($MOS = 10^{15}$) is assigned. This value should not be interpreted as physically meaningful, but rather as a finite numerical representation of an infinite MOS. Furthermore, when the asymptotic value of the failure index satisfies:

$$0 < FI_{lim} < 1$$

the failure condition cannot be achieved for any value of SR, and the corresponding Strength Ratio is not defined. If this condition is verified for all values of α, the matrix failure mode is not activated for the considered stress state. In such cases, the element is excluded from the result visualization and from the computation of the minimum MOS.

The numerical procedure adopted for the solution of $g(SR)$ in the fibre kinking criterion is fully analogous to that described for $f(SR)$, replacing σ_N, τ_T and τ_L with σ_2^m, τ_{23}^m and τ_{12}^m, respectively.

4.5.2 Implementation of in-situ strengths formulations and shear nonlinearity

For typical composite materials, the stress–strain response parallel to the fibres under both tension and compression is approximately linear. In contrast, the response under transverse tension and compression, as well as in shear, exhibits a pronounced nonlinearity, primarily governed by the behaviour of the polymer matrix [30, 48, 50]. Accurately capturing this nonlinear behaviour within the constitutive model is essential to obtain a reliable stress field at the ply level. This, in turn, is a prerequisite for accurate laminate failure predictions [48, 50]. An example of the nonlinear longitudinal shear and transverse compression behaviour is shown in Figure 4.3.

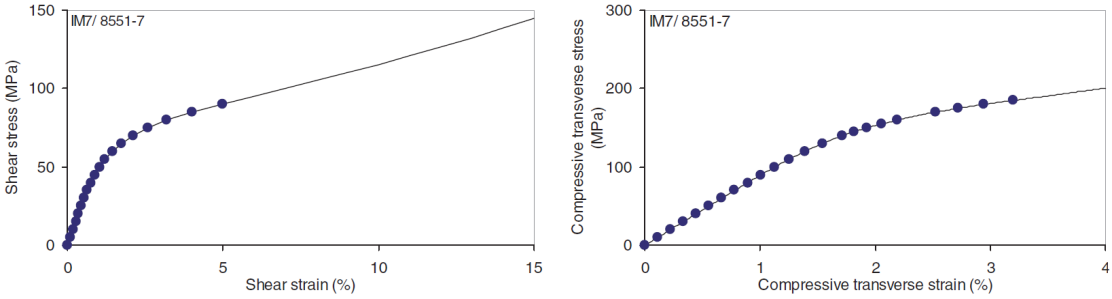


Figure 4.3: Example of nonlinear longitudinal shear and transverse compression stress–strain responses of IM7/8551-7 ((from [48], with permission from SAGE Publications, License Number 6278710457725))

Within the LaRC05 framework, the influence of the material constitutive response is particularly relevant in the evaluation of in-situ strengths. As described in Section 3.3, the approach proposed in LaRC05 [48] involves deriving the functions $\xi_2(\sigma)$, $\xi_L(\tau)$ and $\xi_T(\tau)$ from experimental stress–strain curves, which are then used to evaluate the in-situ strengths (see Table 3.1).

However, in practical applications, such experimental curves are often unavailable. Furthermore, as highlighted in [48], extrapolating these curves from limited experimental data requires additional assumptions, introducing a degree of subjectivity, particularly in the identification of key features such as inflection points.

In the present work, an alternative approach was therefore sought in order to account for the nonlinear material response while still retaining closed-form formulations for the evaluation of the in-situ strengths. In other words, a compromise was pursued between implementation practicality, availability of the required input data, and fidelity with experimental observations. From this perspective, the analytical model proposed by Catalanotti in [9], which is fully consistent with LaRC05 formulation, was considered the most suitable alternative.

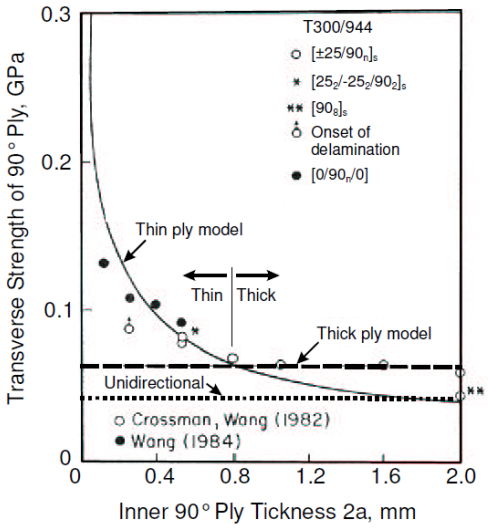


Figure 4.4: In-situ transverse tensile strength predictions as a function of ply thickness based on linear formulations (from [47])

Transverse tensile strength According to the LaRC05 formulation, a complete modelling framework would require accounting for the nonlinear transverse tensile response through the function ξ_2. However, as shown in [47, 8, 9], the use of formulations derived under the assumption of a linear stress–strain response provides good agreement with experimental results, as illustrated in Figure 4.4.

For this reason, and consistently with several implementations of LaRC04 and LaRC05 [2, 9, 19, 7], only the linear formulation for the transverse tensile in-situ strength is adopted in the present work.

Longitudinal shear strength In accordance with the approaches proposed in [47, 8, 9], the nonlinear longitudinal shear response is modelled using the polynomial constitutive relationship originally proposed by Hahn and Tsai in [22]:

$$\gamma_L = \frac{\tau_L}{G_{12}} + \beta\tau_L^3$$

where β is the *shear response factor*. With this formulation, the characterization of the nonlinear constitutive response is reduced to the identification of a single parameter β from experimental shear stress–strain data. Substituting the constitutive relation into the definition of ξ_L yields:

$$\xi_L(\tau) = \int_0^{\gamma(\tau)} \tau_L \, d\gamma_L = \frac{\tau^2}{2G_{12}} + \frac{3}{4}\beta\tau^4$$

By inverting the previous relation, the following closed-form expression is obtained:

$$\tau = \xi_L^{-1}(\xi_L) = \sqrt{\frac{\sqrt{1+\beta\phi G_{12}^2} - 1}{3\beta G_{12}}} \quad \text{with} \quad \phi = 12\,\xi_L \tag{4.1}$$

Following the LaRC05 formulations reported in Table 3.1, the longitudinal in-situ shear strength S_L^{is} is obtained by substituting into Eq. 4.1 the appropriate expression of ϕ corresponding to the considered ply typology:

- thick embedded ply: $\xi_L = 2\xi_L(S_L) = \frac{S_L^2}{G_{12}} + \frac{3}{2}\beta S_L^4 \implies \phi = \frac{12S_L^2}{G_{12}} + 18\beta S_L^4$
- thin inner ply: $\xi_L = \frac{4G_{IIc}^L}{\pi h} \implies \phi = \frac{48G_{IIc}^L}{\pi h}$
- thin outer ply: $\xi_L = \frac{2G_{IIc}^T}{\pi h} \implies \phi = \frac{24G_{IIc}^T}{\pi h}$

It can be verified that the nonlinear formulation asymptotically reduces to the linear elastic solution for $\beta \to 0$. However, due to the structure of Eq. 4.1, the linear solution cannot be obtained by directly substituting $\beta = 0$, and the limit must instead be evaluated analytically.

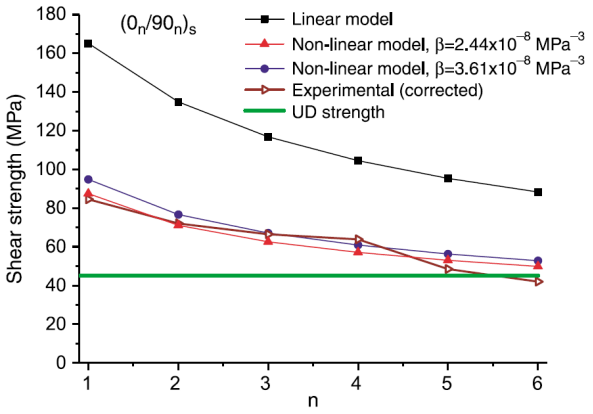
Using this formulation, Camanho et al. [8] demonstrated excellent agreement between the predicted in-situ longitudinal shear strengths and experimental results. Their study considered a T300/1034 CFRP laminate with layup $(0_n/90_n)_s$ and a nominal ply thickness of 0.127 mm. The corresponding results are reported in Figure 4.5a, where the experimental measurements are compared with both linear and nonlinear predictions as a function of the number n of plies within each sublaminate.

Several important observations can be drawn from these results. First, the in-situ longitudinal shear strength decreases as adjacent plies with identical orientation are stacked together, consistently with the progressive reduction of the constraining effect exerted by neighbouring plies. Second, the linear elastic formulation significantly overestimates the in-situ strength, particularly for thin plies. For the case $n = 1$, the relative

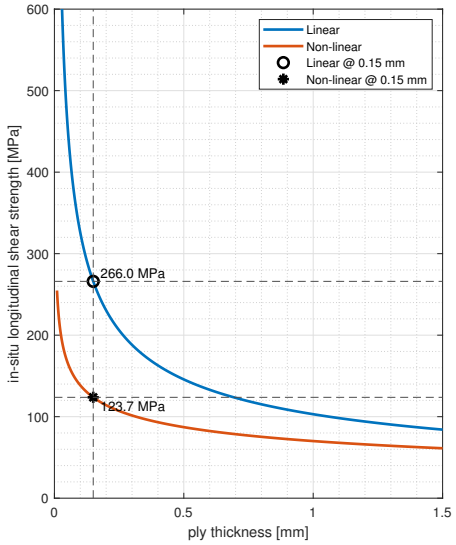
error between the experimental value and the linear prediction is approximately +95.5%. In contrast, the nonlinear formulation provides a much more accurate estimate, with a relative error of approximately −3.6%. Finally, the relatively small variation obtained using different values of β suggests that the model is not excessively sensitive to the precise identification of the nonlinear parameter [8].

Figure 4.5b shows the variation of the predicted in-situ longitudinal shear strength as a function of ply thickness using both linear and nonlinear formulations. The material properties correspond to the IM7/8552 CFRP prepreg reported in Table 5.1, characterized by a nominal ply thickness of 0.131 mm, representative of aerospace composite laminates. For the nominal ply thickness, the linear formulation overestimates the in-situ strength by approximately 115% with respect to the nonlinear prediction.

The results presented in Figures 4.5a and 4.5b clearly demonstrate that neglecting the nonlinear longitudinal shear response leads to severe overestimations of the in-situ shear strength, particularly for thin plies, where the in-situ effect is most pronounced.



(a) Comparison with experimental data (from [8], , with permission from Elsevier, License Number 6278711312248)



(b) Prediction as a function of ply thickness

Figure 4.5: In situ longitudinal shear strength: linear and non-linear predictions

It is important to note that the adopted shear constitutive law must also be consistently taken into account in the evaluation of the kinking FI/MOS, specifically through the evaluation of the shear strain under longitudinal compression γ_{m_c} (Eq. 3.17) and in general loading condition γ_m (Eq. 3.18). In the linear case, closed-form solutions are obtained (Eq. 3.19 and 3.20). Conversely, when the nonlinear Hahn–Tsai formulation is adopted, γ_{m_c} in evaluated as follow (accordingly to Eq. 3.17):

$$\gamma_{m_c} = \frac{\sin(2\phi_c) \cdot X_C}{2\,G12} + \beta(\sin(\phi_c)\cos(\phi_c)X_C)^3 \tag{4.2}$$

and, for the calculation of γ_m, the following nonlinear equation must be solved iteratively:

$$\gamma_m = \frac{(\phi_0 + \gamma_m)(\sigma_2^{\psi} - \sigma_1) + |\tau_{12}^{\psi}|}{G_{12}} + \beta[(\phi_0 + \gamma_m)(\sigma_2^{\psi} - \sigma_1) + |\tau_{12}^{\psi}|]^3 \tag{4.3}$$

The previous equation does not always admit a solution. In the developed API, if γ_m cannot be evaluated for all the considered values of ψ, the kink-mode FI/MOS for the corresponding element is considered undefined. Consequently, the element is excluded from the graphical output vectors and is not taken into account in the evaluation of the maximum FI or minimum MOS.

Moreover, it's important to analyse the effect of the non-linear term in the γ_{m_c} formulation. To do that, consider again the IM7/8552 CFRP prepreg (Table 5.1). For this material (considering the value of $S_{L_{is}}$ obtained with the non linear formulation):

$$\phi_c = 6.44° \; ; \quad \frac{\sin(2\phi_c) \cdot X_C}{2\,G12} = 0.0253 \;\; rad \;\; ; \quad \beta(\sin(\phi_c)\cos(\phi_c)X_C)^3 = 0.0714 \;\; rad$$

The previous example highlights that the nonlinear contribution is not negligible in the evaluation of γ_{m_c}. For this material system, the cubic term is approximately 2.8 times larger than the corresponding linear contribution, leading to a significant variation of the initial fiber misalignment angle ϕ_0.

More importantly, the effect of the nonlinear constitutive law is not limited to the evaluation of γ_{m_c}. The resulting value of ϕ_0 directly affects the calculation of γ_m, while the governing equation used to evaluate γ_m is itself modified by the introduction of the nonlinear cubic term. Furthermore, the nonlinear formulation also influences the calculation of the in-situ strengths and of the angle ϕ_c.

Consequently, the linear and nonlinear formulations do not differ by a simple correction factor, but rather by the underlying kinematic and constitutive description of the kinking mechanism. For this reason, similar kinking FI/MOS predictions should not be expected a priori. The differences between the two approaches may become significant, particularly for materials exhibiting a pronounced nonlinear shear response.

Transverse shear strength Rather than introducing an explicit nonlinear constitutive law for the transverse shear response, as previously done for the longitudinal shear behaviour, the present implementation exploits the structure of the LaRC05 matrix failure criterion to derive a direct relationship between the in-situ transverse shear strength S_T^{is} and the longitudinal in-situ shear strength S_L^{is}.

As shown in Section 3.3.5, under pure transverse compression the matrix failure index assumes the form:

$$FI_M = \frac{(Y_C^{is})^2 \sin^2\alpha \, \cos^2\alpha}{\left(S_T^{is} + \eta_T \, Y_C^{is} \cos^2\alpha\right)^2}$$

At failure, both the following condition must be satisfied:

$$\begin{cases} FI_M\big|_{\alpha=\alpha_0} = 1 \\ \dfrac{\partial FI_M}{\partial \alpha}\Big|_{\alpha=\alpha_0} = 0 \end{cases}$$

Assuming the relationship between the friction parameters proposed by Puck [50]:

$$\frac{\eta_L}{\eta_T} = \frac{S_L^{is}}{S_T^{is}}$$

the system can be solved analytically, leading to closed-form expressions for both Y_C^{is} and S_T^{is}. In particular, the following expression is obtained for the in-situ transverse shear strength:

$$S_T^{is} = \frac{(2\sin^2\alpha_0 - 1)}{\eta_L \sin(2\alpha_0)} S_L^{is}$$

This relation is adopted in the present implementation for the nonlinear formulation. The parameter η_L is evaluated using Eq. 3.9.

The relation is used only within the nonlinear formulation for two main reasons. First, LaRC05 already provides closed-form expressions for S_T^{is} under linear elastic assumptions. Second, as discussed in the previous subsection, the linear formulation significantly overestimates the longitudinal in-situ shear strength S_L^{is}. Since the previous expression directly relates S_T^{is} to S_L^{is}, its use together with the linear formulation would consequently propagate the same overestimation to the prediction of the transverse in-situ shear strength.

Conclusions The expressions adopted for the in-situ strengths and implemented in the present work are summarized in Table 4.1.

	Y_T^{is}	S_L^{is}		S_T^{is}	
Configuration	Linear	Linear	Nonlinear	Linear	Nonlinear
UD	Y_T	S_L		$S_T = Y_C\cos(\alpha_0)\left(\sin(\alpha_0) + \frac{\cos(\alpha_0)}{\tan(2\alpha_0)}\right)$	
Thick embedded	$1.12\sqrt{2}Y_T$	$\sqrt{2}S_L$	$\sqrt{\frac{\sqrt{1+\beta\,\phi\,G_{12}^2}-1}{3\,\beta\,G_{12}}}$ with $\phi = \frac{12\,S_L^2}{G_{12}} + \frac{72}{4}\beta\,S_L^4$	$\sqrt{2}S_T$	$\frac{2\sin^2(\alpha_0)-1}{\eta_L\sin(2\alpha_0)}\,S_L^{is}$
Thin embedded	$\sqrt{\frac{8G_{Ic}^L}{\pi h\Lambda}}$	$\sqrt{\frac{8G_{IIc}^L G_{I2}}{\pi h}}$	$\sqrt{\frac{\sqrt{1+\beta\,\phi\,G_{12}^2}-1}{3\,\beta\,G_{12}}}$ with $\phi = \frac{48\,G_{IIc}^L}{\pi h}$	$\sqrt{\frac{8G_{IIc}^L G_{I2}}{\pi h}}$	$\frac{2\sin^2(\alpha_0)-1}{\eta_L\sin(2\alpha_0)}\,S_L^{is}$
Thin outer	$\sqrt{\frac{4G_{Ic}^T}{\pi h\Lambda}}$	$\sqrt{\frac{4G_{IIc}^T G_{I2}}{\pi h}}$	$\sqrt{\frac{\sqrt{1+\beta\,\phi\,G_{12}^2}-1}{3\,\beta\,G_{12}}}$ with $\phi = \frac{24\,G_{IIc}^T}{\pi h}$	$\sqrt{\frac{8G_{IIc}^T G_{I2}}{\pi h}}$	$\frac{2\sin^2(\alpha_0)-1}{\eta_L\sin(2\alpha_0)}\,S_L^{is}$

Table 4.1: In-situ strength formulas implemented in the API

Accounting for nonlinear material behaviour significantly increases the complexity of the formulation. In particular, it requires additional material parameters and reliable experimental data describing the nonlinear constitutive response, which are not always readily available for all material systems. This limitation affects the practical applicability of nonlinear models. Nevertheless, such complexity is justified by the strong influence

of shear nonlinearity on the prediction of in-situ strengths, especially in thin plies, where linear models are known to provide non-conservative strength overestimations.

Despite these limitations, linear formulations remain used in engineering practice and commercial software [2, 8, 15]. While they may be acceptable at preliminary design stages, their limitations must be clearly understood, particularly with respect to the potential overestimation of in-situ strengths.

Conversely, assuming that in-situ strengths are equal to the corresponding lamina strengths (i.e., neglecting in-situ effects) is equivalent to implicitly considering a unidirectional laminate configuration. This represents a conservative assumption and may lead to an underestimation of the actual structural performance. In practical applications, it is therefore preferable to account for in-situ effects and address model uncertainties through appropriate safety factors, rather than neglecting them altogether.

It should also be noted that, for ply thicknesses below approximately 0.1 mm, both linear and nonlinear formulations tend to provide inaccurate predictions of in-situ strengths. In fact, with the presented formulations, the in situ strengths asymptotically tend to infinity when the thickness approaches zero [9]. This limitation should be taken into account when applying the proposed models to very thin-ply laminates.

An example of the evaluation of in-situ strengths for a representative material system is provided in Section 5.1.

As discussed by Catalanotti in [9], the proposed formulations have been extensively validated for conventional composite laminates manufactured with thermosetting resins and characterized by ply thicknesses typically ranging between 0.1 mm and 0.2 mm.

4.6 User guide

This section describes the analyses that can be performed using the developed API and the data required for each of them. The starting interface of the application is shown in Figure 4.6. From this window, the user must select both the type of analysis to be performed and the portion of the FEM model to be analysed.

The analyses available in the API are divided into two main categories: *Composite Laminate FI/MOS* and *Sandwich Panel MOS*, which are described respectively in subsections 4.6.2 and 4.6.3.

The workflow of the API is organized as follows. First, the main interface requires a set of general input parameters. Then, according to the selected analysis, additional forms are automatically opened to collect all the data required for the specific analysis.

The execution of the analysis is enabled only when all the required input data have been correctly provided. Until all mandatory fields are completed, the *Evaluate* button remains disabled. Missing or incomplete inputs are automatically highlighted in red in order to clearly identify the information still required by the API.

Regarding the model scope, the user can choose to analyse either the entire FEM model or only selected groups. The full model can be analysed only if all the elements share the same property and are compatible with the selected analysis type. Otherwise, the model must be divided into groups and analysed separately.

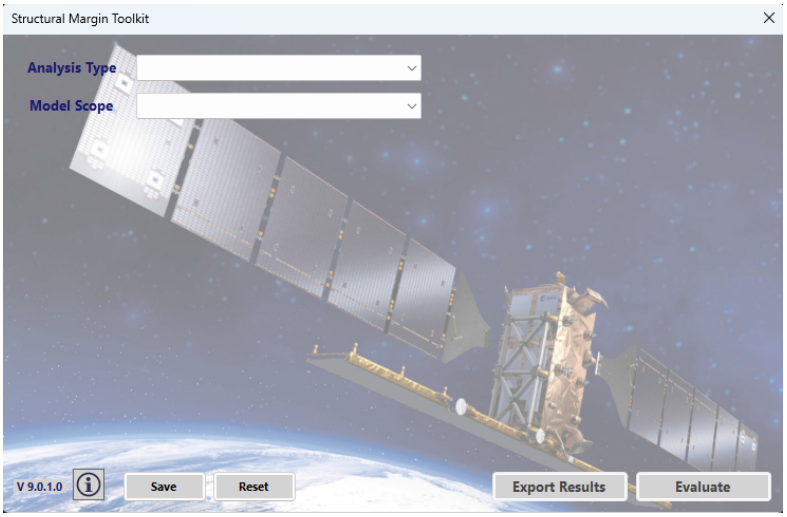


Figure 4.6: Starting interface of the API

If the *group mode* option is selected, the IDs of the groups to be analysed must be inserted into the dedicated textbox, separated by commas (see, for example, Figure 4.7). Before starting the computation, the API automatically performs a series of checks on each selected group. These checks verify both the existence of the specified group IDs and the compatibility of the contained elements with the selected analysis type.

For example, if the analysis *Metallic Skin + Honeycomb (2D Laminate)* is selected, all the elements inside the groups must be 2D laminate elements and the associated layups must consist of exactly three plies: first skin, honeycomb core, and second skin. Conversely, if the analysis *Honeycomb Solid Core (3D)* is selected, all the groups must contain only 3D solid elements.

One of the main strengths of the developed API is the possibility of analysing multiple groups simultaneously. In this case, the API automatically identifies the input data required for each group and requests each parameter only once, even when the same information is shared among different groups.

Before going in depth with every type of analysis, some general remarks regarding the use of the API are listed below:

- The standard units adopted in both the FEM model and the Nastran results must be m and Pa;
- In all API forms, decimal values must be entered using "." as the decimal separator;
- The API reads the material and element databases available in the FEM model at the moment the API is executed. Therefore, the analysed load cases must refer to the current mesh configuration and to the current material properties stored in the model database;
- In the input forms of the API, the notation adopted for the different parameters is

consistent with the symbols introduced in Sections 2.4, 3.2 and 3.3, according to the selected analysis. Therefore, for a detailed definition and physical meaning of each parameter, the reader should refer to the corresponding theoretical sections.

- Details regarding the output vectors generated for each analysis are reported in Appendix A.

4.6.1 Safety factor

Whenever a MOS evaluation is performed, the definition of a safety factor is required. Within the developed API, the overall safety factor is defined as the product of multiple independent contributions according to the ESA standard ECSS-E-ST-32-10C [17]:

$$SF = QSF \cdot DSF \cdot ASF \cdot SF_u$$

where:

- QSF (*Qualification Safety Factor*): factor applied to define the *qualification load*, i.e. the load level to which the structural component shall be subjected during qualification testing;
- DSF (*Design Safety Factor*), expressed as the product of *Model Safety Factor*, to account for uncertainties in mathematical models when predicting dynamic response, loads, and evaluating load paths, and *Project Safety Factor*, to account for the maturity of the program (e.g. stability of the mass budget, well-identified design) and the confidence in the specification given to the project;
- ASF (*Additional Safety Factor*): factor introduced as a load magnification term in specific design conditions to account for additional uncertainties or inaccuracies not covered by other safety factors;
- SF_u (*Ultimate Safety Factor*): factor associated with ultimate strength requirements.

For metallic skins, if yielding MOS evaluations are requested, the factor SF_u is replaced by the yielding safety factor SF_y, specifically prescribed for yielding verification.

4.6.2 *Composite Laminates FI/MOS* Mode

If the analysis type *Composite Laminates FI/MOS* is selected, the user must choose both the failure criterion and whether to evaluate only the FI, only the MOS, or both (see Figure 4.7).

It is important to underline that the API is designed to be used only with elements associated with linear or parabolic 2D laminate properties (PCOMP). Three-dimensional laminates and equivalent PSHELL properties are not supported.

If LaRC05 is selected as failure criterion, the user must also specify the thickness limit above which a ply is considered thick. This parameter is required for the evaluation of

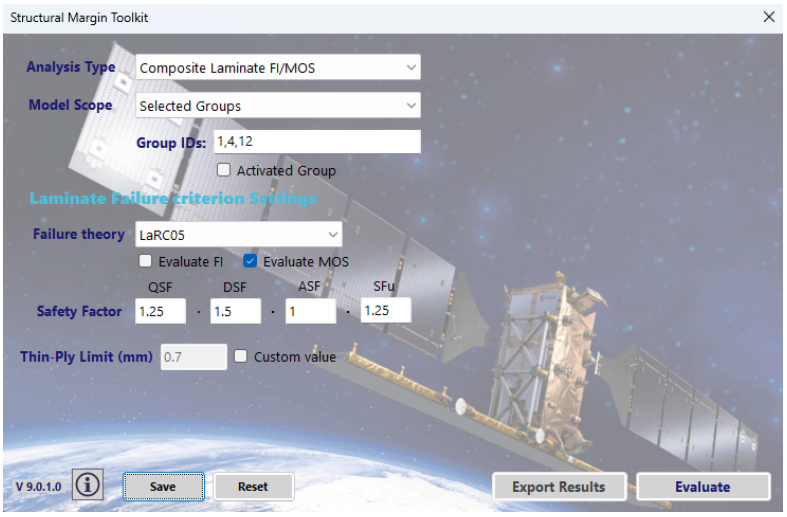


Figure 4.7: *Composite Laminates FI/MOS* interface

the in-situ strengths and therefore affects the material data requested by the API. The default value is initialized to $0.7\,mm$, in agreement with the results proposed by Dvorak and Laws [16] (for further details, see subsection 3.3.7).

For each ply of the laminate, the minimum MOS, the corresponding element ID and, in the case of LaRC05, the associated failure mode are printed in the Femap *Message Window*. At the end of the analysis, the overall minimum MOS and its associated properties are also reported.

In industrial practice, carbon-fabric plies are commonly used as the outermost plies of composite laminates. Unlike Hoffman criterion, which does not distinguish between ply types, LaRC05 is not directly applicable to fabric plies.

For these types of laminates, it is recommended to perform two separate analyses: one using Hoffman criterion and one using LaRC05 criterion. The Hoffman results should then be used for the fabric plies, while the LaRC05 results should be considered for the remaining unidirectional plies.

Hoffman Criterion If Hoffman criterion is selected, no additional inputs are required. The material strengths are directly read from the Femap database.

Nastran also provides FI and MOS values based on Hoffman criterion. The comparison performed between the values calculated by Nastran and those obtained through the developed API showed a good agreement. Depending on the analysed load case, the relative error generally does not exceed 10^{-5}.

LaRC05 Criterion First of all, it is important to reiterate the assumptions underlying the implemented LaRC05 formulation. When calculating FI and MOS using LaRC05, σ_3 is assumed equal to zero because this stress component is not returned by Nastran for the considered element type.

To model multilayer structures (PCOMP), Nastran adopts a kinematic expansion based on Classical Lamination Theory (CLT), which does not directly provide the out-of-plane stress component. The evaluation of σ_3 would instead require theories based on layer-wise kinematic expansions.

When LaRC05 is selected as failure criterion, the first form displayed by the API is the one reported in Figure 4.8. For each analysed group, the user must specify whether the laminate has to be treated as unidirectional (UD) or multidirectional (MD). A third option, namely *MD treated as UD*, is also available.

This choice was intentionally left to the analyst as a design feature of the API. In principle, the laminate type could be automatically identified from the stacking sequence available in the FEM database. However, allowing the analyst to explicitly select the laminate modelling assumptions provides greater flexibility in the analysis process.

In particular, even when the laminate is multidirectional, the analyst may intentionally choose to process it as a UD laminate in order to neglect in-situ effects and therefore obtain more conservative results. Moreover, for multidirectional laminates, fracture toughness values must be specified for each material appearing inside the layup, and these data are not always available (see section 4.7).

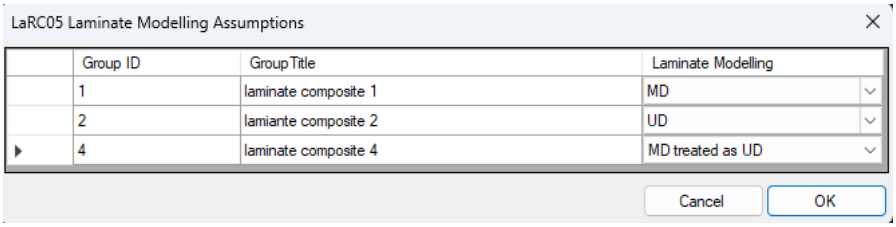


Figure 4.8: *LaRC05 Laminate Modelling Assumptions* interface

After the laminate modelling assumptions have been selected for each group, the API automatically identifies all the material data required by the analysed groups and requests them through the form reported in Figure 4.9.

If a material appears inside a multidirectional laminate with thin plies, all the material properties are required, including fracture toughness values. Conversely, if the material appears only in UD laminates or in MD laminates with thick plies, fracture toughness values are not required.

The parameter η_T is evaluated starting from α_0, while η_L is evaluated starting from both α_0 and the material strengths (respectively Eqs. 3.7 and 3.9). In all cases, the user can additionally specify a value for β.

If $\beta = 0$, the in-situ strengths are evaluated using the linear formulation. Conversely, if $\beta \neq 0$, the nonlinear formulation proposed by Hahn and Tsai [22] is adopted (see Table 4.1).

When visualizing the LaRC05 output vectors, the activated failure mode depends on the sign of σ_1. Tensile failure or kinking failure are therefore activated according to the local stress state. Elements for which a given failure mode is not active are displayed in grey.

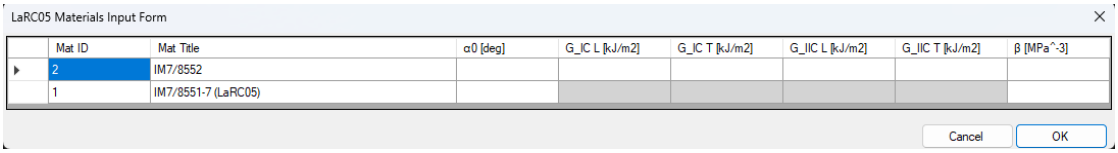


Figure 4.9: *LaRC05 Material Input* interface

If, for an entire ply, one failure mode is never activated (for example, if $\sigma_1 \geq 0$ for all the elements or $\sigma_1 < 0$ for all the elements), an "invalid" vector is generated and a warning message is printed in the Femap *Message Window*. In the case of FI, the invalid vector is filled with zeros, whereas in the case of MOS the invalid vector is filled with values equal to 10^{16}.

For both FI and MOS evaluations, the angular discretization is fixed to $\Delta\alpha = 5°$ and $\Delta\psi = 5°$. These values are defined within the implementation and are not user-adjustable. This choice is consistent with the considerations reported in the original LaRC04 [47] and LaRC05 [48] formulations, where it is shown that a very fine angular discretization of the interval [0°,180°] is not required in order to accurately identify the critical angle value.

Furthermore, when examining the output vectors associated with the LaRC05 failure modes, the following convention is adopted: `1` = fibre tensile failure, `2` = matrix failure, and `3` = fibre kinking failure.

4.6.3 *Sandwich Panel MOS* Mode

If the analysis type *Sandwich Panel MOS* is selected, the user must choose, through the dedicated *Sandwich Model* box, the sandwich modelling approach adopted or the specific part of the structure to be analysed (see, for example, Figure 4.10). Each available option is described in the following paragraphs.

Laminate Facesheets Only (2D laminate) This mode is identical to the *Composite Laminates FI/MOS* analysis previously described, with the only difference that only MOS values are evaluated. The procedure and required inputs remain unchanged. The distinction is purely conceptual and was introduced to group all the tools related to sandwich panel verification within the same analysis category.

Laminate + Honeycomb (2D laminate) The operating principle of this mode is similar to that adopted for isolated laminate skins modelled as 2D laminates. In this case, however, both the skins and the honeycomb core are represented within the same layup definition. For this reason, the user must first specify, through a dedicated form, the ply ID corresponding to the honeycomb core inside each analysed layup.

The user can also select the failure criterion adopted for the composite skins. If LaRC05 is selected, the same input data required for isolated laminate analyses must

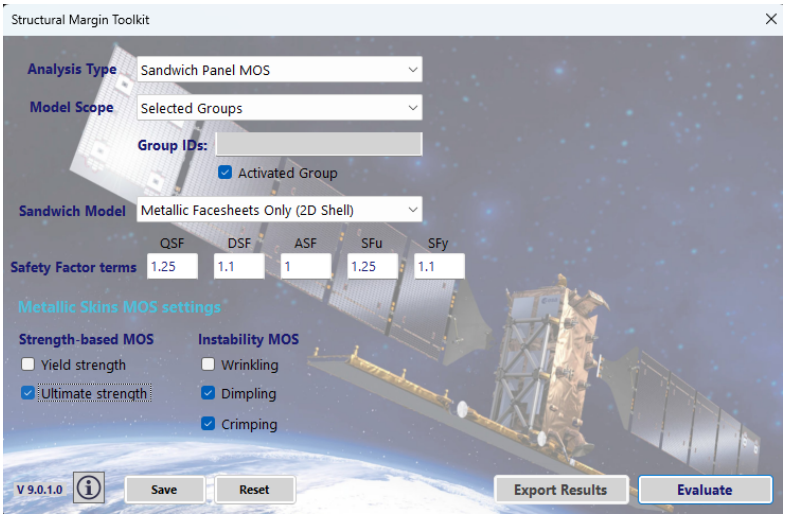


Figure 4.10: *Sandwich Panel MOS* Interface

be provided (Figures 4.8 and 4.9). In addition, the honeycomb material strengths are required through the input form reported in Figure 4.13.

Metallic Facesheets Only (2D shell) In this mode, the MOS related to metallic skins are evaluated. In this modelling approach, each group is assumed to contain only one skin. From the starting interface, the user can select which MOS calculations have to be performed (see Figure 4.10). This choice directly affects the parameters requested in the form reported in Figure 4.12.

First, the API requests the strength properties of all the metallic materials appearing inside the analysed groups (Figure 4.11). Subsequently, the geometrical and mechanical properties of the sandwich panel associated with each skin are required (Figure 4.12).

This is the analysis mode requiring the largest amount of user input data, because the procedure cannot be fully automated through the Femap database. In particular, for dimpling calculations, not only the thickness of the analysed skin (t_1) must be specified, but also the thicknesses of both the honeycomb core (t_c) and the opposite skin (t_2).

The same limitation applies to the honeycomb properties: when the honeycomb core is modelled using solid elements, Femap does not provide a direct automatic association between a skin and its corresponding honeycomb core. Consequently, all the related material properties (compressive modulus E_c, lower flatwise strength F_c, minimum shear modulus G_c) must be manually specified.

Metallic + Honeycomb (2D laminate) The approach adopted in this mode is similar to the one described in the previous paragraph. In this case, however, the thicknesses of the skins and the honeycomb core are directly known from the laminate layup definition.

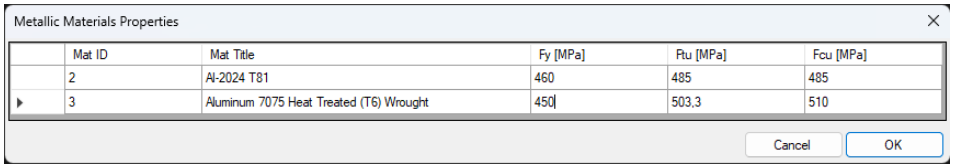


Figure 4.11: *Metallic Materials Properties* Interface

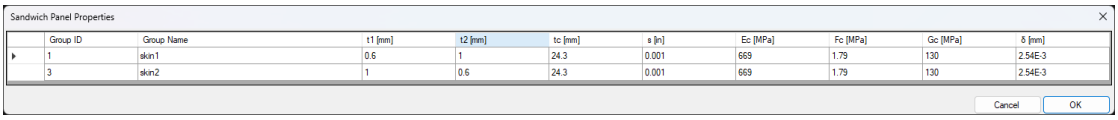


Figure 4.12: *Sandwich Panel Properties* Interface

Moreover, a specific honeycomb core is automatically associated with each layup. As a consequence, the honeycomb properties, namely E_c, F_c and G_c, are requested only once together with the corresponding material strengths.

If wrinkling MOS evaluation is requested, an additional form is opened requiring the specification of the initial waviness of both skins together with the lower flatwise strength F_c of the honeycomb core.

Honeycomb Solid core (3D) In this mode, only the MOS associated with the honeycomb core are evaluated. The user is required to provide the honeycomb shear strengths through the dedicated input form reported in Figure 4.13. The requested data are specified for each honeycomb material appearing inside the analysed groups.

4.7 Fracture toughnesses

The fracture toughness values required for the evaluation of the in-situ strengths represent some of the most difficult material parameters to obtain reliably. In addition to the limited availability of experimental data, considerable ambiguity is often found in the literature regarding the definition, notation and physical meaning of these quantities.

For this reason, the present section was specifically included to clarify the assumptions adopted in this work and provide the user with practical guidelines for the conscious and consistent selection of the required input parameters.

Terminology Dealing with fracture toughness in composite materials is inherently complex. As highlighted by Swolfs et al. in [65], multiple aspects must be taken into account.

Firstly, it is worth noting that the term *fracture toughness* can be referred both to critical energy release rate G_c or to the critical stress intensity factor K_c. When it is not explicitly specified in the literature, the distinction can generally be inferred from the physical dimensions: G has units of energy per unit area (typically kJ/m^2 or N/mm), whereas K is expressed in MPa$\sqrt{\text{m}}$.

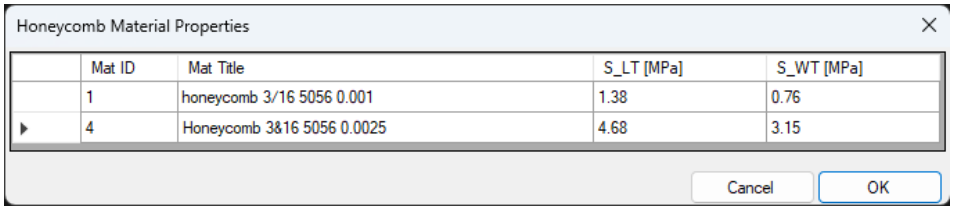


Figure 4.13: *Honeycomb Materials Properties* Interface

In composite laminates, different types of fracture toughness can be identified depending on both the crack growth direction and the orientation of the fracture surface with respect to the laminate. However, a universally accepted terminology is still lacking, which requires careful interpretation of the literature.

The framework proposed by Swolfs et al. [65] distinguishes two independent features: the crack growth direction (longitudinal, transverse, or through-thickness) and the crack surface orientation (intralaminar, interlaminar, or translaminar). Their combination leads to six possible cases. In particular (see Figure 4.15):

- **Intralaminar**: the crack propagates within a single ply, without crossing ply interfaces;
- **Interlaminar**: the crack propagates along the interface between adjacent plies, leading to delamination;
- **Translaminar**: the crack crosses the plies, breaking both fibres and matrix.

Unless otherwise specified, fracture toughness values reported in the literature often refer to interlaminar fracture toughness, due to its direct relevance to delamination phenomena. For this reason, such values are frequently regarded as interface properties.

Different works may adopt different definitions for the crack propagation directions. In particular, the terminology used in the LaRC theories differs from the classification introduced above.

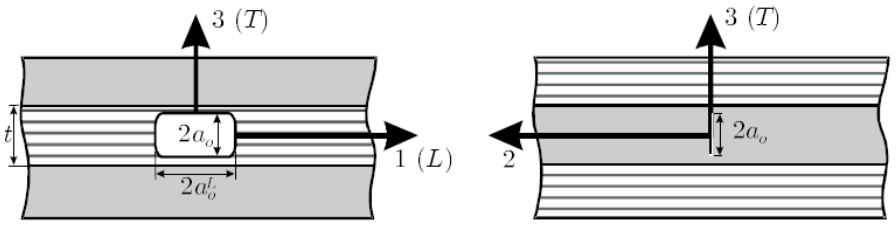


Figure 4.14: Slit crack geometry (from [47])

Within the LaRC framework (see Figure 4.14), the transverse direction (T) corresponds to the 3-direction, i.e. the through-thickness direction of the laminate, whereas

in the classification by Swolfs et al. the transverse direction denotes the 2-direction, i.e. the in-plane direction perpendicular to the fibres.

Therefore, the same term "transverse" may refer to different physical directions depending on the adopted convention, and fracture toughness data must be interpreted accordingly. Given the lack of a universally accepted terminology and the potential for ambiguity, a consistent convention must be adopted. In this work, the nomenclature used in the LaRC theories is followed throughout.

Accordingly, Figure 4.15 illustrates the independent ply-level failure mechanisms in a unidirectional laminate, while Figure 4.16 highlights the intralaminar crack propagation directions associated with the fracture toughnesses considered in LaRC05. Although Figure 4.16 refers to a unidirectional laminate, it is representative of the local behaviour of an individual ply within a multidirectional laminate, which is the reference framework adopted in LaRC theories.

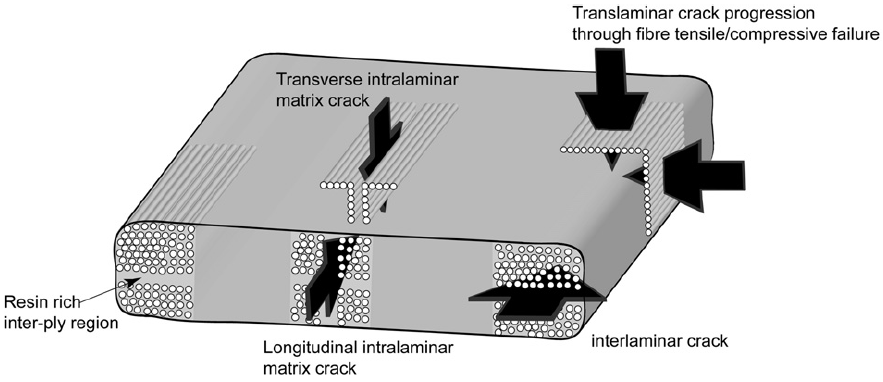


Figure 4.15: Overview of ply-level failure modes (from [35], with permission from Elsevier, License Number 6278730749245)

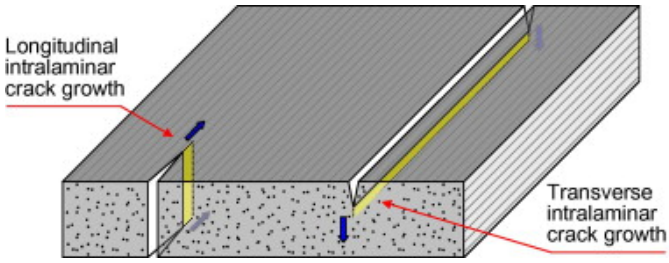


Figure 4.16: Transverse and longitudinal intralaminar crack growth (from [46], with permission from Elsevier, License Number 6278730972880)

Fracture toughness as a material property The second difficulty highlighted by Swolfs et al. in [65], concerns whether fracture toughness in composite materials can be regarded as a purely material property. For this to be the case, it should (i) be

independent of the testing laboratory, operator, or equipment, (ii) not depend on the laminate layup, and (iii) be size-independent. However, it is not evident that fracture toughness in composites fully satisfies these requirements [65, 51].

Firstly, a common issue in fracture toughness testing is the definition of the crack initiation point. Accurate measurement of the initiation toughness (i.e. the value required in LaRC criteria) is highly sensitive to both the data reduction method, i.e. procedures used to extract toughness values from load–displacement curves, and the crack observation technique [65, 44]. Indeed, many test methods are based on measuring the load and displacement at which a delamination of known length starts to propagate [51].

For example, in interlaminar fracture toughness testing, in order to improve repeatability, Robinson and Hodgkinson [51] report different approaches to identify the onset of delamination based on specific points of the load–displacement curve, rather than relying on visual inspection, which is highly operator-dependent.

Regarding the influence of the laminate layup, it has been shown that translaminar fracture toughness, in this case expressed in terms of stress intensity factors, depends on the laminate layup [49]. Moreover, standard tests for interlaminar fracture toughness typically require symmetric laminates with only 0° plies (i.e. unidirectional laminates) [51, 44]. As a result, the measured toughness values are representative of 0°/0° interfaces only and may not be fully representative of all interface configurations.

Regarding size effects, the influence of ply thickness on the intralaminar fracture toughness associated with longitudinal failure has been extensively investigated [19, 18]. As summarized by Furtado et al. in [19], some authors reported an apparent increase in fracture toughness with ply thickness, often attributed to variations in fibre pull-out length, and therefore suggested treating it as an in-situ property.

However, the results presented in [19] indicate that this apparent dependence is mainly due to subcritical damage mechanisms, such as longitudinal splitting, which promote stress redistribution. When these mechanisms are properly accounted for, the intralaminar fracture toughness can be considered independent of the ply thickness.

Nevertheless, this issue remains debated in the literature. Different interpretations coexist, with some studies supporting a thickness-dependent behaviour, while others suggest that the observed increase in fracture toughness is primarily associated with structural damage mechanisms rather than intrinsic material properties [65].

These examples demonstrate that it is not straightforward to establish whether the fracture toughnesses of composite laminates can be regarded as true material properties. Although not exhaustive, they highlight the inherent difficulties associated with the definition and use of these quantities.

Conclusions In this work, consistently with most of the referenced literature, fracture toughness is treated as a property of the material system, i.e. of the fibre–matrix combination.

The *in-situ* strengths in LaRC theories depend specifically on the *intralaminar* matrix fracture toughness [48]. In principle, four values are required: longitudinal and transverse fracture toughness (see figure 4.16), each for Mode I and Mode II loading conditions.

However, these values are not always available or easily measurable [48], and the available experimental data are limited [65]. Therefore, as also discussed in LaRC05 [48], reasonable assumptions are often required in practical applications.

4.7.1 Comparison of interlaminar and intralaminar fracture toughness

From a physical standpoint, both interlaminar and intralaminar fracture processes are governed by matrix-dominated failure mechanisms. For this reason, their associated fracture toughness values are expected to be of the same order of magnitude [46, 35, 9]. Nevertheless, it must be noted that the fracture mechanisms are not identical: interlaminar fracture typically occurs within resin-rich layers at ply interfaces, whereas intralaminar fracture involves the matrix–fibre interface [14]. Therefore, the equivalence between the two cannot be assumed a priori and requires experimental validation. However, the experimental characterization of these properties differs significantly in terms of maturity and standardisation.

Interlaminar fracture toughness has been extensively investigated due to its key role in delamination analysis. As a result, several standardised test methods have been developed and adopted [65]. In particular, standards from ISO, ASTM, ESIS and JIS define well-established procedures. For Mode I loading, the most common test is the Double Cantilever Beam (DCB), while for Mode II loading widely used configurations include the End-Notched Flexure (ENF) and the End-Loaded Split (ELS) tests [51].

Despite this level of standardisation, these methods are primarily developed for unidirectional laminates and typically involve crack propagation along the fibre direction (longitudinal direction) [51]. Even in this relatively simple configuration, some experimental difficulties remain, particularly for Mode II loading.

In contrast, intralaminar fracture toughness characterization is far less developed. This is mainly due to experimental challenges such as fibre bridging, the difficulty of isolating matrix-dominated failure mechanisms, and the lack of standardised procedures, especially regarding specimen geometry and crack initiation methods, including the difficulty of introducing a well-defined and sharp intralaminar pre-crack [14, 46, 11, 9].

The similarity between interlaminar and intralaminar fracture toughnesses is also supported by the literature. In [11], several experimental studies on different carbon/epoxy systems are reviewed, showing that the ratio between Mode I intralaminar and interlaminar fracture toughness generally remains close to unity, typically ranging from values slightly below 1 up to approximately 2.4 depending on the material system, specimen configuration and data reduction method. The observed variability is mainly attributed to inaccuracies and inconsistencies in the measurement of intralaminar fracture toughness, particularly due to the experimental difficulties described previously. Moreover, the results presented in [11] indicate that, when properly defined pre-cracks are introduced, the initiation values of interlaminar and intralaminar fracture toughness become approximately equivalent.

In [14], it is shown that, for a carbon/epoxy unidirectional laminate, the intrinsic *longitudinal* Mode I fracture toughness (excluding fibre bridging effects) is comparable for interlaminar and intralaminar cases. Similarly, in [46], it is observed that Mode I

transverse interlaminar fracture toughness values are close to the transverse intralaminar ones for different carbon/epoxy systems (e.g. HSC/SE84LV and T300/913).

It should also be noted that significant experimental difficulties already arise in the characterization of Mode II interlaminar fracture toughness, even for crack propagation along the fibre direction. These challenges are expected to be even more pronounced for intralaminar fracture, for which reliable experimental data are considerably more limited.

Conclusions Given the limited availability of intralaminar fracture data, practical applications often rely on simplifying assumptions. As discussed by Catalanotti in [9], it is common practice to approximate transverse intralaminar fracture toughness using longitudinal interlaminar fracture toughness. In line with the approach adopted in [47, 48, 2], and based on the literature discussed above, the following assumptions are considered acceptable in this work:

- Longitudinal and transverse fracture toughness can be considered equal as a first approximation:
$$G_{I_C}^L \simeq G_{I_C}^T, \qquad G_{II_C}^L \simeq G_{II_C}^T$$
- Intralaminar fracture toughness values can be approximated using interlaminar fracture toughness values [44].

Nevertheless, the implemented API allows the user to specify different fracture toughness values for each direction.

For carbon/epoxy systems, typical ranges reported in the literature for interlaminar (and, by approximation, intralaminar) fracture toughness are:

$$G_{I_C} \approx 0.2 - 0.6\, kJ/m^2, \qquad G_{II_C} \approx 0.7 - 1.8\, kJ/m^2$$

However, these values may vary significantly depending on the specific material system. A summary of interlaminar fracture toughness values for different carbon/epoxy systems, for both Mode I and Mode II, is reported in [53].

In conclusion, although the adopted assumptions introduce a certain level of approximation, they are consistent with common engineering practice and supported by available experimental evidence. This approach enables the practical implementation of LaRC05 criteria even in the absence of a complete intralaminar fracture characterization.

Chapter 5

Validation case studies

This Chapter presents the case studies used to validate the API implementation of the LaRC05 failure criterion and to highlight the differences between the predictions obtained with LaRC05 and the Hoffman criterion.

The selected case studies provide a representative overview of different stress states and failure mechanisms. Although not exhaustive, they cover fundamental loading conditions and include the presence of stress concentrations, thus providing a meaningful validation set for the proposed API.

The correctness of the LaRC05 implementation was verified by comparing the API predictions with the results obtained from independent MATLAB scripts implementing the individual failure modes separately, whereas the Hoffman implementation was validated through comparison with the corresponding results provided by Nastran.

5.1 Material Properties and In-Situ Strengths

The unidirectional carbon/epoxy prepreg system HexPly IM7/8552 was selected for the following examples. This intermediate-modulus carbon fibre and toughened epoxy resin system is widely used in the aerospace industry for primary structural components [33, 27]. For example, all composite structures on the Eurofighter Typhoon, including wings, front fuselage, and tail section, are built with HexPly IM7/8552 [26].

All the material properties required for the application of the LaRC05 criterion and for the definition of the Nastran material card are reported in Table 5.1.

	E_1	E_2	G_{12}	G_{13}	G_{23}	ν_{12}	X_T	X_C	Y_T	Y_C	S_L	G_{IC}	G_{IIC}	α_0	β
Value	171.42	9.08	5.29	5.29	3.98	0.32	2724	1690	64	199.8	92.3	0.2774	0.7879	53	2.98×10^{-8}
Unit	GPa	GPa	GPa	GPa	GPa	–	MPa	MPa	MPa	MPa	MPa	kJ/m^2	kJ/m^2	deg	MPa^{-3}
Source	[7]	[7]	[7]	[7]	[42]	[7]	[27]	[27]	[27]	[7]	[7]	[7, 11]	[7]	[7]	[7]

Table 5.1: Material properties for IM7/8552 used in the present study.

The nominal ply thickness specified by the manufacturer is equal to $0.131\,mm$ [27]. The laminate stacking sequence varies depending on the considered test case and will

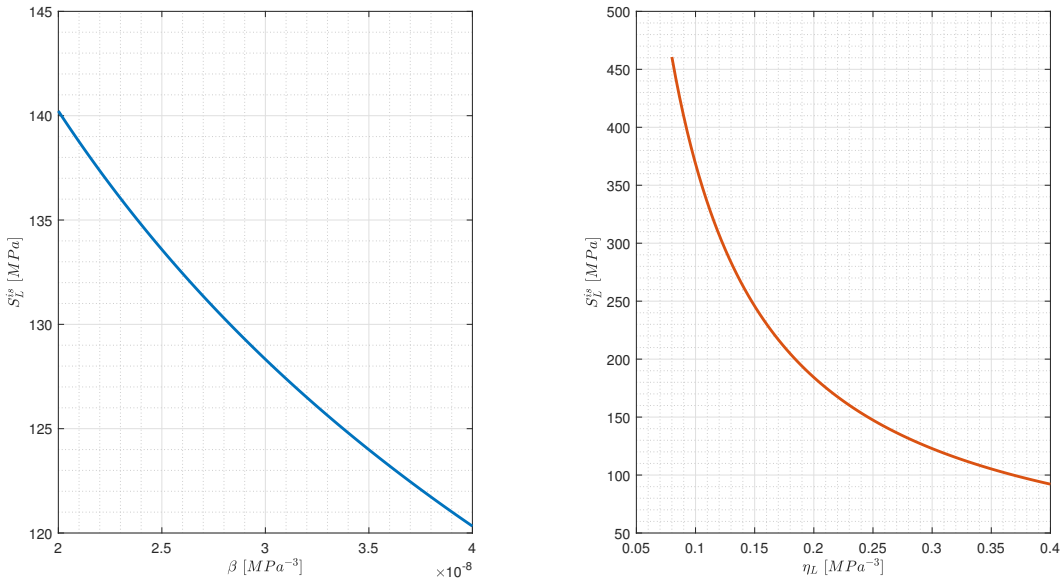
therefore be specified separately for each example.

Based on the material properties listed above, the in-situ strengths were evaluated using the formulations reported in Table 4.1. The results, reported in Table 5.2, were obtained using a dedicated MATLAB script and were subsequently used to verify the correctness of the API implementation. For η_L and η_T, Eqs. 3.9 and 3.7 provided the following values: $\eta_L = 0.352$ and $\eta_T = 0.287$.

	Y_T^{is}	S_L^{is}		S_T^{is}	
Configuration	Linear	Linear	Nonlinear	Linear	Nonlinear
UD	64	92.3		75.28	
Thick embedded	101.37	156.89	113.02	110.94	92.18
Thin embedded	156.89	284.64	128.52	284.64	104.82
Thin outer	110.94	201.27	105.57	284.64	86.10

Table 5.2: In-situ strengths (MPa) of IM7/8552 under linear and nonlinear shear behaviour

An initial verification of both the formulation and the selected material data can be obtained by observing that the predicted in-situ strengths are consistently higher than the corresponding UD values. Furthermore, as discussed in Section 4.5.2, the linear shear model predicts significantly higher strength values than the nonlinear formulation.



(a) Variation of S_L^{is} with β

(b) Variation of S_T^{is} with η_L

Figure 5.1: Effect of β and η_L on in-situ strengths

Figure 5.1 highlights the influence of β and η_L on the prediction of in-situ strengths.

As anticipated in Section 4.5.2, the parameter β has a relatively limited influence on the prediction of S_L^{is}. For CFRP materials, β typically ranges between 2×10^{-8} and 4×10^{-8} MPa^{-3} [8, 7, 15]. Within this interval, the variation of the predicted strength remains limited, with a maximum variation of approximately 14%.

As the value of β decreases, the material behaviour approaches a linear response, leading to higher predicted strength values. Therefore, when the value of β is not available, using higher values may represent a more conservative approach.

A significantly different behaviour is observed in the case of η_L. The prediction of in-situ strengths is highly sensitive to this parameter. In particular, increasing η_L leads to a substantial reduction in the predicted value of S_T^{is}.

In LaRC05 [48], a value of $\eta_L = 0.082$ is suggested for IM7-8551-7, a material system reasonably similar to the one considered in the present work. However, using this value causes the nonlinear prediction of S_T^{is} to exceed the corresponding linear prediction, contrary to the expected physical behaviour.

The value obtained through Eq. 3.9 leads instead to $\eta_L = 0.352$. Furthermore, in [33], a value of $\eta_L = 0.287$ was experimentally obtained for IM7/8552 system, which is reasonably close to the value predicted by Eq. 3.9. For this reason, Eq. 3.9 may represent a suitable approach to avoid requiring the user to manually define η_L. Nevertheless, the strong influence of this parameter on the final predictions must be carefully emphasized.

5.2 Overview of Validation Test Cases

Table 5.3 summarizes the validation campaign carried out to assess the predictive capabilities of the implemented failure criteria. For each configuration, the corresponding ASTM standard adopted as reference is also reported.

The validation campaign was designed to assess the predictive capabilities of the implemented failure criteria under different loading conditions and laminate configurations. Both unidirectional (UD) and multidirectional (MD) laminates were considered. Specimen geometries, loading procedures and the corresponding reference strength values were defined according to the requirements and recommendations provided by the corresponding ASTM standards.

The selected test matrix includes tensile, compressive, shear and open-hole configurations, covering a broad range of stress states commonly encountered in composite structures. In particular, longitudinal and transverse tests were used to assess the prediction of fibre and matrix failure under uniaxial loading, while off-axis compression, in-plane shear and short beam strength tests were included to evaluate the capability of the criteria to predict failure under combined and shear-dominated stress states. Open-hole tension and compression tests were additionally considered to investigate the predictive accuracy in the presence of stress concentrations.

Several layups were intentionally included for each loading condition in order to evaluate the robustness of the implementation and avoid conclusions based on isolated test cases.

For each configuration, the same procedure was adopted to estimate the FPF load. A

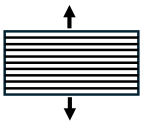
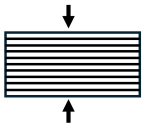
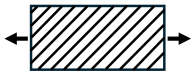
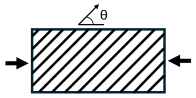
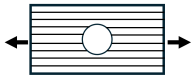
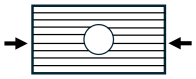
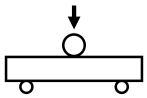
Test Type	**Configuration**	**Standard**	**Test ID**	**Layup**
Longitudinal Tension		ASTM D3039 [64]	LT-UD	$[0]_8$
			LT-MD-01	$[90/0]_{2s}$
			LT-MD-02	$[45/0/-45/90]_{2s}$
			LT-MD-03	$[45/-45/0/45/-45/90/45/-45/45/-45]_s$
Longitudinal Compression		ASTM D6641 [59]	LC-MD-01	$[90/0/90]_7$
			LC-MD-02	$[45/-45/0/45/-45/90/45/-45/45/-45]_s$
Transverse Tension		ASTM D3039 [64]	TT-UD	$[90]_{16}$
Transverse Compression		ASTM D6641 [59]	TC-UD	$[90]_{16}$
In-Plane Shear		ASTM D3518 [60]	PS-MD	$[45/-45]_{2s}$
Off-Axis Compression		ASTM D6641 [59]	OAC-UD-15	$[15]_{32}$
			OAC-UD-30	$[30]_{32}$
			OAC-UD-45	$[45]_{32}$
			OAC-UD-60	$[60]_{32}$
			OAC-UD-75	$[75]_{32}$
Open-Hole Tensile Strength		ASTM D5766 [62]	OHT-MD-01	$[90/0/\pm 45]_{3s}$
			OHT-MD-02	$[45/0/-45/90]_{2s}$
			OHT-MD-03	$[45/-45/0/45/-45/90/45/-45/45/-45]_s$
			OHT-MD-04	$[0/45/0/90/0/-45/0/45/0/-45]_s$
Open-Hole Compression Strength		ASTM D6484 [61]	OHC-MD-01	$[45/0/-45/90]_{2s}$
			OHC-MD-02	$[45/-45/0/45/-45/90/45/-45/45/-45]_s$
Short Beam Strength		ASTM D2344 [63]	SBS-UD	$[0]_{34}$
			SBS-MD-01	$[45/0/-45/90]_{3s}$

Table 5.3: Validation test matrix adopted for the assessment of the implemented failure criteria

linear static FEM analysis was first performed using the MSC Nastran SOL 101 solution sequence by applying a reference load P. The corresponding laminate minimum MOS was then evaluated with both failure criteria. Assuming linear scaling of stresses with

the applied load, the FPF load was estimated as $P_{FPF} = P \cdot (MOS + 1)$.

The corresponding strength value was then obtained by dividing the critical load by a characteristic section area. For all the investigated configurations, and in accordance with the corresponding ASTM standards, the characteristic section was defined as the product of the laminate thickness and the specimen width.

5.3 Summary of Validation Results

In Table 5.4 the comparison between the experimental reference values and the numerical predictions obtained using the Hoffman and LaRC05 failure criteria is reported.

Test ID	**Exp.** [MPa]	**Source**	**Hoffman** [MPa]	**Err.** [%]	**LaRC05** [MPa]	**Err.** [%]	**Failure Mode**
LT-UD	2724.00	[27]	2028.60	-25.52	2564.50	**-5.85**	fibre tensile
LT-MD-01	1359.40	[45]	629.01	-53.70	1014.10	**-25.40**	fibre tensile
LT-MD-02	717.10	[37]	346.37	-51.69	522.52	**-27.12**	matrix
LT-MD-03	462.50	[37]	190.50	-51.70	287.20	**-23.68**	matrix
LC-MD-01	1690.00	[27]	708.69	-58.06	1573.60	**-6.89**	fibre kinking
LC-MD-02	465.33	[37]	267.40	-42.53	436.56	**-6.18**	fibre kinking
TT-UD	64.00	[27]	61.64	**-3.68**	61.54	-3.83	matrix
TC-UD	199.80	[7]	191.51	-4.10	192.50	**-3.67**	matrix
PS-MD	92.30	[37]	57.02	-38.20	70.34	**-23.80**	matrix
OAC-UD-15	399.00	[33]	396.70	**-0.45**	351.40	-11.9	fibre kinking
OAC-UD-30	266.00	[33]	256.20	**-3.68**	246.20	-7.44	fibre kinking
OAC-UD-45	254.00	[33]	226.70	-10.73	244.51	**-3.73**	matrix
OAC-UD-60	263.00	[33]	141.80	-12.20	230.92	**-5.12**	matrix
OAC-UD-75	252.00	[33]	246.54	-2.17	253.82	**-0.72**	matrix
OHT-MD-01	438.70	[7]	197.20	-54.97	337.15	**-23.02**	fibre kinking
OHT-MD-02	443.00	[31]	197.07	-55.51	315.68	**-28.74**	matrix
OHT-MD-03	300.90	[31]	131.04	-56.46	196.25	**-34.79**	fibre kinking
OHT-MD-04	597.30	[31]	294.20	-50.74	584.60	**-2.12**	matrix
OHC-MD-01	377.00	[31]	235.24	-29.14	263.07	**-20.76**	fibre kinking
OHC-MD-02	264.00	[37]	146.31	-44.73	201.97	**-23.71**	fibre kinking
SBS-UD	118.10	[37]	225.70	+91.10	83.70	-29.13	matrix
SBS-MD-01	83.00	[37]	55.11	-34.10	80.92	**-3.24**	matrix
MRE [%]				−32.57		−14.58	
SD [%]				21.71		11.21	
Max. Abs. Err. [%]				91.10		34.79	
Min. Abs. Err. [%]				0.45		0.75	

Table 5.4: Comparison between experimental results and numerical predictions obtained with Hoffman and LaRC05 criteria.

It should be emphasized that the experimentally measured ultimate strengths should primarily be regarded as benchmark reference values for the validation of the implemented methodologies. Considering the use of linear static analyses without progressive damage modelling and the adoption of 2D laminate elements for the numerical models, exact agreement with the experimental ultimate loads was not expected.

The results show that both criteria systematically provide conservative predictions, with the exception of the SBS-UD test for Hoffman criterion, with respect to the experimental values. However, significant differences can be observed in terms of predictive capability and robustness.

Overall, the LaRC05 criterion demonstrated substantially better agreement with the experimental data. The mean relative error decreased from -32% for the Hoffman criterion to -15% for LaRC05, while also showing a lower standard deviation. This indicates not only an improvement in the average prediction accuracy, but also a more consistent behaviour across the different laminate configurations and loading conditions considered.

The improvement provided by LaRC05 compared to the Hoffman criterion becomes particularly evident in multidirectional laminates and in configurations characterized by combined stress states, matrix-dominated failure mechanisms and stress concentrations.

In general, the results suggest that the prediction error tends to increase with the complexity of the laminate stacking sequence. This behaviour is expected, since the numerical predictions are based on a first-ply failure approach, whereas the experimental ultimate strength is also influenced by damage progression and stress redistribution occurring after the onset of the FPF.

The best agreement with the experimental data was obtained for brittle unidirectional configurations, such as longitudinal tension, transverse loading tests and off-axis compression tests where first-ply failure and ultimate failure occur almost simultaneously. In these cases, the LaRC05 predictions showed very small discrepancies with respect to the experimental reference values.

In the following subsections, a more detailed discussion of the different test configurations is presented together with selected output vectors generated by the developed API.

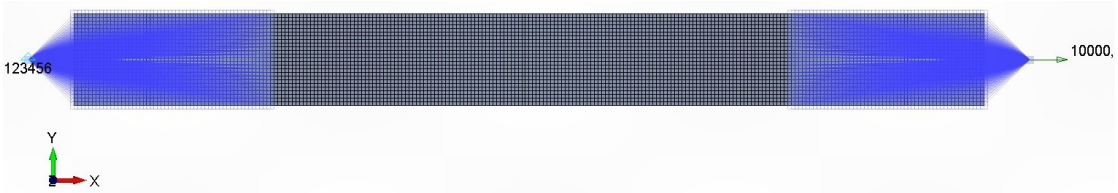
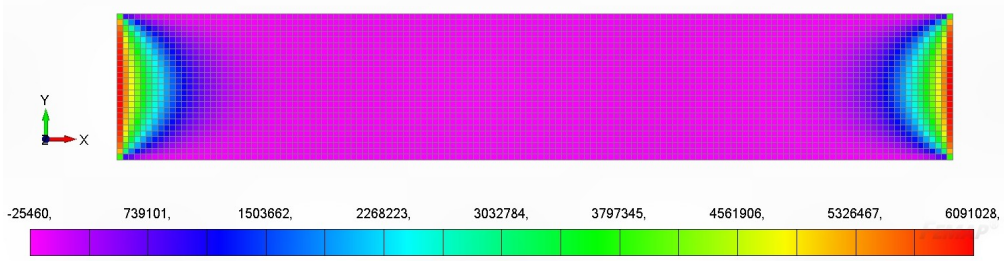


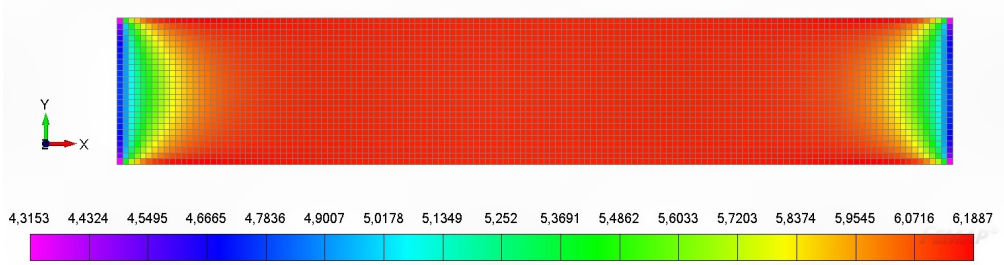
Figure 5.2: FEM model adopted for the longitudinal tension tests, including boundary conditions and loading application

5.3.1 Longitudinal Tension and In-Plane Shear Tests

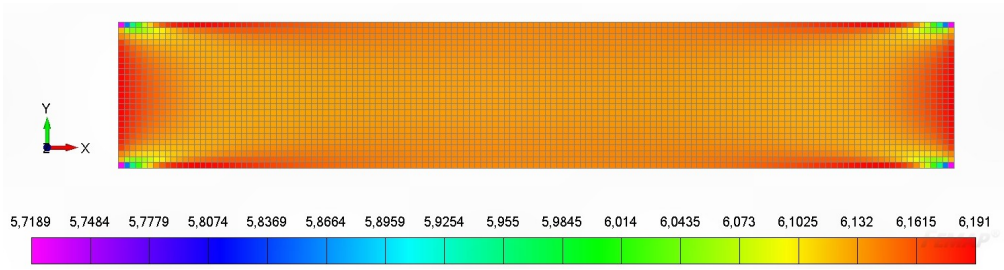
The longitudinal tension specimen were modelled according to the ASTM D3039 standard: it has a length of 250 mm and a width of 25 mm. The applied load, of 10000 N for all longitudinal tension test, was introduced through RBE2 elements in order to distribute the load uniformly across the specimen width and reproduce the clamping regions adopted in the experimental setup (see Figure 5.2).



(a) σ_2



(b) Hoffman MOS



(c) LaRC05 MOS for fibre tensile failure

Figure 5.3: Stress and MOS distributions predicted for the LT-UD test

In all the uniaxial tensile tests, the out-of-plane shear stress components τ_{23} and τ_{31} were null. Depending on the laminate layup, the dominant failure mechanism predicted by the LaRC05 criterion was associated with fibre tensile failure or matrix failure.

Some initial considerations can be drawn from the unidirectional longitudinal tension case LT-UD, which represents the simplest investigated configuration while still highlighting important conceptual differences between the two failure criteria. In this case, the difference between the Hoffman and LaRC05 predictions cannot be attributed to

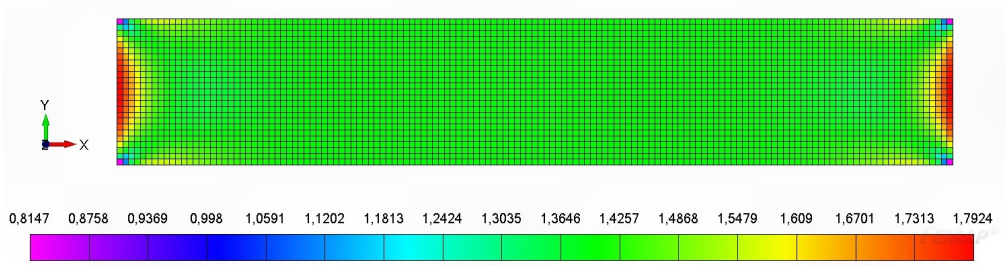
in-situ strength effects, since for unidirectional laminates the isolated material strengths are considered in LaRC05.

Figures 5.3b and 5.3c show the MOS distributions predicted respectively by the Hoffman criterion and by the LaRC05 fibre tensile formulation for a representative ply. Since the laminate is unidirectional, the obtained distributions are identical for all plies. As expected, the dominant failure mechanism predicted by LaRC05 corresponds to fibre tensile failure. In particular, the minimum MOS associated with matrix failure was equal to 7.33, whereas the minimum MOS predicted for fibre tensile failure was equal to 5.72.

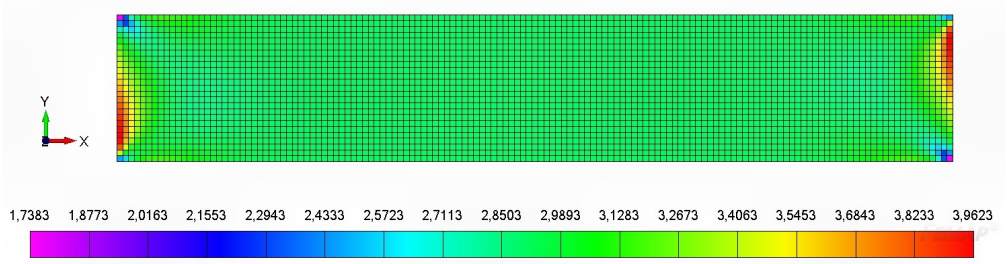
An interesting observation can be drawn from the central region of the specimen. In this area, where σ_2 and τ_{12} are negligible if compared to σ_1, both criteria predict nearly identical MOS values. This suggests that the larger discrepancy observed for the Hoffman criterion mainly originates from the localized transverse stresses generated near the clamping regions.

In these regions, σ_2 becomes non-negligible with respect to σ_1, despite remaining approximately one order of magnitude lower. In the Hoffman criterion, this contribution directly compare in the interaction equation, significantly reducing the local MOS values. Conversely, in LaRC05 the contribution of σ_2 does not affect the fibre tensile failure MOS and the distribution remains substantially uniform along the specimen.

Overall, this relatively simple test case already highlights one of the main strengths of the LaRC05 formulation. The separation of the stress components into distinct failure mechanisms lead to predictions that are generally more consistent with the physical behaviour of the laminate.



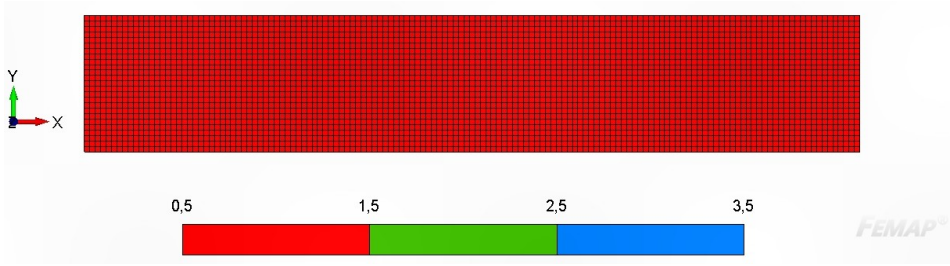
(a) Hoffman minimum MOS value among all plies



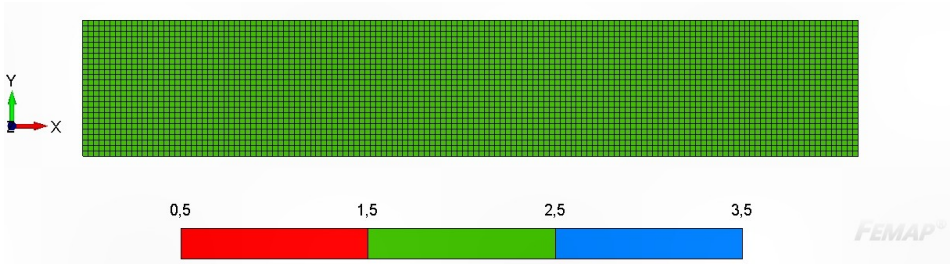
(b) LaRC05 minimum MOS value among all plies considering all failure modes

Figure 5.4: MOS distributions predicted for the LT-MD-02 test

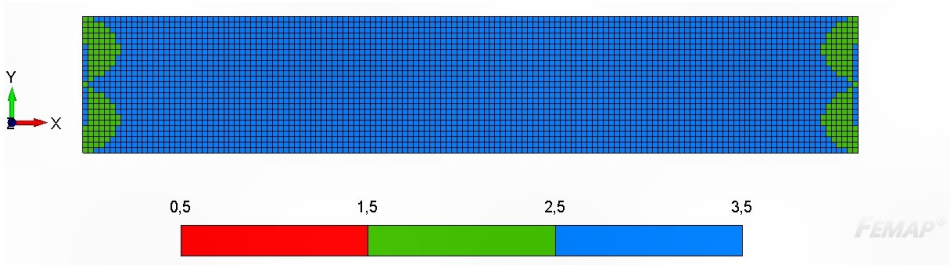
For the multidirectional case, the LT-MD-02 configuration is proposed as a representative example. The corresponding MOS distributions predicted by the Hoffman and LaRC05 criteria are shown in Figure 5.4. In multidirectional laminates, the discrepancy between first-ply failure and ultimate failure becomes more pronounced compared to unidirectional laminates, since damage can progressively develop before final collapse. In addition to the considerations already discussed for the UD case, in MD laminates the differences between the Hoffman and LaRC05 predictions are also influenced by the in-situ effect.



(a) Dominant failure mode for the 0° plies



(b) Dominant failure mode for the $+45°/-45°$ plies



(c) Dominant failure mode for the 90° plies

Figure 5.5: Dominant LaRC05 failure modes predicted for plies with different fibre orientations in the LT-MD-02 test (red = fibre tensile failure; green = matrix failure; blue = fibre kinking failure)

As expected, the most critical plies predicted by LaRC05 are the outer plies oriented at 45°, where the in-situ effect is less pronounce. Consequently, the minimum MOS distribution among all plies corresponds to the distribution associated with the ±45°

plies shown in Figure 5.5b.

Interesting considerations can also be drawn from the dominant failure modes predicted for plies with different fibre orientations, reported in Figure 5.5. According to the convention adopted within the developed API, the failure mode indices correspond to: `1` = fibre tensile failure, `2` = matrix failure, and `3` = fibre kinking failure.

Before discussing the results, it is important to note that, according to Classical Lamination Theory (CLT), the stresses acting within a ply do not depend solely on its material properties and fibre orientation. They also depend on the strain of the overall laminate and, therefore, on the layup and loading conditions. As a consequence, even under the same test configuration and applied load, the dominant failure mode associated with a given ply orientation cannot be considered independent of the plies stacking sequence. Therefore, the failure modes reported in Figure 5.5 should be regarded as specific to the LT-MD-02 test case.

For the 0° plies, shown in Figure 5.5a, the dominant failure mode is fibre tensile failure. This result is consistent with the applied loading condition, since the laminate is subjected to longitudinal tension and the fibres are aligned with the loading direction.

A different behaviour is observed for the ±45° plies, shown in Figure 5.5b, where matrix failure becomes the governing failure mode. The local stress state obtained from the Nastran results and confirmed through CLT consists of a combination of longitudinal, transverse and shear stresses. In particular, for the applied load P considered, the longitudinal stress component σ_1 reaches values of the order of hundreds of MPa, whereas σ_2 and τ_{12} remain of the order of tens of MPa. Nevertheless, the fibre tensile failure formulation of LaRC05 compares σ_1 with the longitudinal tensile strength $X_T = 2724, \text{MPa}$, while the matrix failure formulation is governed by the combined action of σ_2 and τ_{12} relative to the corresponding in-situ strengths, which are typically one order of magnitude lower than X_T (see Table 5.1).

Consequently, although σ_1 is the largest stress component, it remains far from the fibre tensile strength, whereas the transverse and shear stress contributions reach a significantly larger fraction of the corresponding matrix strengths.

For the 90° plies, the dominant failure mechanism may correspond either to matrix failure or fibre kinking failure depending on the laminate configuration. This behaviour is mainly associated with the transverse strain of the laminate induced by the Poisson effect. As a first approximation, the stress component acting along the fibre direction of a 90° ply may be expressed as

$$\sigma_1 \approx E_1 \varepsilon_y$$

where ε_y denotes the transverse strain of the laminate. Since the longitudinal modulus E_1 is significantly larger than the transverse modulus E_2, even relatively small transverse strains may generate substantial longitudinal stresses within the 90° plies.

For the LT-MD-02 laminate, the transverse contraction of the laminate generates compressive σ_1 values within the 90° plies that are approximately one order of magnitude larger than σ_2. Although this result may initially appear counterintuitive, it is fully consistent with laminate compatibility conditions and with the transformation of stresses

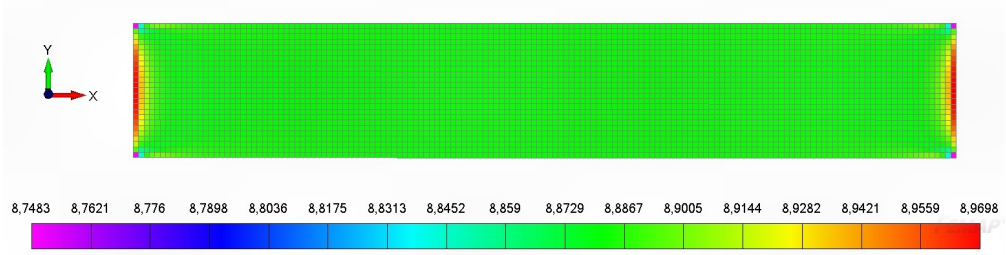
between the global and material reference systems. Consequently, depending on the relative magnitude of the compressive stress σ_1 and the transverse stress σ_2, the dominant failure mode predicted by LaRC05 could be matrix failure or fibre kinking failure.

An additional observation can be drawn from the experimental results reported in Table 5.4. The longitudinal tensile strength decreases from $1359.4\,\mathrm{MPa}$ for LT-MD-01 to $717.1\,\mathrm{MPa}$ for LT-MD-02 and $462.5\,\mathrm{MPa}$ for LT-MD-03, despite the progressive increase in the number of plies from 8 to 16 and 20, respectively.

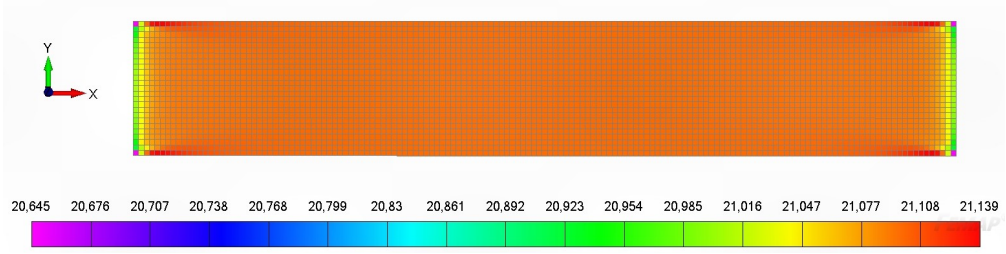
This behaviour highlights the strong influence of the stacking sequence and ply orientation distribution. In particular, the tensile strength tends to decrease as the percentage of plies aligned with the loading direction is reduced, since a larger fraction of the load must be carried by off-axis plies, promoting matrix-dominated failure mechanisms.

The in-plane shear test (PS-MD) defined by ASTM D3518 can be interpreted as a particular case of longitudinal tension. For the layup $[\pm 45°]_{ns}$ prescribed by the standard, CLT predicts that the applied longitudinal stress is transformed into a local stress state dominated by shear, leading to the relationship $\tau_{12} = \sigma_x/2$. Consistently, the maximum in-plane shear stress is evaluated as $\tau_{12} = P/(2A)$, where P is the longitudinal applied load and A is the specimen cross section area.

5.3.2 Longitudinal Compression Tests



(a) Hoffman minimum MOS value among all plies



(b) LaRC05 minimum MOS value among all plies

Figure 5.6: MOS distributions predicted for the LC-MD-01 test

The FEM model adopted for the longitudinal compression tests is analogous to that previously described for the longitudinal tension configuration (Figure 5.2). A compressive load of $5000\,N$ was applied to the specimen.

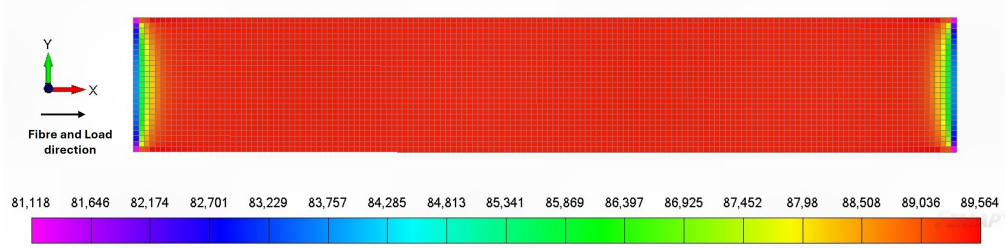
Among all the considered validation cases, longitudinal compression is one of the configurations for which the largest difference between the Hoffman and LaRC05 predictions is observed. As an example, Figure 5.6 reports the MOS distributions obtained for the LC-MD-01 test with a cross-ply laminate.

The minimum MOS predicted by Hoffman is associated with the 0° plies ($MOS \simeq 8.75$), whereas the minimum MOS predicted by LaRC05 is associated with the outer 90° plies ($MOS \simeq 20.65$). For these plies, the dominant predicted failure mode is fibre kinking.

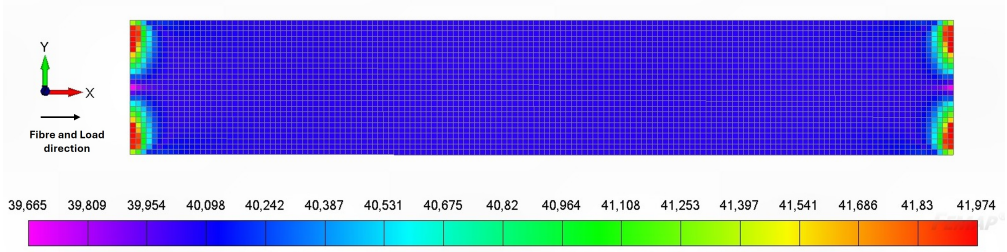
Particular attention should therefore be paid to the 0° plies, since they exhibit the largest discrepancy between the two criteria. In fact, for these plies, Hoffman predicts a minimum MOS of approximately 8.75, whereas the minimum MOS predicted by LaRC05 is approximately 39.66. The corresponding MOS distributions are reported in Figure 5.7.

The stress state within the 0° plies is dominated by the longitudinal compressive stress component $\sigma_1 < 0$, while both σ_2 and τ_{12} remain comparatively smaller. Furthermore, the transverse stress component is also compressive ($\sigma_2 < 0$). Under these conditions, matrix failure is not expected to be critical, since transverse compression increases the resistance against matrix cracking. Consistently, the fibre kinking mode provides substantially lower MOS values than the matrix failure mode.

It is also worth noting that X_C does not explicitly appear in the LaRC05 fibre kinking formulation. Therefore, the significantly improved agreement with the experimental results provides additional confidence in the correct implementation of the kinking model.



(a) Matrix failure



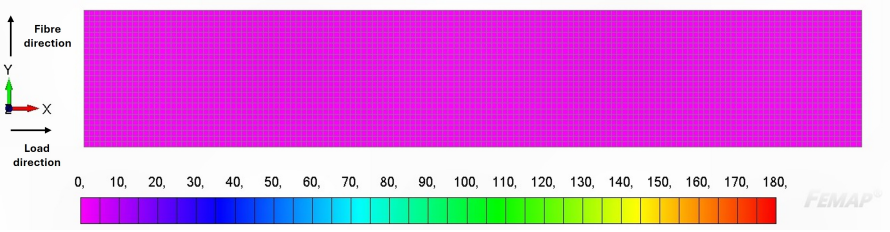
(b) Fibre kinking failure

Figure 5.7: LaRC05 MOS distributions for the 0° plies in test LC-MD-01

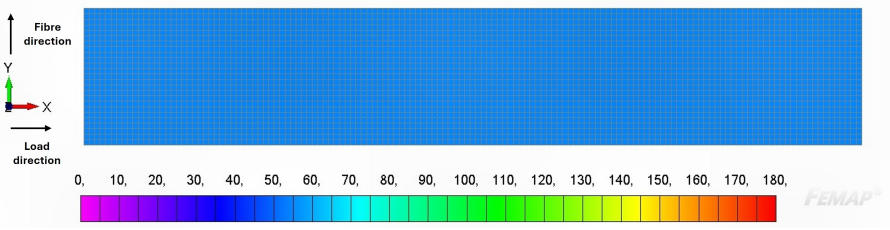
5.3.3 Transverse Loading Tests

The transverse tension and compression tests were used to verify the implementation of the matrix failure formulation. Since both specimens consist of unidirectional laminates subjected to a nearly uniaxial stress state ($\sigma_2 \gg \sigma_1, \tau_{12}$), the failure response is dominated by matrix failure and no significant stress redistribution effects are expected. Furthermore, the failure process is inherently brittle, such that first-ply failure and ultimate failure occur almost simultaneously. As a result, both Hoffman and LaRC05 provide accurate predictions of the experimental failure loads.

In particular, the good agreement obtained with LaRC05 confirms the correct implementation of the matrix failure criteria, including the determination of the critical fracture plane angle α. This aspect is highlighted in Figure 5.8, where the fracture angle associated with the minimum MOS distribution for both the tests is shown.



(a) Transverse tension test (TT-UD)



(b) Transverse compression test (TC-UD)

Figure 5.8: Fracture angle α corresponding to the minimum MOS for matrix failure

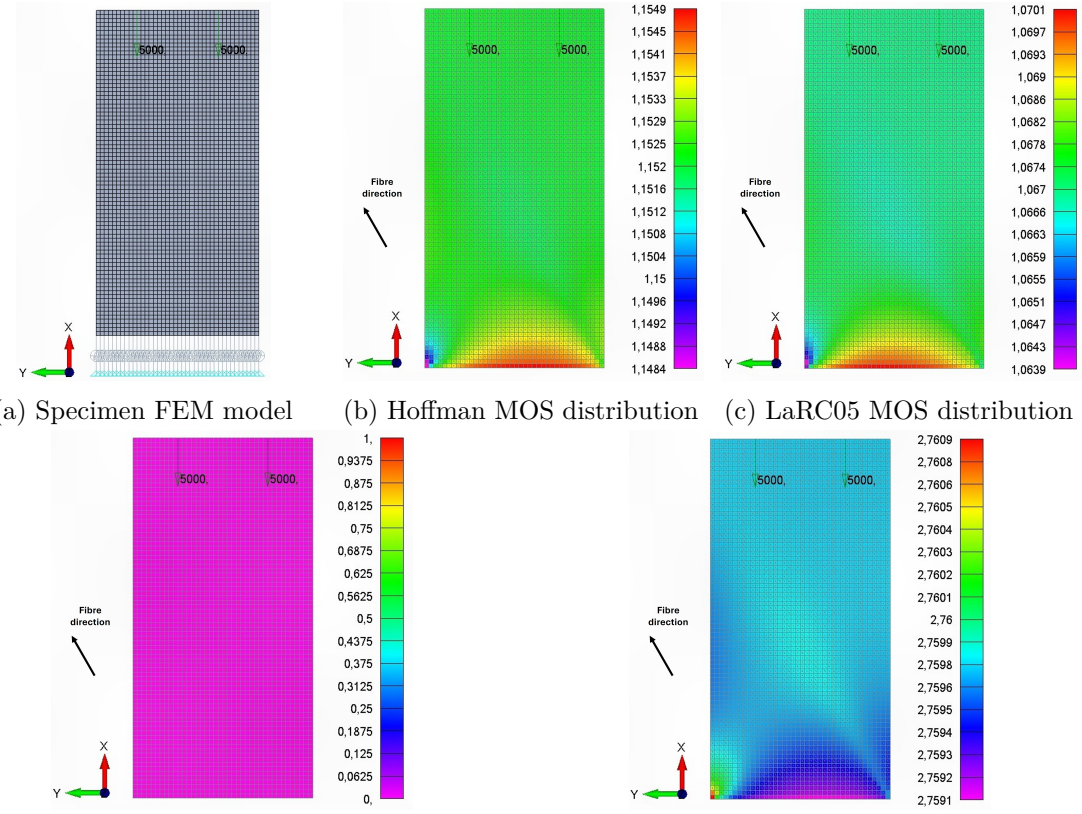
For transverse tension, the predicted fracture angle is close to 0°, indicating that failure occur on a plane parallel to the fibres and normal to the applied load. In contrast, for transverse compression, the critical fracture plane angle α_0 is approximately 55°. These predictions are consistent with the fracture planes observed experimentally (see α_0 value in Table 5.1).

5.3.4 Off-Axis Compression Tests

Off-axis specimens are commonly used to generate shear stresses and deformations in fibre-reinforced composites through the application of simple axial loads. The main advantage of this configuration is that a combined stress state with respect to the material

principal directions can be produced using a uniaxial loading condition. By employing off-axis block specimens in compression, fibre kinking and matrix cracking can be induced at significantly lower compressive stress levels due to the presence of in-plane shear stresses [4].

The specimens considered in this work are based on those adopted by Koerber et al. in [33], which were used as a reference for the validation of the static results. They have nominal dimensions of $20 \times 10 \times 4$ mm^3 and consist of 32 plies with identical fibre orientation, resulting in a unidirectional squat laminate.



(a) Specimen FEM model (b) Hoffman MOS distribution (c) LaRC05 MOS distribution

(d) Kink-band angle ψ corresponding to the minimum MOS

(e) Misalignment angle ϕ associated with the value of ψ minimizing the MOS

Figure 5.9: OAC-30 test specimen and results

The finite element model was developed using 2D laminate elements, as shown in Figure 5.9a. A uniformly distributed compressive load was applied to one edge of the specimen, whereas the opposite edge was connected to spring elements having infinite stiffness in all degrees of freedom except the transverse translations.

This modelling strategy was adopted to reproduce the lubricated end-loaded boundary conditions employed in the experimental campaign of Koerber et al. [33], in order to avoid the introduction of artificial transverse constraints that could affect the stress

distribution.

As the off-axis angle θ increases, the applied axial load is progressively redistributed from the fibre direction towards the transverse direction. Consequently, the contribution of σ_1 and τ_{12} decreases, while σ_2 becomes increasingly significant. This evolution results in a transition of the dominant failure mode from fibre kinking to matrix cracking, as observed both experimentally by Koerber et al. [33] and numerically in the present work (see Table 5.4).

The results obtained for the OAC-30 configuration, in which the fibres are oriented at 30° with respect to the loading direction, are reported in Figure 5.9. Given the importance of fibre kinking in this test, the two additional output vectors generated by the API for this failure mode for each ply are also shown: the kink-band angle ψ corresponding to the minimum MOS (Figure 5.9d) and the associated misalignment angle ϕ (Figure 5.9e). Since the laminate is unidirectional, the distributions of MOS, ψ, and ϕ are identical through the thickness and therefore coincide for all plies. The predicted kink-band angle is equal to zero throughout the specimen, indicating that the fibres involved in the failure mode remain within the laminate plane.

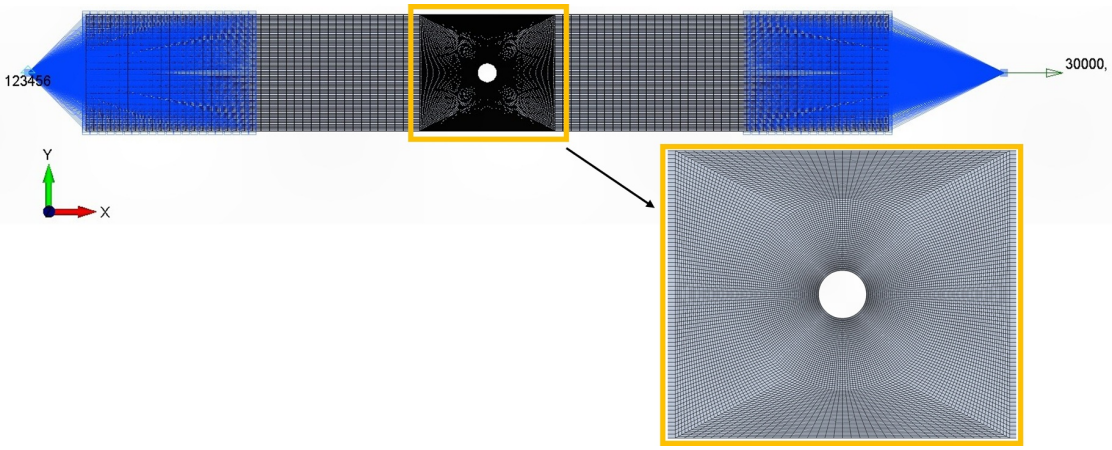


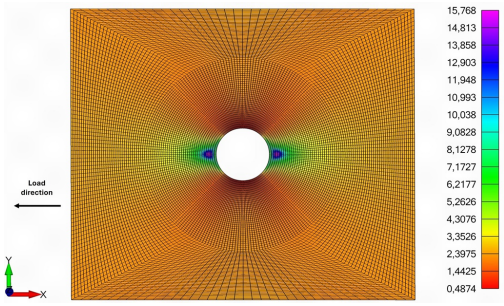
Figure 5.10: FEM model adopted for open hole tests, including boundary conditions and loading application

5.3.5 Open-Hole Strength Tests

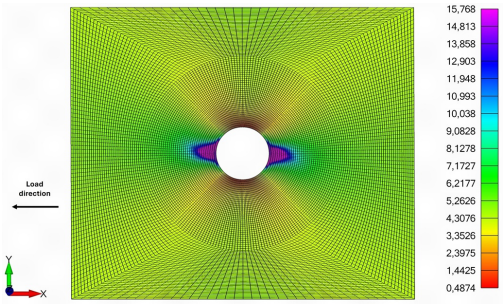
CFRPs have excellent characteristics in terms of specific strength and high rigidity, but they also lose a substantial amount of their strength when a cut-out is made. In order to assess the use of composite materials, particular in aeronautic applications, tests must be performed with samples that have a circular hole cut through the centre. ASTM D5766 [62] and ASTM D6484 [61] are the standard followed respectively for evaluate the Open-Hole Tensile (OHT) strength and the Open-Hole Compression (OHC) strength. The test consist in uniaxial tension or compression of a multidirectional laminate with a 6 mm diameter circular hole cut in its centre.

The finite element model adopted in the present work is shown in Figure 5.10. The specimen dimensions were defined according to the corresponding ASTM standards. Following the mesh convergence study proposed by Su and Colton in [67] for open-hole compression specimens, a refined mesh with 220 elements along the hole perimeter and a characteristic element length of 0.25 mm was adopted for both OHT and OHC analyses.

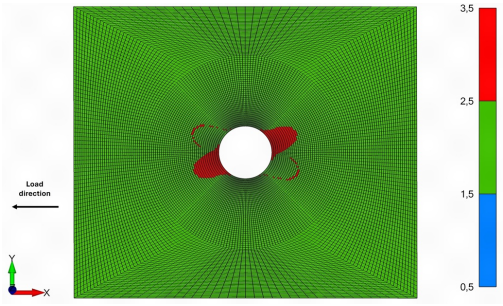
The quadratic failure criteria as the Hoffman criterion, as evident even from Table 5.4, are inapplicable when failure is initiated by localized disturbances such as holes. If any of these criteria were evaluated using the stresses near the disturbance, the criteria would underestimate the failure load [34].



(a) Hoffman MOS distribution



(b) LaRC05 MOS distribution



(c) LaRC05 failure mode distribution

Figure 5.11: OHT-MD-02 test results

Unlike the other validation cases considered in this work, the stress and MOS distributions around the hole are characterized by highly localized stress concentrations and complex interactions among different failure mechanisms. A rigorous interpretation of these phenomena would require a dedicated investigation and therefore lies beyond the scope of the present work.

The primary purpose of the open-hole tests was not to provide a detailed description of the local stress redistribution around the holes, but rather to assess the capability of the implemented LaRC05 criterion to predict the onset of failure in notched laminates. In this regard, the results reported in Table 5.4 demonstrate that LaRC05 provides significantly more accurate predictions than the Hoffman criterion for both OHT and OHC specimens. As an example, Figure 5.11 shows the results obtained for specimen OHT-MD-02.

5.3.6 Short Beam Strength Tests

The short-beam strength test is a flexure test thought to only estimate interlaminar shear strength. The specimen consist in a short squat beam up to 6.00 mm thick, with a length 6 time the thickness and a width of 2 times the thickness [63]. The beam is loaded in three-point bending. Considering the SBS-UD test, the total thickness of the laminate is 4.45 mm and the dimension of the specimen has been modelled accordingly.

There are difficulties associated with this type of test, and its overall value is questionable. The specimen is designed so that shear deformation effects are as large as possible, and failure results from interlaminar shear stresses rather than normal stresses [58].

However, although shear is the dominant applied loading in this test method, the internal stresses are complex, and a variety of failure modes can occur [63]. The specimen has a parabolic shear stress distribution through the thickness, and the maximum shear stress may not be at the mid-surface of the beam. The interlaminar shear strength is expressed as

$$F^{sbs} = 0.75 \cdot \frac{P_m}{b \cdot h}$$

where F^{sbs} is the short beam strength, P is the applied load, and b and h are the beam width and thickness, respectively.

Although the test specimen does not satisfy the assumptions of the 2D model and the accuracy of the off-plane shear stresses derived from the CLT is low, the test is nevertheless proposed as it is one of the few bending tests for which experimental results are available. Furthermore, for laminated 2D elements, Nastran does not return the out-of-plane stress σ_3, which is significant at the supports and the load cylinder.

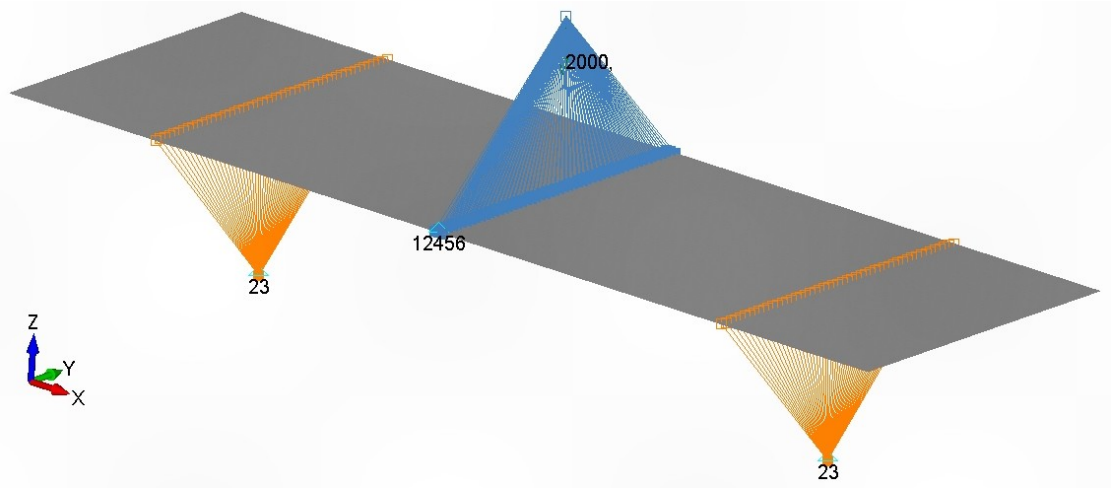
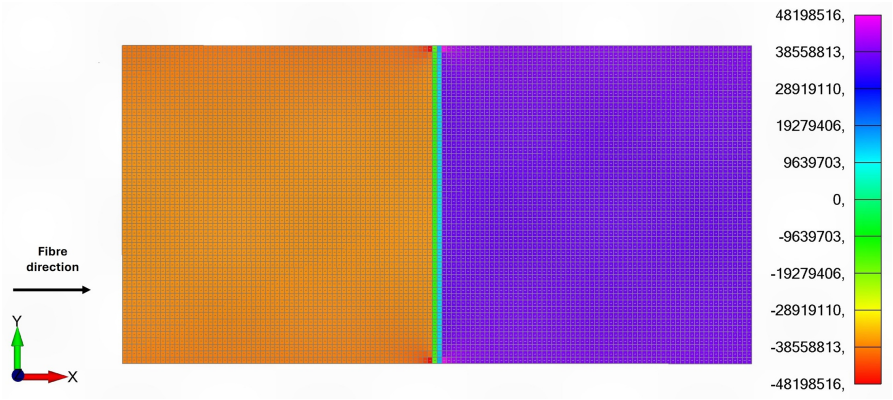
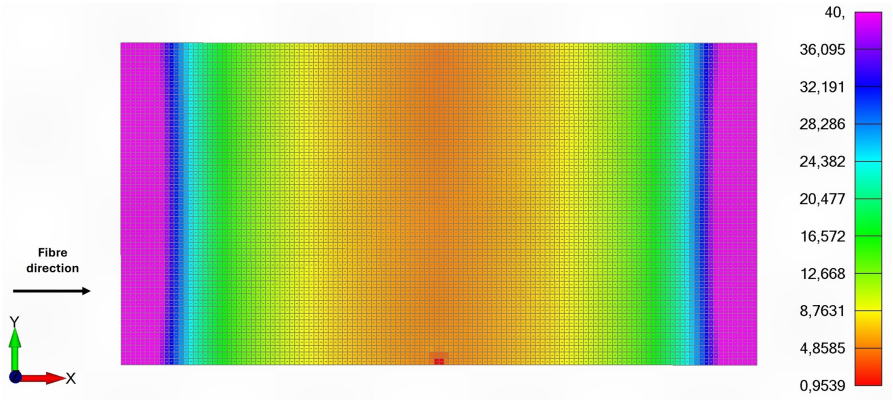


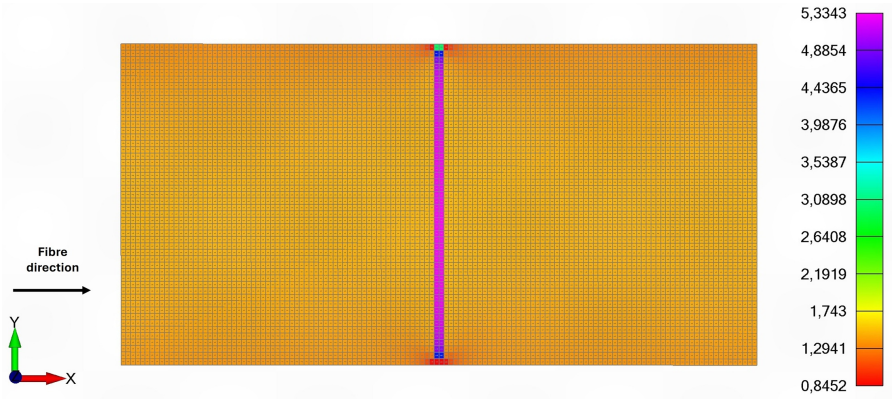
Figure 5.12: FEM model adopted for the short beam strength tests, including boundary conditions and loading application



(a) Out-of-plane shear stress $tau_x z$ distribution in the intermediate laminate ply



(b) Hoffman minimum MOS value among all plies



(c) LaRC05 minimum MOS value among all plies

Figure 5.13: Stress and MOS distributions predicted for the SBS-UD test

Figure 5.12 shows the finite element model adopted for the analysis. The supports were modelled with RBE2 elements positioned according to ASTM D2344, whereas the

loading nose was represented by an RBE3 element. To reproduce the contact area associated with the 6 mm diameter loading nose, all nodes located within 0.1 mm from the specimen midline were included as dependent nodes. To eliminate rigid-body motions, the rotations of the outer node located on the specimen midline were constrained (see Figure 5.12). Since these constraints introduce non-physical stress concentrations, the elements immediately adjacent to the constrained node were excluded from the evaluation of the minimum MOS.

The comparison between the two failure criteria (Figure 5.13) clearly illustrates the limitations of the Hoffman criterion for this type of problem. Being a 2D criterion, Hoffman neglects out-of-plane stresses and therefore completely ignores the contribution of τ_{xz}. As a consequence, it predicts significantly higher MOS values and consequently an ultimate strength considerably larger than the experimentally measured one (+91.10%).

Conversely, LaRC05 explicitly accounts for out-of-plane shear stresses through the matrix failure and fibre kinking formulations. As expected, the most critical ply predicted by LaRC05 is the central ply of the laminate (ply 17), where τ_{xz} reaches its maximum value (Figure 5.13a). In contrast, Hoffman identifies the outer ply in contact with the loading nose as the critical one, since the maximum longitudinal stresses σ_1 occur in this region.

Chapter 6

Application to a real satellite use case

6.1 Overview of the Case Study

Following the validation of the two composite laminate failure criteria and the verification of the MOS calculations for both honeycomb cores and metallic face sheets, the developed API was applied to the analysis of three panels belonging to an actual satellite manufactured by Thales Alenia Space.

Due to industrial confidentiality constraints, the name of the satellite, as well as detailed information regarding the materials and laminate layups, cannot be disclosed. Nevertheless, it can be stated that the satellite is a telecommunications platform with a launch mass of approximately 2.5 tonnes and that all composite skins are multidirectional.

The objective of this case study is to demonstrate the applicability of the developed API to a representative industrial finite element model and to assess its effectiveness in automating the evaluation, processing, and organization of structural analysis results. The selected panels involve all the modelling approaches supported by the API and therefore provide a comprehensive validation of the implemented workflow.

The three selected panels are shown in Figure 6.1, identified according to their position within the global reference system shown. The element groups associated with different properties are highlighted using different colours and are listed in Table 6.1.

Two of them are lateral panels belonging to the secondary structure, while the third one is the bottom panel and belongs to the primary structure. These panels were selected because they are representative of the three main sandwich panel configurations adopted within the satellite and, collectively, involve all the modelling approaches supported by the developed API.

The $-X$ panel features composite laminate face sheets and is modelled using 2D laminate elements. The $-Y$ panel, which also employs 2D laminate elements, supports the solar arrays and the majority of the onboard equipments. Both for mechanical and thermal requirements, its skins are made of aluminium alloy.

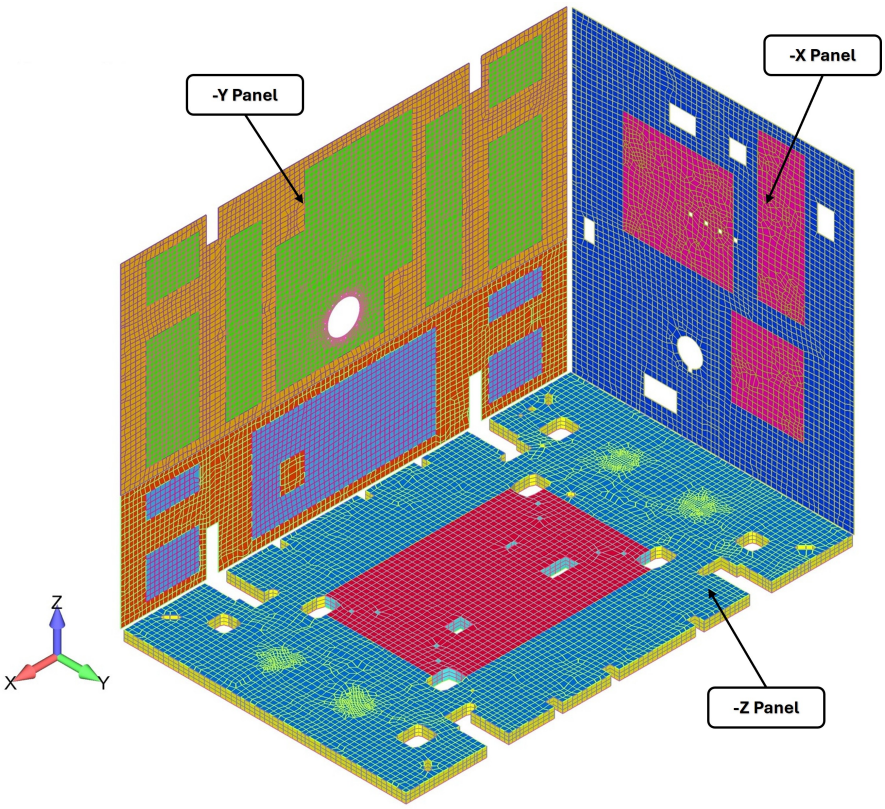


Figure 6.1: Analysed satellite panels

ID	Group	Colour
1	-Y panel - upper part - unreinforced area	green
2	-Y panel - upper part - reinforced area	orange
3	-Y panel - lower part - unreinforced area	purple
4	-Y panel - upper part - reinforced area	red
5	-X panel - unreinforced area	blue
6	-X panel - reinforced area	fuchsia
7	-Z panel - honeycomb core - reinforced area	yellow
8	-Z panel - honeycomb core - unreinforced area	cyan
9	-Z panel - bottom skin - reinforced area	*not visible*
10	-Z panel - bottom skin - unreinforced area	*not visible*
11	-Z panel - top skin - reinforced area	light blue
12	-Z panel - top skin - unreinforced area	magenta

Table 6.1: Group identification

Moreover, as can be seen in the Figure 6.1, the panel is manufactured as two separate sub-panels to facilitate assembly and integration activities. The two sections are connected through structural bars and square cleats located along the interface.

The bottom panel ($-Z$) also features composite skins; however, the honeycomb core is modelled using solid elements, while the face sheets are modelled using 2D laminate elements and are divided into independent structural groups. All three panels incorporate a honeycomb core.

As shown in Figure 6.1, different coloured regions can be identified within each panel. These regions correspond to local reinforcements, commonly referred to as doublers. In these areas, the face-sheet thickness is increased in order to enhance the local strength of the structure. For metallic face sheets, this is achieved by increasing the sheet thickness, whereas for composite face sheets the reinforcement is obtained by adding additional plies to the laminate stacking sequence. Furthermore, a honeycomb core with a larger foil thickness is generally adopted in reinforced regions. The core height is adjusted accordingly so that the overall panel thickness remains constant throughout the structure.

These reinforcements are typically introduced at panel interfaces or in correspondence with attachment points for propellant tanks and other onboard equipment. In the specific configurations considered in this work, the reinforced regions are located on the external area of the $-Y$ and $-Z$ panels, whereas for the $-X$ panel the reinforcement is located on the internal area.

In this case study, a total of 20 load cases, listed in Table 6.2, were analysed. These load cases are defined in terms of body accelerations and correspond to the quasi-static loads specified by the launcher for structural verification.

Load Case ID	**X Acceleration** [g]	**Y Acceleration** [g]	**Z Acceleration** [g]
1	2	0	-3.6
2	-2	0	-3.6
3	0	2	-3.6
4	0	-2	-3.6
5	1	0	-6
6	-1	0	-6
7	0	1	-6
8	0	-1	-6
9	0.9	0	2.2
10	-0.9	0	2.2
11	0	0.9	2.2
12	0	-0.9	2.2
13	0.5	0	-4.5
14	-0.5	0	-4.5
15	0	0.5	-4.5
16	0	-0.5	-4.5
17	2	0	1.5
18	-2	0	1.5
19	0	2	1.5
20	0	-2	1.5

Table 6.2: Definition of the analysed load cases

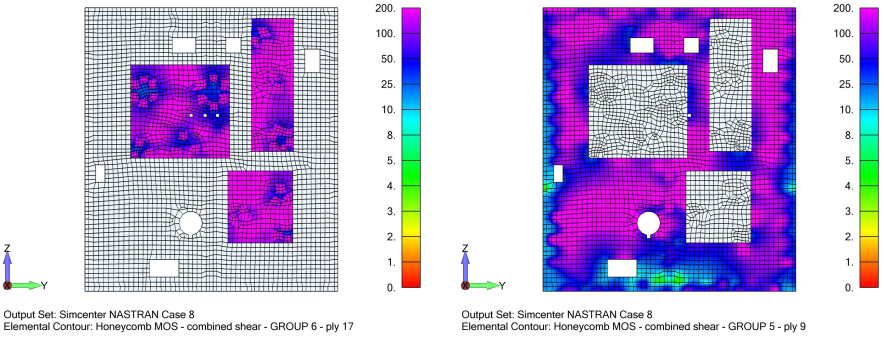
The main advantage of the developed API lies in its ability to automatically process Nastran results and generate, within a few minutes, the tables, plots, and MOS evaluations required for the structural assessment of the analysed panels. Furthermore, as anticipated in the previous chapters, multiple structural groups can be processed simultaneously, which is particularly advantageous when they share the same material properties.

The material data required for the application of the LaRC05 criterion, particularly the fracture toughness values, were obtained from the literature. The safety factors adopted in the analysis were defined in accordance with the requirements of ECSS-E-ST-32-10C [17], using the values prescribed for satellite structures subjected to global flight loads.

The results obtained for the $-X$, $-Y$, and $-Z$ panels are presented in Sections 6.2, 6.3, and 6.4, respectively. Only a representative subset of the tables and summary plots automatically generated by the API is presented in the following sections. In particular, the reported tables identify, for each group and failure mode, the most critical load case together with the minimum MOS and associated data. Given the large amount of information produced by the analyses, the complete set of results for every load case is not included and would not be practical to present within the scope of this work.

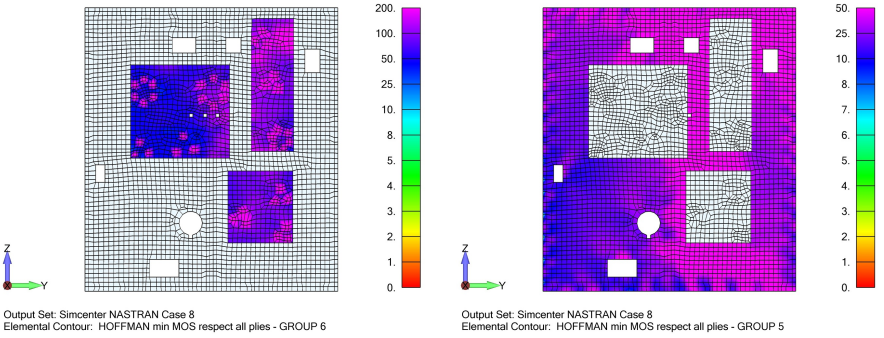
For the panels with composite skins, the MOS were evaluated using both the Hoffman and LaRC05 failure criteria. A comparison between the results obtained with the two criteria is presented and discussed in section 6.5. Unlike the panel summaries presented in the following sections, this comparison is based on the complete set of results generated for all analysed load cases rather than only on the most critical cases.

6.2 -X Panel Results



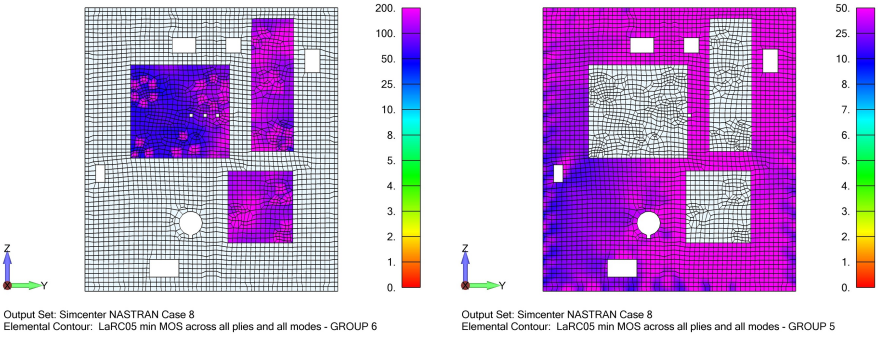
(a) Reinforced area (b) Unreinforced area

Figure 6.2: -X Panel - honeycomb MOS distribution - Load Case 8



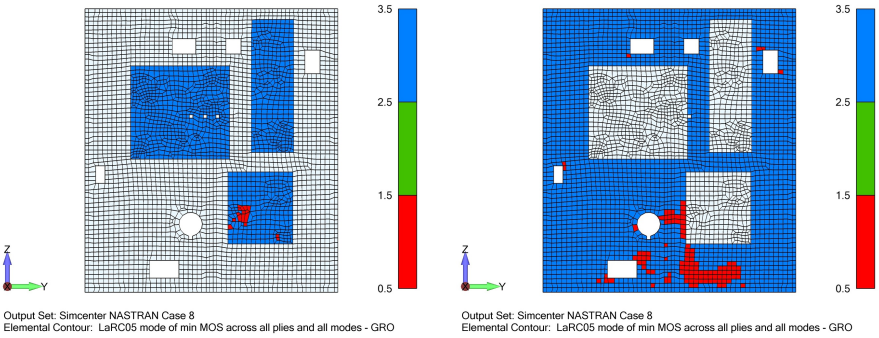
(a) Reinforced area (b) Unreinforced area

Figure 6.3: -X panel - Hoffman minimum MOS distribution - Load Case 8



(a) Reinforced area (b) Unreinforced area

Figure 6.4: -X panel - LaRC05 minimum MOS distribution - Load Case 8



(a) Reinforced area (b) Unreinforced area

Figure 6.5: -X panel - LaRC05 failure mode distribution - Load Case 8 (red = fibre tensile failure; green = matrix failure; blue = fibre kinking failure)

Gr. ID	Critical LC	Min MOS	Ply ID	Elem. ID	σ_x [Pa]	σ_y [Pa]	τ_{xy} [Pa]
5	8	4.45	14	440958	-38140000	617505	8052
6	8	19.42	2	442580	-12602800	22723	-66469

(a) Skins - Hoffman criterion

Gr. ID	Critical LC	Min MOS	Failure Mode	Ply ID	Elem. ID	σ_x [Pa]	σ_y [Pa]	σ_z [Pa]	τ_{xy} [Pa]	τ_{yz} [Pa]	τ_{xz} [Pa]
5	8	5.94	3	16	440425	-45953700	110348	0	182068	182	13759
6	8	24.45	3	2	442580	-12602800	22723	0	-66469	1542	493

(b) Skins - LaRC05 criterion

Gr. ID	Mat. ID	Ply ID	Critical LC	Min MOS	Elem. ID	Shear Strength [Pa]	τ_{xz} [Pa]
5	400002	9	6	4.54	441665	1380000	-144864
6	400005	17	2	7.11	442697	3300000	-236531

(c) Honeycomb core - L direction

Gr. ID	Mat. ID	Ply ID	Critical LC	Min MOS	Elem. ID	Shear Strength [Pa]	τ_{yz} [Pa]
5	400002	9	6	2.13	440485	760000	-141104
6	400005	17	2	10.94	442583	1900000	92551

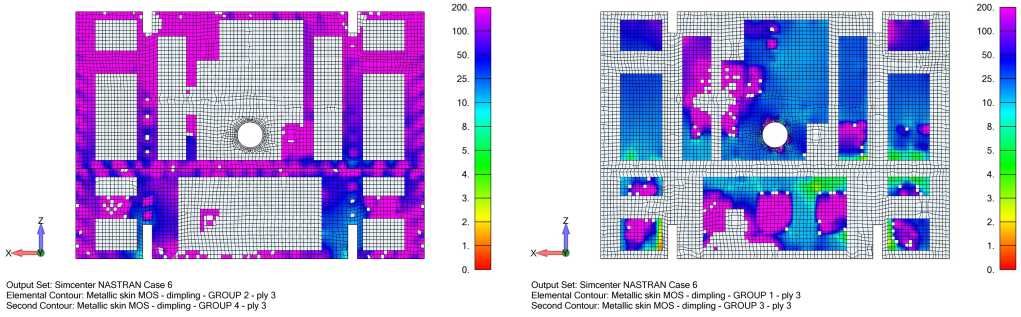
(d) Honeycomb core - W direction

Gr. ID	Mat. ID	Ply ID	Critical LC	Min MOS	Elem. ID	Shear Strength - L [Pa]	τ_{xz} [Pa]	Shear Strength - W [Pa]	τ_{yz} [Pa]
5	400002	9	6	2.12	440485	1380000	-20703	760000	-141104
6	400005	17	2	5.80	442697	3300000	-236531	1900000	88747

(e) Honeycomb core - combined shear

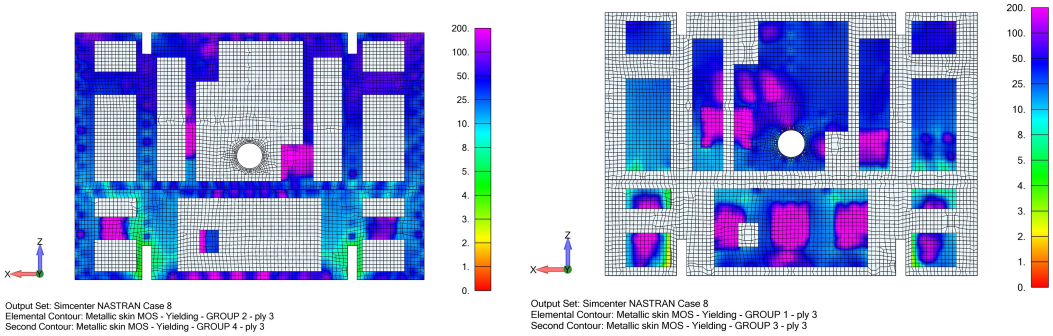
Table 6.3: -X Panel - Minimum MOS results

6.3 -Y Panel Results



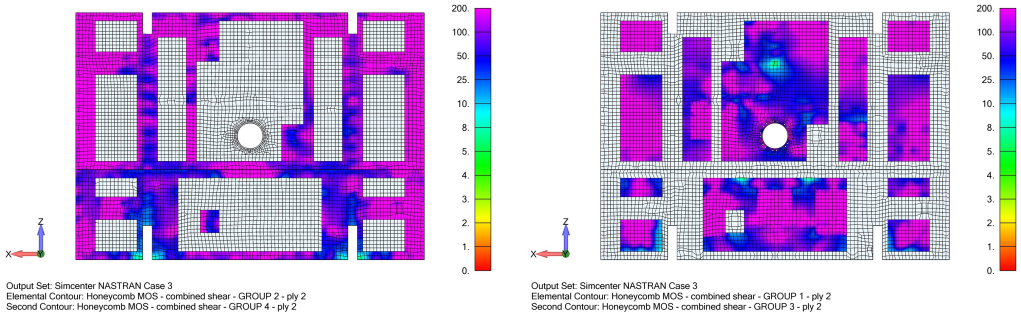
(a) Reinforced area (b) Unreinforced area

Figure 6.6: -Y panel - dimpling MOS distribution - Load case 6



(a) Reinforced area (b) Unreinforced area

Figure 6.7: -Y Panel - yielding MOS distribution - Load Case 8



(a) Reinforced area (b) Unreinforced area

Figure 6.8: -Y Panel - honeycomb MOS distribution - Load Case 3

Gr. ID	Crit. LC	Ply ID	Mat. ID	Min MOS	Elem. ID	Yielding Strength [Pa]	Von Mises Stress [Pa]
1	6	3	450001	4.58	472450	320000000	37942104
2	8	3	450001	5.24	470318	320000000	33899648
3	8	3	450001	1.45	481375	320000000	86427464
4	1	3	450001	0.88	480462	320000000	112433992

(a) Skins - yielding

Gr. ID	Crit. LC	Ply ID	Mat. ID	Min MOS	Elem. ID	Tensile Strength [Pa]	Von Mises Stress [Pa]
1	1	3	450001	8.07	474358	399000000	25603900
2	17	3	450001	7.94	471893	399000000	25962984
3	19	3	450001	3.54	481375	399000000	51111024
4	17	3	450001	1.56	480226	399000000	90594680

(b) Skins - tensile ultimate

Gr. ID	Crit. LC	Ply ID	Mat. ID	Min MOS	Elem. ID	Critical Stress [Pa]	Min. Prin. Stress [Pa]
1	6	3	450001	120.33	472450	8901543307	-42683900
2	6	3	450001	121.65	471667	7976739970	-37840400
3	8	3	450001	59.30	481375	8901543307	-85892096
4	1	3	450001	39.75	480462	7976739970	-113890000

(c) Skins - crimping

Gr. ID	Crit. LC	Ply ID	Mat. ID	Min MOS	Elem. ID	Critical Stress [Pa]	Min. Prin. Stress [Pa]
1	6	3	450001	5.90	472450	506400743	-42683900
2	6	3	450001	17.54	471667	1205781827	-37840400
3	8	3	450001	2.43	481375	506400743	-85892096
4	1	3	450001	5.16	480462	1205781827	-113890000

(d) Skins - wrinkling

Gr. ID	Crit. LC	Ply ID	Mat. ID	Min MOS	Elem. ID	Critical Stress [Pa]	Min. Prin. Stress [Pa]
1	6	3	450001	2.23	472450	236835479	-42683900
2	6	3	450001	13.57	471667	947341915	-37840400
3	8	3	450001	0.60	481375	236835479	-85892096
4	1	3	450001	3.84	480462	947341915	-113890000

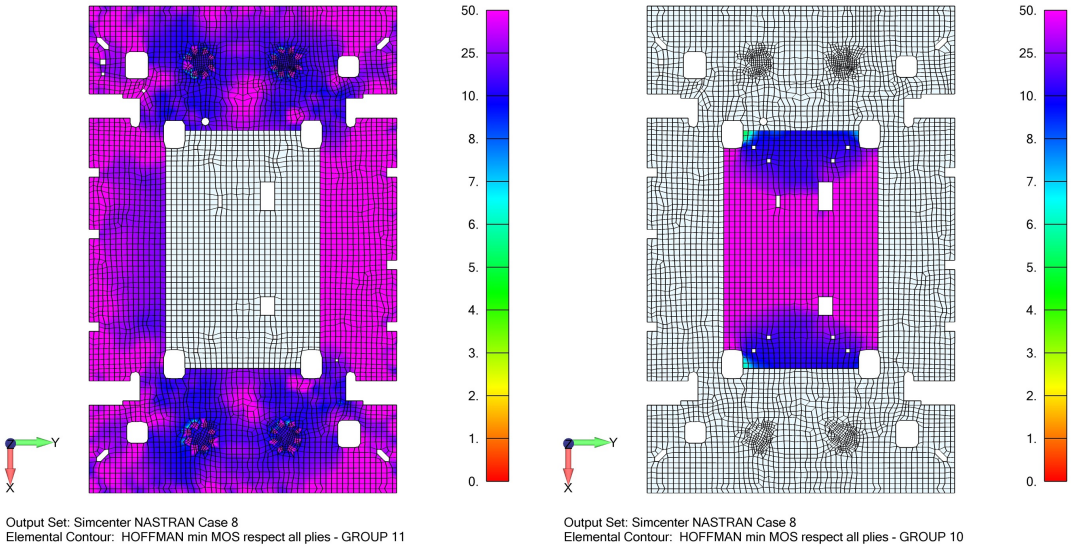
(e) Skins - dimpling

Gr. ID	Mat. ID	Ply ID	Crit. LC	Min MOS	Elem. ID	Shear Strength - L [Pa]	τ_{xz} [Pa]	Shear Strength - W [Pa]	τ_{yz} [Pa]
1	400002	2	3	2.66	472846	1380000	-74261	760000	113803
2	400005	2	2	6.88	471667	3300000	42793	1900000	-138119
3	400002	2	6	2.52	481815	1380000	13296	760000	-125342
4	400005	2	4	5.00	480455	3300000	319849	1900000	-2788

(f) Honeycomb core - combined shear

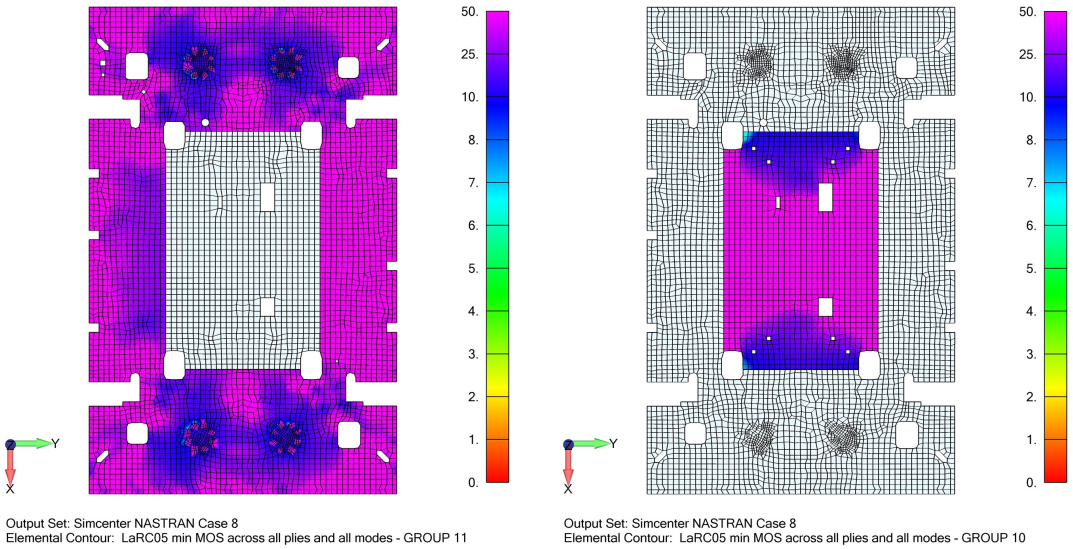
Table 6.4: -Y Panel - Minimum MOS results

6.4 -Z Panel Results



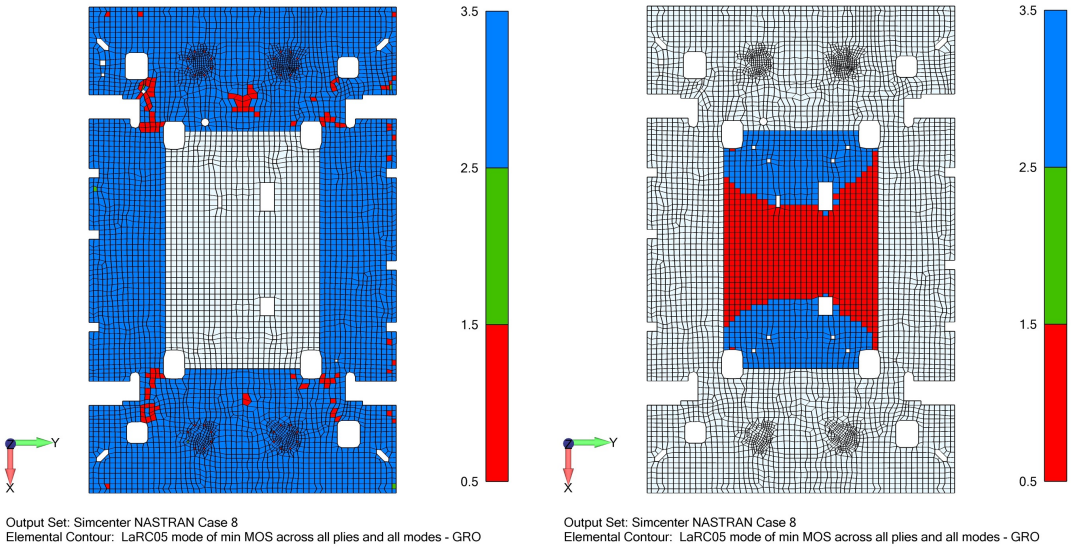
(a) Reinforced area (b) Unreinforced area

Figure 6.9: -Z panel - bottom skin - Hoffman minimum MOS distribution - Load Case 8



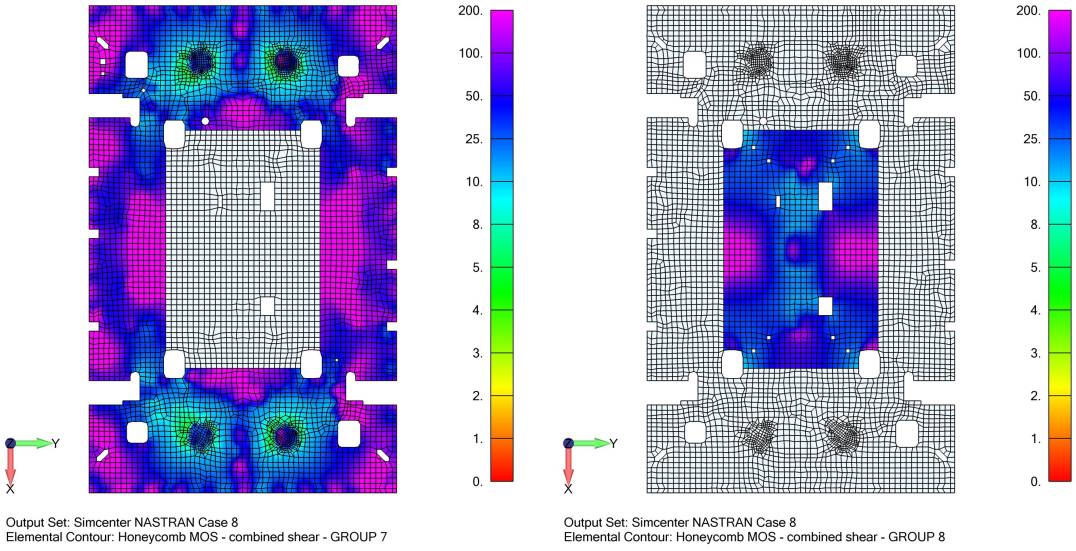
(a) Reinforced area (b) Unreinforced area

Figure 6.10: -Z panel - bottom skin - LaRC05 minimum MOS distribution - Load Case 8



(a) Reinforced area (b) Unreinforced area

Figure 6.11: -Z panel - LaRC05 failure mode distribution - Load Case 8 (red = fibre tensile failure; green = matrix failure; blue = fibre kinking failure)



(a) Reinforced area (b) Unreinforced area

Figure 6.12: -Z panel - honeycomb MOS distribution - Load Case 8

Gr. ID	Crit. LC	Min MOS	Ply ID	Elem. ID	σ_x [Pa]	σ_x [Pa]	τ_{xy} [Pa]
9	1	3.71	2	99044536	-58673800	-178140	-389725
10	8	5.05	1	99040743	-43216000	34845.5	43033
11	6	1.63	16	423682	-108988000	-591875	103443
12	17	7.10	1	420929	-30286400	152717	-91057

(a) Skins - Hoffman criterion

Gr. ID	Crit. LC	Min MOS	Failure Mode	Ply ID	Elem. ID	σ_x [Pa]	σ_y [Pa]	σ_z [Pa]	τ_{xy} [Pa]	τ_{yz} [Pa]	τ_{xz} [Pa]
9	8	4.30	3	1	99043794	-57371700	-111172	0	402334	-94.348602	-1799
10	8	6.19	3	1	99040743	-43216000	34845	0	43033	5.7841	-7058
11	6	1.85	3	16	423682	-108988000	-591875	0	103443	0	0
12	17	8.917509	3	1	420929	-30286400	152717	0	-91057	251	-2495

(b) Skins - LaRC05 criterion

Gr. ID	Mat. ID	Crit. LC	Min. MOS	Elem. ID	Shear Strength [Pa]	τ_{xz} [Pa]
7	200820	7	1.21	99051044	4620000	1217588
8	200710	2	3.63	99046196	1380000	-173545

(c) Honeycomb core - L direction

Gr. ID	Mat. ID	Crit. LC	Min. MOS	Elem. ID	Shear Strength [Pa]	τ_{yz} [Pa]
7	200820	8	1.53	99050694	2760000	-622860
8	200710	2	7.22	99052164	760000	-53769

(d) Honeycomb core - W direction

Gr. ID	Mat. ID	Crit. LC	Min. MOS	Elem. ID	Shear Strength - L [Pa]	τ_{xz} [Pa]	Shear Strength - W [Pa]	τ_{yz} [Pa]
7	200820	8	1.14	99050696	4620000	-1167126	2760000	-274698
8	200710	2	3.47	99046196	1380000	-173545	760000	25847

(e) Honeycomb core - combined shear

Table 6.5: -Z Panel - Minimum MOS results

6.5 Comparison of MOS predictions obtained with Hoffman and LaRC05

The comparison between the Hoffman and LaRC05 criteria was performed using the complete set of results obtained for the six composite structural groups considered in this study. Since 20 load cases were analysed for each group, the comparison is based on a total of 120 independent MOS evaluations, providing a sufficiently large dataset to identify general trends in the predictions of the two criteria.

Unlike the analysis presented in Chapter 5, where the objective was to assess the predictive capability of the failure criteria against experimental results, the purpose of the present comparison is different. Here, the focus is on quantifying the variation in the predicted MOS resulting from the use of the LaRC05 criterion instead of the Hoffman

criterion in a real industrial application. For this comparison, the MOS predicted by the Hoffman criterion is taken as the reference value, and the relative variation is computed as

$$\Delta MOS = \frac{MOS_{\text{LaRC05}} - MOS_{\text{Hoffman}}}{MOS_{\text{Hoffman}}} \times 100.$$

Table 6.6 summarises the relative variations obtained for the six analysed groups.

Group ID	**Group Title**	**Mean Var.** [%]	**Std. Dev.** [%]	**Max. Var.** [%]	**Min. Var.** [%]
5	-X panel - unreinforced area	**35.1**	15.8	96.2	20.1
6	-X panel - reinforced area	**27.3**	7.7	43.2	11.3
9	-Z panel - bottom skin - reinforced area	**19.0**	9.6	43.3	10.7
10	-Z panel - bottom skin - unreinforced area	**24.1**	10.6	48.1	10.9
11	-Z panel - top skin - reinforced area	**22.8**	15.4	55.4	7.3
12	-Z panel - top skin - unreinforced area	**19.4**	8.1	46.0	11.6

Table 6.6: Relative variation of the minimum MOS predicted by the LaRC05 criterion with respect to the Hoffman criterion

As shown in Table 6.6, the LaRC05 criterion systematically predicts higher MOS values than the Hoffman criterion for all the analysed groups. The average increase of the minimum MOS ranges from approximately 19% to 35%, indicating that LaRC05 consistently provides less conservative predictions.

Furthermore, the minimum variation obtained for each group remains positive. This means that, for all 120 analysed load cases, the MOS predicted by LaRC05 is always higher than the corresponding Hoffman prediction.

The standard deviation values indicate a moderate dispersion of the results within each group. This suggests that the observed differences are not associated with a limited number of specific load cases but rather represent a trend across the entire dataset. The largest variations are observed for the -X panel unreinforced area (group 5), where MOS increases approaching 100% are recorded for some load cases. Conversely, the remaining groups exhibit a more limited but still significant increase, generally ranging between 10% and 40%.

Chapter 7

Conclusions

The objective of this thesis was the development and enhancement of a Femap API for the automatic evaluation of structural Margins of Safety (MOS) of sandwich structures and composite laminates, with particular focus on the implementation and assessment of advanced failure criteria.

The work was carried out in collaboration with Thales Alenia Space and originated from the practical need to reduce the time required for finite element post-processing activities while improving the consistency and reliability of structural verification procedures. Starting from a pre-existing tool developed within the company, the API was updated to ensure compatibility with the latest Femap versions and extended in terms of functionality, usability, and analysis capabilities.

In particular, the API is capable of evaluating the MOS associated with the main failure modes of sandwich panels with both metallic and composite skins. In addition, dedicated graphical interfaces and automatic reporting capabilities were developed in order to facilitate its practical use within an industrial context.

A significant part of the work was devoted to the implementation of the LaRC05 formulation. Particular attention was paid to the implementation of the failure modes, in-situ strength formulations, and nonlinear shear behaviour. Moreover, a major advantage of this tool, even when compared to commercial software, is that it returns both the FI and MOS values calculated using the Hoffman and LaRC05 theories, thus providing an actual physical measure of the distance to failure.

The predictive capabilities of the Hoffman and LaRC05 criteria were assessed through a validation campaign based on experimental results available in the literature. Different laminate configurations and loading conditions were considered. Although both criteria systematically provided conservative predictions with respect to the experimental strengths, significant differences emerged in terms of predictive accuracy. The Hoffman criterion produced a mean relative error of approximately 35%, whereas the corresponding value obtained with LaRC05 was approximately 15%. The LaRC05 criterion also exhibited a lower standard deviation of the prediction error, indicating more robust behaviour across different laminate configurations and loading conditions.

Following the validation phase, the developed tool was applied to the analysis of

sandwich panels belonging to a real satellite structure. Different modelling approaches, metallic and composite skins, and multiple load cases were considered. This application demonstrated the capability of the tool to identify the critical load case, critical ply, and critical element associated with the minimum MOS within a large set of load cases, and to automatically generate tables ready to be included in satellite documentation.

The comparison between Hoffman and LaRC05 performed on the satellite case study provided particularly interesting results. Considering six independent structural groups and twenty load cases for each group, corresponding to a total of 120 independent evaluations, the LaRC05 criterion systematically predicted higher MOS values than Hoffman. Depending on the structural region considered, the average increase in the minimum MOS ranged between approximately 19% and 35%. These results suggest that physically-based criteria may significantly reduce the level of conservatism associated with traditional strength-based approaches.

Nevertheless, these results do not imply that one criterion should universally replace the other. The Hoffman criterion remains attractive because of its simplicity, robustness, and limited input requirements, making it particularly suitable for preliminary design activities and conservative assessments. Conversely, the LaRC05 formulation provides a more physically representative description of failure initiation and demonstrates superior predictive capabilities when a more accurate estimation of structural margins is required. The choice between the two approaches should therefore be an informed decision by the analyst, driven by the desired balance between modelling complexity, computational effort, and acceptable prediction error.

Despite the encouraging results obtained in this work, several limitations remain. The analyses are based on linear-elastic solutions and First-Ply-Failure criteria. Future developments could therefore focus on the integration of progressive damage methodologies and on the extension of the framework to three-dimensional multilayered composite modelling approaches. Besides improving the predictive capabilities of the methodology, such developments would allow a more rigorous comparison with experimental data reported in the literature. Indeed, experimental failure loads generally correspond to damage states that already include progressive degradation mechanisms, whereas the actual onset of first-ply failure is seldom identified or reported. This represents a common limitation of most validation exercises involving first-ply-failure criteria rather than a limitation specific to the present work.

The API, both in terms of design and implementation, has been developed to be easily extended for the automated calculation of MOS values associated with other structural components within satellite structures.

Overall, the developed API successfully bridges the gap between advanced composite failure analysis and practical industrial finite element post-processing. By combining automated post-processing capabilities, direct MOS evaluation, and the implementation of the LaRC05 failure criterion within a user-friendly environment, the tool provides an effective framework for the structural verification of sandwich panels with both metallic and composite skins in aerospace applications.

Bibliography

[1] Composite Materials Handbook-17 (CMH-17). SAE International on behalf of CMH-17, a division of Wichita State University, 2013. ISBN: 978-0-7680-7816-9. URL: https://app.knovel.com/hotlink/pdf/id:kt00U8TJ62/composite-materials-handbook/sandwich-panel-failure.

[2] ANSYS, Inc. *Composites Theory Reference*. ANSYS Documentation. Release 2025 R1. Canonsburg, PA, USA: ANSYS, Inc., 2025. URL: https://ansyshelp.ansys.com/public/Views/Secured/corp/v251/en/pdf/Composites_Theory_Reference.pdf.

[3] A. S. Argon. "Fracture of Composites". In: *Treatise on Materials Science and Technology*. Vol. 1. Academic Press, 1972, pp. 79–114.

[4] Qida Bing and C.T. Sun. "Specimen size effect in off-axis compression tests of fiber composites". In: *Composites Part B: Engineering* 39.1 (2008). Marine Composites and Sandwich Structures, pp. 20–26. ISSN: 1359-8368. DOI: https://doi.org/10.1016/j.compositesb.2007.02.010. URL: https://www.sciencedirect.com/science/article/pii/S1359836807000339.

[5] T. N. Bitzer. *Honeycomb Technology: Materials, Design, Manufacturing, Applications and Testing*. Available via ProQuest Ebook Central. Dordrecht: Springer Netherlands, 1997. ISBN: 978-0-412-54050-8.

[6] Thomas Bru. "Material characterisation for crash modelling of composites [PhD thesis]". PhD thesis. Nov. 2018. DOI: 10.13140/RG.2.2.10536.01280.

[7] P.P. Camanho, P. Maimí, and C.G. Dávila. "Prediction of size effects in notched laminates using continuum damage mechanics". In: *Composites Science and Technology* 67.13 (2007), pp. 2715–2727. ISSN: 0266-3538. DOI: https://doi.org/10.1016/j.compscitech.2007.02.005. URL: https://www.sciencedirect.com/science/article/pii/S0266353807000796.

[8] Pedro P. Camanho et al. "Prediction of in situ strengths and matrix cracking in composites under transverse tension and in-plane shear". In: *Composites Part A: Applied Science and Manufacturing* 37.2 (2006). CompTest 2004, pp. 165–176. ISSN: 1359-835X. DOI: https://doi.org/10.1016/j.compositesa.2005.04.023.

[9] G. Catalanotti. "Prediction of in situ strengths in composites: Some considerations". In: *Composite Structures* 207 (2019), pp. 889–893. ISSN: 0263-8223. DOI: https://doi.org/10.1016/j.compstruct.2018.09.075. URL: https://www.sciencedirect.com/science/article/pii/S0263822318334032.

[10] G. Catalanotti, P.P. Camanho, and A.T. Marques. "Three-dimensional failure criteria for fiber-reinforced laminates". In: *Composite Structures* 95 (2013), pp. 63–79. ISSN: 0263-8223. DOI: https://doi.org/10.1016/j.compstruct.2012.07.016. URL: https://www.sciencedirect.com/science/article/pii/S0263822312003443.

[11] Michael W. Czabaj and James G. Ratcliffe. "Comparison of intralaminar and interlaminar mode I fracture toughnesses of a unidirectional IM7/8552 carbon/epoxy composite". In: *Composites Science and Technology* 89 (2013), pp. 15–23. ISSN: 0266-3538. DOI: https://doi.org/10.1016/j.compscitech.2013.09.008. URL: https://www.sciencedirect.com/science/article/pii/S0266353813003709.

[12] Isaac M. Daniel and Ori Ishai. *Engineering Mechanics of Composite Materials (2nd Edition)*. Oxford University Press, 2006. ISBN: 978-0-19-515097-1. URL: https://app.knovel.com/hotlink/toc/id:kpEMCME002/engineering-mechanics/engineering-mechanics.

[13] Carlos G. Davila and Pedro P. Camanho. *Failure Criteria for FRP Laminates in Plane Stress*. NASA Technical Memorandum NASA/TM-2003-212663. NASA Langley Research Center, 2003. URL: https://ntrs.nasa.gov/citations/20040001363.

[14] M.F.S.F. de Moura et al. "Interlaminar and intralaminar fracture characterization of composites under mode I loading". In: *Composite Structures* 92.1 (2010), pp. 144–149. ISSN: 0263-8223. DOI: https://doi.org/10.1016/j.compstruct.2009.07.012. URL: https://www.sciencedirect.com/science/article/pii/S0263822309002475.

[15] Vishwas Divse, Deepak Marla, and Suhas S. Joshi. "Progressive damage analysis in an open hole compression of FRP laminates including fiber kinking and pre-existing damage". In: *Composites Part A: Applied Science and Manufacturing* 169 (2023), p. 107523. ISSN: 1359-835X. DOI: https://doi.org/10.1016/j.compositesa.2023.107523. URL: https://www.sciencedirect.com/science/article/pii/S1359835X23000994.

[16] George J. Dvorak and Norman Laws. "Analysis of Progressive Matrix Cracking In Composite Laminates II. First Ply Failure". In: *Journal of Composite Materials* 21 (1987), pp. 309–329. URL: https://doi.org/10.1177/002199838702100402.

[17] European Cooperation for Space Standardization (ECSS). *ECSS-E-ST-32-10C Rev.2: Structural Factors of Safety for Spaceflight Hardware*. Tech. rep. ECSS-E-ST-32-10C Rev.2. Noordwijk, The Netherlands: ESA-ESTEC, 2019. URL: https://ecss.nl/standard/ecss-e-st-32-10c-rev-2-structural-factors-of-safety-for-spaceflight-hardware-15-may-2019/.

[18] G. Frossard et al. “Ply thickness dependence of the intralaminar fracture in thin-ply carbon-epoxy laminates”. In: *Composites Part A: Applied Science and Manufacturing* 109 (2018), pp. 95–104. ISSN: 1359-835X. DOI: https://doi.org/10.1016/j.compositesa.2018.03.001. URL: https://www.sciencedirect.com/science/article/pii/S1359835X18300952.

[19] C. Furtado et al. “Is there a ply thickness effect on the mode I intralaminar fracture toughness of composite laminates?” In: *Theoretical and Applied Fracture Mechanics* 107 (2020), p. 102473. ISSN: 0167-8442. DOI: https://doi.org/10.1016/j.tafmec.2020.102473. URL: https://www.sciencedirect.com/science/article/pii/S0167844219303611.

[20] Amedeo Grasso. “Implementation of classical and advanced failure criteria for composite layered structures in FEMAP ad assessment of results”. Master’s Thesis. Torino, Italy: Politecnico di Torino, 2018.

[21] Jiefei Gu et al. “A theoretical and experimental assessment of 3D macroscopic failure criteria for predicting pure inter-fiber fracture of transversely isotropic UD composites”. In: *Composite Structures* 259 (2021), p. 113466. ISSN: 0263-8223. DOI: https://doi.org/10.1016/j.compstruct.2020.113466. URL: https://www.sciencedirect.com/science/article/pii/S026382232033395X.

[22] Hong T. Hahn and Stephen W. Tsai. “Nonlinear Elastic Behavior of Unidirectional Composite Laminae”. In: *Journal of Composite Materials* 7.1 (1973), pp. 102–118. DOI: 10.1177/002199837300700108. URL: https://doi.org/10.1177/002199837300700108.

[23] Z. Hashin. “Failure Criteria for Unidirectional Fiber Composites”. In: *Journal of Applied Mechanics* 47.2 (June 1980), pp. 329–334. ISSN: 0021-8936. DOI: 10.1115/1.3153664. URL: https://doi.org/10.1115/1.3153664.

[24] Rik Heslehurst. *Composite Sandwich Structure Design Requirements – Part 6: Failure Modes and Analysis*. 2021. URL: https://www.compositesaustralia.com.au/wp-content/uploads/2021/08/3.6-Composite-Sandwich-Structure-Design-Part-6-Failure-Modes-and-Analysis.pdf.

[25] Hexcel Composites. *Honeycomb Sandwich Design Technology*. Tech. rep. Publication No. AGU 075b. Hexcel Composites, 2000. URL: https://www.hexcel.com/wp-content/uploads/2026/01/Honeycomb_Sandwich_Design_Technology.pdf.

[26] Hexcel Corporation. *Defense and Space*. Accessed: 2026-05-29. 2026. URL: https://www.hexcel.com/industries/defense-space/.

[27] Hexcel Corporation. *HexPly® 8552 Epoxy Matrix (180°C/356°F Curing Matrix) Product Data Sheet*. 2025. URL: https://www.hexcel.com/wp-content/uploads/2025/12/HexPly_8552_eu_DataSheet1.pdf.

[28] M.J. Hinton, A.S. Kaddour, and P.D. Soden. "Chapter 1.1 - The world-wide failure exercise: Its origin, concept and content". In: *Failure Criteria in Fibre-Reinforced-Polymer Composites*. Ed. by M.J. Hinton, A.S. Kaddour, and P.D. Soden. Oxford: Elsevier, 2004, pp. 2–28. ISBN: 978-0-08-044475-8. DOI: https://doi.org/10.1016/B978-008044475-8/50002-0. URL: https://www.sciencedirect.com/science/article/pii/B9780080444758500020.

[29] Oscar Hoffman. "The Brittle Strength of Orthotropic Materials". In: *Journal of Composite Materials* 1.2 (1967), pp. 200–206. DOI: 10.1177/002199836700100210. URL: https://doi.org/10.1177/002199836700100210.

[30] Philip Irving and Constantinos Soutis. *Polymer Composites in the Aerospace Industry (2nd Edition)*. Elsevier, 2020. ISBN: 978-0-08-102679-3. URL: https://app.knovel.com/hotlink/toc/id:kpPCAIE001/polymer-composites-in/polymer-composites-in.

[31] Guenther Jacobsen. "Mechanical Characterization of Stretch Broken Carbon Fiber Materials – IM7 Fiber in 8552 Resin". In: (2026). Accessed: 2026-05-25. URL: https://www.hexcel.com/wp-content/uploads/2026/01/MechanicalCharacterizationofStretchBrokenCarbonFiber.pdf.

[32] AS Kaddour and MJ Hinton. "Maturity of 3D failure criteria for fibre-reinforced composites: Comparison between theories and experiments: Part B of WWFE-II". In: *Journal of Composite Materials* 47.6-7 (2013), pp. 925–966. DOI: 10.1177/0021998313478710. eprint: https://doi.org/10.1177/0021998313478710. URL: https://doi.org/10.1177/0021998313478710.

[33] H. Koerber, J. Xavier, and P.P. Camanho. "High strain rate characterisation of unidirectional carbon-epoxy IM7-8552 in transverse compression and in-plane shear using digital image correlation". In: *Mechanics of Materials* 42.11 (2010), pp. 1004–1019. ISSN: 0167-6636. DOI: https://doi.org/10.1016/j.mechmat.2010.09.003. URL: https://www.sciencedirect.com/science/article/pii/S0167663610001262.

[34] László P. Kollár and George S. Springer. *Mechanics of Composite Structures*. Cambridge University Press, 2003. ISBN: 978-0-521-80165-2. URL: https://app.knovel.com/hotlink/toc/id:kpMCS00005/mechanics-composite-structures/mechanics-composite-structures.

[35] M.J. Laffan et al. "Translaminar fracture toughness testing of composites: A review". In: *Polymer Testing* 31.3 (2012), pp. 481–489. ISSN: 0142-9418. DOI: https://doi.org/10.1016/j.polymertesting.2012.01.002. URL: https://www.sciencedirect.com/science/article/pii/S0142941812000049.

[36] Robert P. Ley, Weichuan Lin, and Uy Mbanfo. *Facesheet Wrinkling in Sandwich Structures*. Contractor Report NASA/CR-1999-208994. Document ID: 19990017863. Hampton, VA, USA: NASA Langley Research Center, Jan. 1999.

[37] Kristin Marlett. *Hexcel 8552 IM7 Unidirectional Prepreg 190 gsm & 35% RC Qualification Material Property Data Report*. NCAMP Test Report CAM-RP-2009-015 Rev A. FAA Special Project Number SP4614WI-Q. Wichita, Kansas, USA: National Institute for Aviation Research, Wichita State University, Apr. 2011. URL: https://thyme.ornl.gov/CFCrush/materials/uou/CAM-RP-2009-015_Rev_A_April_22_2011_Hexcel_8552_IM7_Uni_Data_Report.pdf.

[38] MSC Software Corporation. *MSC Nastran Reference Guide*. Accessed via MSC Patran installation (local documentation). 2024.

[39] P. Nali and E. Carrera. "A numerical assessment on two-dimensional failure criteria for composite layered structures". In: *Composites Part B: Engineering* 43.2 (2012), pp. 280–289. ISSN: 1359-8368. DOI: https://doi.org/10.1016/j.compositesb.2011.06.018.

[40] Charles B. Norris, Kenneth H. Boller, and Arnold W. Voss. *Wrinkling of the Facings of Sandwich Construction Subjected to Edgewise Compression: Sandwich Constructions Having Honeycomb Cores*. Tech. rep. Report No. 1810-A. Prepared in cooperation with the University of Wisconsin. Madison, Wisconsin: Forest Products Laboratory, U.S. Department of Agriculture, 1953. URL: https://apps.dtic.mil/sti/tr/pdf/AD0015257.pdf.

[41] J.P. Nunes and J.F. Silva. "5 - Sandwiched composites in aerospace engineering". In: *Advanced Composite Materials for Aerospace Engineering*. Ed. by Sohel Rana and Raul Fangueiro. Woodhead Publishing, 2016, pp. 129–174. ISBN: 978-0-08-100939-0. DOI: https://doi.org/10.1016/B978-0-08-100037-3.00005-5. URL: https://www.sciencedirect.com/science/article/pii/B9780081000373000055.

[42] T. Kevin O'Brien and Ronald Krueger. *Analysis of Ninety Degree Flexure Tests for Characterization of Composite Transverse Tensile Strength*. Technical Memorandum NASA/TM-2001-211227, ARL-TR-2568. Hampton, Virginia: NASA Langley Research Center and U.S. Army Research Laboratory, 2001.

[43] A.C. Orifici, I. Herszberg, and R.S. Thomson. "Review of methodologies for composite material modelling incorporating failure". In: *Composite Structures* 86.1 (2008). Fourteenth International Conference on Composite Structures, pp. 194–210. ISSN: 0263-8223. DOI: https://doi.org/10.1016/j.compstruct.2008.03.007. URL: https://www.sciencedirect.com/science/article/pii/S0263822308000810.

[44] Federico Paris, Michael Wisnom, and Yentl Swolfs. *Mode I interlaminar fracture toughness and the factors affecting it*. Tech. rep. University of Bristol, 2023. URL: https://www.bristol.ac.uk/media-library/sites/composites/documents/toughness-workshop-140524/Mode%20I%20interlaminar%20fracture%20toughness%20and%20the%20factors%20affecting%20it%20-%20paper.pdf.

[45] Peter A. Parker and William H. Prosser. *Mechanics Leading to Stress Rupture Failure in Carbon Fiber Composite Overwrapped Pressure Vessels (COPVs)*. Tech.

rep. NASA/TM-20260002192. NASA Technical Memorandum. National Aeronautics and Space Administration (NASA), 2020. URL: https://ntrs.nasa.gov/api/citations/20200002195/downloads/20200002195.pdf.

[46] S.T. Pinho, P. Robinson, and L. Iannucci. "Developing a four point bend specimen to measure the mode I intralaminar fracture toughness of unidirectional laminated composites". In: *Composites Science and Technology* 69.7 (2009), pp. 1303–1309. ISSN: 0266-3538. DOI: https://doi.org/10.1016/j.compscitech.2009.03.007. URL: https://www.sciencedirect.com/science/article/pii/S0266353809001067.

[47] Silvestre T. Pinho et al. *Failure Models and Criteria for FRP Under In-Plane or Three-Dimensional Stress States Including Shear Non-Linearity*. NASA Technical Memorandum NASA/TM-2005-213530. NASA Langley Research Center, 2005. URL: https://ntrs.nasa.gov/citations/20050110223.

[48] ST Pinho et al. "Material and structural response of polymer-matrix fibre-reinforced composites". In: *Journal of Composite Materials* 46.19-20 (2012), pp. 2313–2341. DOI: 10.1177/0021998312454478. URL: https://doi.org/10.1177/0021998312454478.

[49] Jr. Poe C. C. *Fracture Toughness of Fibrous Composite Materials*. Technical Publication NASA-TP-2370. Report Numbers: NAS 1.60:2370, L-15848. Hampton, VA, USA: NASA Langley Research Center, 1984. URL: https://ntrs.nasa.gov/citations/19850002828.

[50] A. Puck and H. Schürmann. "FAILURE ANALYSIS OF FRP LAMINATES BY MEANS OF PHYSICALLY BASED PHENOMENOLOGICAL MODELS". In: *Composites Science and Technology* 58.7 (1998), pp. 1045–1067. ISSN: 0266-3538. DOI: https://doi.org/10.1016/S0266-3538(96)00140-6. URL: https://www.sciencedirect.com/science/article/pii/S0266353896001406.

[51] P. Robinson and J.M. Hodgkinson. "9 - Interlaminar fracture toughness". In: *Mechanical Testing of Advanced Fibre Composites*. Ed. by J.M. Hodgkinson. Woodhead Publishing Series in Composites Science and Engineering. Woodhead Publishing, 2000, pp. 170–210. ISBN: 978-1-85573-312-1. DOI: https://doi.org/10.1533/9781855738911.170. URL: https://www.sciencedirect.com/science/article/pii/B9781855733121500135.

[52] B. W. Rosen. "Mechanics of Composite Strengthening". In: *Fiber Composite Materials*. Metals Park, OH: American Society of Metals, 1965, pp. 37–75.

[53] N. Sela and O. Ishai. "Interlaminar fracture toughness and toughening of laminated composite materials: a review". In: *Composites* 20.5 (1989), pp. 423–435. ISSN: 0010-4361. DOI: https://doi.org/10.1016/0010-4361(89)90211-5. URL: https://www.sciencedirect.com/science/article/pii/0010436189902115.

[54] Siemens Digital Industries Software. *Femap API Guide: Simcenter Femap 2412 Series*. Accessed via Femap installation (local documentation). 2024.

[55] Siemens Digital Industries Software. *Femap Commands Guide: Simcenter Femap 2412 Series*. Accessed via Femap installation (local documentation). 2024.

[56] P.D Soden, A.S Kaddour, and M.J Hinton. "Recommendations for designers and researchers resulting from the world-wide failure exercise". In: *Composites Science and Technology* 64.3 (2004). Failure criteria in fibre reinforced polymer composites Part C: Additional theories conclusions and recommendations, pp. 589–604. ISSN: 0266-3538. DOI: https://doi.org/10.1016/S0266-3538(03)00228-8. URL: https://www.sciencedirect.com/science/article/pii/S0266353803002288.

[57] *Space engineering – Structural materials handbook – Part 3: Load transfer and design of joints and design of structures*. ECSS-E-HB-32-20 Part 3A. European Cooperation for Space Standardization (ECSS). 2011. URL: https://ecss.nl/wp-content/uploads/handbooks/ecss-e-hb/ECSS-E-HB-32-20_Part3A.pdf.

[58] George H. Staab. *Laminar Composites (2nd Edition)*. Elsevier, 2015. ISBN: 978-0-12-802400-3. URL: https://app.knovel.com/hotlink/toc/id:kpLCE00001/laminar-composites-2nd/laminar-composites-2nd.

[59] *Standard Test Method for Compressive Properties of Polymer Matrix Composite Materials Using a Combined Loading Compression (CLC) Test Fixture*. West Conshohocken, PA: ASTM International, 2023. DOI: 10.1520/D6641_D6641M-23.

[60] *Standard Test Method for In-Plane Shear Response of Polymer Matrix Composite Materials by Tensile Test of a ±45° Laminate*. Reapproved 2025. West Conshohocken, PA: ASTM International, 2025. DOI: 10.1520/D3518_D3518M-18R25.

[61] *Standard Test Method for Open-Hole Compressive Strength of Polymer Matrix Composite Laminates*. ASTM D6484/D6484M-23. ASTM International, 2023.

[62] *Standard Test Method for Open-Hole Tensile Strength of Polymer Matrix Composite Laminates*. ASTM D5766/D5766M-23. ASTM International, 2023.

[63] *Standard Test Method for Short-Beam Strength of Polymer Matrix Composite Materials and Their Laminates*. West Conshohocken, PA: ASTM International, 2022. DOI: 10.1520/D2344_D2344M-22.

[64] *Standard Test Method for Tensile Properties of Polymer Matrix Composite Materials*. West Conshohocken, PA: ASTM International, 2025. DOI: 10.1520/D3039_D3039M-17R25.

[65] Yentl Swolfs, Federico Paris, and Michael R. Wisnom. *Is fracture toughness applicable as a material property for composites?* Tech. rep. University of Bristol, 2023. URL: https://www.bristol.ac.uk/media-library/sites/composites/news/2023/Toughness%20paper%20final.pdf.

[66] Thales Alenia Space. *Lanciato con successo il satellite per l'osservazione della Terra Sentinel-1D*. 2024. URL: https://www.thalesaleniaspace.com/it/press-releases/lanciato-con-successo-il-satellite-losservazione-della-terra-sentinel-1d.

[67] Su Yu and Jonathan S. Colton. "A compact open-hole compression test fixture for composite materials". In: *Composites Part B: Engineering* 223 (2021), p. 109126. ISSN: 1359-8368. DOI: https://doi.org/10.1016/j.compositesb.2021.109126. URL: https://www.sciencedirect.com/science/article/pii/S1359836821005102.

Appendix A

Femap API Upgrade: Implementation Aspects

A.1 Implementation Examples

The following subsections present two representative examples of the modifications introduced during the API upgrade. These examples are provided for illustrative purposes only and are intended to give insight into the software implementation. They are not required for understanding the use of the developed tool.

Access to Nastran results

The following code snippets compare the implementation used in previous API versions with the updated approach based on the Results Browsing Object (RBO). The code extracts the in-plane stress components σ_1, σ_2, and τ_{12} for the current ply, which are required for the evaluation of the Hoffman failure criterion. The implementation is executed within nested loops over load cases and laminate plies.

In both implementations, the variables `s1`, `s2`, and `t12` are vectors whose length corresponds to the number of analysed elements and store the stress components for the considered ply. `fmpElSet` is a Set object containing the IDs of the elements included in the analysis, while `v` represents the current ply index, starting from zero.

```
1       s1 = Nothing
2       s2 = Nothing
3       t12 = Nothing
4
5       rc = fmpOut.Get(1000020 + 200 * v)   'Reading stress component
6       rc = fmpOut.GetScalarAtElemSet(fmpElSet.ID, s1)   'Saving stress component
7       rc = fmpOut.Get(1000021 + 200 * v)
8       rc = fmpOut.GetScalarAtElemSet(fmpElSet.ID, s2)
9       rc = fmpOut.Get(1000023 + 200 * v)
10      rc = fmpOut.GetScalarAtElemSet(fmpElSet.ID, t12)
```

The code above represents the implementation adopted in previous versions of the

API. The object `fmpOut` is an instance of the *Output Object*. The method `Get` retrieves an output vector based on its ID, while `GetScalarAtElemSet` extracts the corresponding data for the elements defined in the Set and stores it in the output vector.

In previous versions of Femap, the ID corresponding to σ_1 for the first ply was 1000020, with a constant offset of 200 between consecutive plies. Therefore, the ID for the current ply could be computed as $1000020 + 200 \cdot v$. However, in newer API versions this offset has changed (e.g. to 500). As a result, using hard-coded IDs with updated API methods may lead to runtime errors or, more critically, to retrieving incorrect output vectors. This highlights the importance of avoiding hard-coded values, which can compromise both robustness and consistency with the software.

The updated implementation using the RBO is shown below.

```
1       s1 = Nothing
2       s2 = Nothing
3       t12 = Nothing
4       iCols1 = Nothing
5       iCols2 = Nothing
6       iColt12 = Nothing
7
8       ' ------------------- Reading stress components -------------------
9       fmpRbo.DataNeeded(zDataType.FT_ELEM, fmpElSet.ID)
10      rc = fmpRbo.AddColumnV2(vOCids(i), idQuery.Laminate(zVecPlateResult.VPV_STRESS,
        ↪  zVecPlateType.VPT_X, v + 1, zVecPlateLoc.VPL_CENTROID), False, nCols, iCols1)
11      rc = fmpRbo.AddColumnV2(vOCids(i), idQuery.Laminate(zVecPlateResult.VPV_STRESS,
        ↪  zVecPlateType.VPT_Y, v + 1, zVecPlateLoc.VPL_CENTROID), False, nCols, iCols2)
12      rc = fmpRbo.AddColumnV2(vOCids(i), idQuery.Laminate(zVecPlateResult.VPV_STRESS,
        ↪  zVecPlateType.VPT_XY, v + 1, zVecPlateLoc.VPL_CENTROID), False, nCols, iColt12)
13
14      rc = fmpRbo.Populate()
15
16      ' ------------------- Saving stress components -------------------
17      rc = fmpRbo.GetScalarAtElemSetV2(iCols1(0), fmpElSet.ID, s1)
18      rc = fmpRbo.GetScalarAtElemSetV2(iCols2(0), fmpElSet.ID, s2)
19      rc = fmpRbo.GetScalarAtElemSetV2(iColt12(0), fmpElSet.ID, t12)
20
21      ' ------------------- RBO reset -------------------
22      fmpRbo.clear()
```

The RBO can be interpreted as a table in which each column corresponds to a specific output quantity. Before defining the columns, the method `DataNeeded` must be called to specify the set of entities for which the results are required.

The method `AddColumnV2` defines new columns by specifying the analysis set ID (stored in `vOCids(i)`), the desired result ID, and a boolean variable that, if set to True, enables the addition of multiple columns to represent vector components [54].

In this implementation, the `idQuery` object (an instance of a *Results Vector ID Query Object*) is used to generate the appropriate output vector ID based on descriptive input parameters. This approach eliminates hard-coded IDs and ensures compatibility with future API updates.

The outputs of `AddColumnV2` are `nCols`, which stores the number of columns added to the RBO, and a variable (respectively `iCols1`, `iCols2` and `iColt12` in the three uses) that stores the indices of the created columns.

A crucial aspect of this implementation is the initialization of the variables used to store the results. The variables `s1`, `s2`, `t12`, `iCols1`, `iCols2`, and `iColt12` must be reset before each use, as the RBO methods require "clean" variables to operate correctly.

The method `Populate` loads the analysis results into the defined columns; before this call, no data are available in the RBO. Once `Populate` has been executed, no further modifications to the column definitions are allowed.

The method `GetScalarAtElemSetV2` retrieves the data associated with a given column index (first input) for the elements defined by the element set (second input), and stores them in the corresponding vector (third input).

Finally, the RBO is reset using the `Clear` method. This step is essential because the same RBO instance is used both for reading results and for creating new output vectors. Clearing the RBO ensures consistency between successive operations and prevents unintended interactions. In addition, without resetting the RBO, subsequent calls to `Populate` would not be possible, as the object would already contain populated data.

Creation of custom output vectors

A key feature of the developed API is the introduction of custom output vectors, enabling direct visualization of results within the Femap post-processing environment (see also Section A.2). The method used to create these vectors has been updated accordingly. First, the implementation based on the previous API version is presented. As in the previous example, `fmpOut` is an instance of the *Output Object*.

```
1       vTitle = "Lam Ply" & v + 1 & " HOFFMAN MOS INDEX (FULL MODEL)"
2       rc = fmpOut.InitScalarAtElem(vOCids(i), 9519221 + v, vTitle, 0, True)
3       rc = fmpOut.PutScalarAtElem(nEl, ElIds, MOS)
4       rc = fmpOut.Put(-1)
```

The method `InitScalarAtElem` initialized the object to create an output vector containing a scalar value at each element. Its inputs are the output set ID (`vOCids(i)`), the output vector ID (`9519221 + v`), the vector title (`vTitle`), the output category (here set to 0, i.e. "Any"), and a boolean flag indicating whether the result can be linearly combined.

The method `PutScalarAtElem` then stored the data by providing the number of entries, the element IDs, and the corresponding values [54]. Finally, `Put` writes the output vector to the model database.

The updated implementation based on the RBO is shown below.

```
1       vTitle = "Lam Ply" & v + 1 & " HOFFMAN MOS (FULL MODEL)"
2       rc = fmpRbo.AddScalarAtElemColumnV2(vOCids(i),
        ↪  GetOutputVectorID(ResultMode.MOS_Hoffman, MOS_Hoffman_Result.MOSply, 0, v + 1),
        ↪  vTitle, 0, True, iColOV)
3       fmpRbo.SetScalarAtElemColumnV2(iColOV, nEl, ElIds, MOS)
4       fmpRbo.Save()
5       fmpRbo.Clear()
```

The methods `InitScalarAtElem` and `PutScalarAtElem`, associated with the *Output Object*, are obsolete and not available for the RBO. Their functionality is replaced by `AddScalarAtElemColumnV2` and `SetScalarAtElemColumnV2`.

Since the RBO can be interpreted as a data table, an additional parameter is required compared to the obsolete methods: the column index (`iColOV`), which identifies the column being created or accessed.

The `Save` method replaces the obsolete `Put` method and stores the output vector in the Femap database. Once `Save` has been called, the RBO cannot be modified. For this reason, and for consistency with the workflow described in the previous section, the RBO must be reset after each use by calling the `Clear` method.

To avoid hard-coded values and improve readability and maintainability, a custom function (`GetOutputVectorID`) has been introduced. Similarly to the ID query mechanism used for reading results, this function generates the output vector ID from descriptive input parameters, ensuring consistency with the adopted standardization (section A.2).

A.2 Standardization of the Output Vector IDs

In earlier API versions, no standardized structure for output vector IDs was defined. While this did not prevent usage, it significantly complicated development by making it difficult to identify available output slots. This lack of convention is particularly problematic for new developers, as it renders the management and extension of output vectors error-prone and time-consuming. With newer API versions and the introduction of additional output vectors, a standardized ID structure has been implemented to ensure consistent integration and usability.

Based on the guidelines provided in the official Femap API documentation [54], a standardized convention for output vector IDs has been adopted. In particular, only the ranges designated for user-defined outputs are used, in order to avoid conflicts with vectors automatically generated by NASTRAN. Accordingly, the output vector ID, consisting of 8 digits, is structured as:

$$NN - M - R - GG - PP$$

where each field is defined in Table A.1. For each one, more details are given in table A.2 and A.3.

Field	Description
NN	Prefix identifying the group range
M	Result mode (analysis type)
R	Specific result within the selected mode
GG	The tens and units digits of the group ID (00 = full model)
PP	Ply ID (00 when referring to the whole laminate)

Table A.1: Structure of the output vector ID

NN	Description
24	Full model or groups 1–99
49	Groups 100–199
74	Groups 200–299
99	Groups 300–399

Table A.2: Prefix definition (NN)

For sandwich panel MOS, the value of PP depends on the modelling approach used: it corresponds to the ply ID when the sandwich is modelled as an equivalent 2D laminate, whereas $PP = 00$ when the sandwich is modelled with a solid honeycomb core and 2D plate skins.

To enforce the proposed standardization, a dedicated function `GetOutputVectorID` has been implemented in VB.NET and integrated into the API. This function automatically generates the output vector ID based on the selected result mode, result type, group ID, and ply ID, ensuring consistency and eliminating the risk of manual errors. An example of how it has been used is provided in the section A.1.

The adoption of this standardization provides several advantages:

- the result mode field (M) still allows for additional expansion. Since not all possible values are currently used, up to three additional (M = 8,9,0) analysis modes can be introduced in the future without modifying the existing structure.
- the defined prefix strategy (NN) ensures that results associated with groups having ID up to 399 are uniquely mapped and never overwritten. Each group is assigned to a specific numerical range, preventing conflicts between different output vectors. In contrast, for the full model case (group ID equal to 0), the same identifier is reused at each iteration and the output vectors are overwritten.
- if the output vector ranges are modified (as occurred, for example, in version 2019.1 [55]), the proposed implementation allows updating the entire mapping by changing a single line of code.

It should be noted that group IDs greater than 399 are not supported within the current standardization, as they would break the predefined prefix mapping and potentially cause inconsistencies or ID overlap. Similarly, the ply index (PP) is limited to two digits, and therefore layups with more than 99 plies are not supported.

To preserve the integrity of the identification scheme, inputs outside these defined ranges are explicitly rejected at runtime, as allowing them would lead to silent overwriting or misinterpretation of results. For this reason, such conditions are not handled through implicit truncation or fallback strategies.

These limits are considered acceptable for practical applications, as they still allow the analysis of highly complex models in terms of both number of plies and group ID range.

Mode	**M**	**R**	**PP**	**Description**
FI Hoffman	1	1	ply ID	FI evaluated at ply level
		2	00	Maximum FI value among all plies
MOS Hoffman	2	1	ply ID	MOS evaluated at ply level
		2	00	Minimum MOS value among all plies
FI LaRC05 - ply level	3	1	ply ID	FI for fibre tensile failure
		2	ply ID	FI for matrix failure
		3	ply ID	Fracture angle α corresponding to the maximum FI for matrix failure
		4	ply ID	FI for fibre kinking failure
		5	ply ID	Kink-band angle ψ corresponding to the maximum FI for fibre kinking failure
		6	ply ID	Misalignment angle ϕ associated with the value of ψ maximizing the FI for fibre kinking
		7	ply ID	Maximum FI among all considered failure modes at ply level
		8	ply ID	Failure mode corresponding to the maximum FI
FI LaRC05 - among all the plies	4	1	00	Maximum FI for fibre tensile failure among all plies
		2	00	Maximum FI for matrix failure among all plies
		3	00	Maximum FI for fibre kinking failure among all plies
		4	00	Maximum FI among all plies considering all failure modes
		5	00	Failure mode corresponding to the overall maximum FI
MOS LaRC05 - ply level	5	1	ply ID	MOS for fibre tensile failure
		2	ply ID	MOS for matrix failure
		3	ply ID	Fracture angle α corresponding to the minimum MOS for matrix failure
		4	ply ID	MOS for fibre kinking failure
		5	ply ID	Kink-band angle ψ corresponding to the minimum MOS for fibre kinking failure
		6	ply ID	Misalignment angle ϕ associated with the value of ψ minimizing the MOS for fibre kinking
		7	ply ID	Minimum MOS among all considered failure modes at ply level
		8	ply ID	Failure mode corresponding to the minimum MOS
MOS LaRC05 - among all the plies	6	1	00	Minimum MOS for fibre tensile failure among all plies
		2	00	Minimum MOS for matrix failure among all plies
		3	00	Minimum MOS for fibre kinking failure among all plies
		4	00	Minimum MOS among all plies considering all failure modes
		5	00	Failure mode corresponding to the overall minimum MOS
MOS Sandwich panels	7	1	00 / ply ID	Metallic skins - Dimpling MOS
		2	00 / ply ID	Metallic skins - Wrinkling MOS
		3	00 / ply ID	Metallic skins - Crimping MOS
		4	00 / ply ID	Metallic skins - MOS for yielding
		5	00 / ply ID	Metallic skins - MOS for ultimate tensile failure
		6	00 / ply ID	Metallic skins - MOS for ultimate compression failure
		7	00 / ply ID	Honeycomb - MOS for ultimate shear L direction
		8	00 / ply ID	Honeycomb - MOS for ultimate shear W direction
		9	00 / ply ID	Honeycomb - MOS for combined shear failure

Table A.3: Definition of result identifier (R) and ply index (PP) for each analysis mode (M)